

Ballistic Conduction in Multiwalled Carbon Nanotubes  
at Room Temperature

A Thesis  
Presented to  
The Academic Faculty

by

Yan Yi

In Partial Fulfillment  
of the Requirements for the Degree of  
Doctor of Philosophy in Physics

Georgia Institute of Technology  
May 2004

Ballistic Conduction in Multiwalled Carbon Nanotubes  
at Room Temperature

Approved by:

Dr. Walt A. de Heer, Advisor

Dr. Phillip N. First

Dr. Edward H. Conrad

Dr. Robert L. Whetten

Dr. Thomas K. Gaylord  
(School of Electrical and Computer  
Engineering, G.I.T.)

May 5, 2004

## ACKNOWLEDGEMENTS

There are lots of people I would like to thank for a huge variety of reasons.

Firstly, I would like to thank my Supervisor, Dr. Walt A. de Heer. I could not have imagined having a better advisor and mentor for my PhD, and without his common-sense, knowledge, perceptiveness and cracking-of-the-whip I would never have finished. I can't overstate the importance of his involvement in my graduate career. I am also particularly indebted to Dr. Claire Berger, currently visiting scientist at Georgia Institute of Technology (GIT), for the time spent in discussion of the many topics and ideas that needed to come together in order to make this a successful research, as well as for her tireless help in the preparation of this manuscript. I thank both of them for their incurable enthusiasm for the work and experience with the process allowed them to both encourage me and commiserate with me appropriately. Their timely comments were invaluable throughout.

I would like to thank Dr. Philippe Poncharal, former-postdoc at GIT and currently working as a professor at Université Montpellier II, France, for the earlier contribution on this research.

Thank-you to my committee members, Dr. Phillip N. First, Dr. Edward H. Conrad, Dr. Robert L. Whetten and Dr. Thomas K. Gaylord, for managing to read the whole thing so thoroughly, and for giving me valuable advice.

I would also like to thank all the rest of the academic and support staff of the Department of Physics at GIT for their help through all these years. Thanks Joe Gezo, former undergraduate at GIT and currently being a graduate student at UIUC, for operating TEM. Much respect to my lab-mates, Zhimin Song, Ramiro Moro, Xiaoshan Xu and Shuangye Yin for putting up with me for five years.

Finally, I have to say 'thank-you' to: all my friends and family, wherever they are, particularly my mom and brothers; and, most importantly of all, to my husband Xiaoran Gao, for everything.

Peace and Solidarity,

Yan Yi

## TABLE OF CONTENTS

Acknowledgements	iii
List of Figures	vii
List of Symbols	xv
Summary	xvii
Chapter 1 Introduction	1
1.1 Motivation	1
1.2 Atomic Structure of Carbon Nanotubes	3
1.3 Bonding between carbon atoms in carbon nanotubes	9
1.4 Nanotube Growth Methods	10
1.4.1 Arc-Discharge and Laser-Ablation	10
1.4.2 Chemical Vapor Deposition	13
1.5 Structural Quality of MWNTs Grown by Different Methods	14
Chapter 2 Electronic Structure and Transport Properties of Carbon Nanotubes	17
2.1 Electronic Structures	17
2.1.1 Structure of graphene	18
2.1.2 Electronic structure of $\pi$ bands for graphene	19
2.1.3 Electronic Structure of Single-wall Carbon Nanotubes	20
2.1.4 Multi-walled nanotubes: structure and properties	32
2.2 Basics of Transport of One-Dimensional Conductor	33
2.2.1 Resistance of a ballistic conductor	33
2.2.2 Landauer formula	35
2.3 Transport properties of carbon nanotubes	37
Chapter 3 Experiment Configurations and Procedures	41
3.1 Sample preparation	41
3.2 Experiment using SPM	44
3.3 Experiment using TEM	48

Chapter 4 Observations and Results	54
4.1 Low-Bias Experiments	54
4.1.1 Clean nanotubes	54
4.1.2 Nanotubes covered with surfactant	59
4.2 High-Bias Experiments	62
4.2.1 Clean nanotubes	62
4.2.2 Nanotubes covered with surfactant	64
4.3 Measurements of variable contacts	64
4.4 Observations of non-conducting MWNT	70
4.5 Observations of Nanotube failure	72
4.6 Observations of Hg bubble formation	74
4.7 Experiments with a small Hg droplet touching an HOPG surface	79
Chapter 5 Analysis and Interpretation	81
5.1 Analysis of low-bias conductance curves	81
5.2 Ballistic transport in carbon nanotubes	88
5.3 Scattering at Contacts	90
5.4 Scattering from defects and contaminants	93
5.5 Conductance versus voltage	95
5.6 In-situ measurements of variable contacts	99
5.7 Non-conducting MWNT	100
5.8 In-situ observations of nanotube failure	101
5.9 Hg bubble formation	102
5.10 Experiments with a small Hg droplet touching an HOPG surface	103
5.11 Comparisons with theory and with other experiments	103

Chapter 6 Summary and Conclusion	111
Appendix A: Derivation of Tight-Binding Calculation for $\pi$ Electrons of graphene	118
References	121

## LIST OF FIGURES

Figure 1.1	The structure of a honeycomb lattice, which contains two atoms per unit cell.	4
Figure 1.2	The crystal structure of hexagonal single crystal graphite, in which the distinct planes of carbon hexagons are stacked in the <b>ABAB</b> sequence (Wyckoff, 1964).	4
Figure 1.3	The unrolled honeycomb lattice of a nanotube, showing the unit vectors $\vec{a}_1$ and $\vec{a}_2$ for the graphene sheet. When we connect sites O and A, and B and B', a nanotube can be constructed. $OA$ and $OB$ define the chiral vector $C_h = n\hat{a}_1 + m\hat{a}_2$ and the translational vector $T$ of the nanotube, respectively. The rectangle $OAB'B$ defines the unit cell for the nanotube. The figure corresponds to $C_h = (4,2)$ (Saito, 1998).	5
Figure 1.4	Schematic models for SWNTs with the nanotube axis normal to the chiral vector which, in turn, is along: (a) the $\theta=30^\circ$ direction, [an armchair (n,n) nanotubes], (b) the $\theta=0^\circ$ direction, [a zigzag (n,0) nanotube], and (c) a general $\theta$ direction, such as $OB$ (see Figure 1.2), with $0 < \theta < 30^\circ$ [ a chiral (n,m) nanotubes]. The actual nanotubes shown here correspond to (n,m) values of: (a) (5,5), (b) (9,0), and (c) (10,5) (Dresselhaus, 1995).	6
Figure 1.5	HRTEM image of a SWNT. (Zettl, unpublished) The diameter of SWNTs is typically in the rang of 1-2 nm.	8
Figure 1.6	The observation by TEM of multi-walled coaxial nanotubes with various inner and outer diameters, $d_i$ and $d_o$ , and numbers of cylindrical shells $N$ reported by Iijima in 1991: (a) $N=5$ , $D_o=67 \text{ \AA}$ ; (b) $N=2$ , $D_o=55 \text{ \AA}$ ; and (c) $N=7$ , $D_i=23 \text{ \AA}$ , $D_o=65 \text{ \AA}$ (Iijima, 1991).	8
Figure 1.7	Schematic experimental setups for nanotube growth methods.	12
Figure 1.8	Scanning Electron Microscope image of the (a) rod-shaped deposit on the cathode and of (b) a zoomed part of a deposit, which shows the heterogeneous character of the arc-grown nanotube soot (Bonard, 1997).	13
Figure 1.9	HRTEM image of an arc-produced MWNT. Each concentric layer can easily be seen (de Heer, unpublished).	15
Figure 1.10	HRTEM images of CVD grown MWNTs, which produced by the decomposition of acetylene using a Co/silica catalyst, (i) at $720^\circ\text{C}$	16

	and (ii) at 900°C. All scale bars are 10 nm (Forró, 1999).	
Figure 1.11	HRTEM images of arc-produced MWNTs after purified for 45 minutes in ambient air at 750°C and then dispersed in isopropanol and mixed ultrasonically. (Roschier, 1999). Note the surface roughness of these treated MWNTs.	16
Figure 2.1	(a) The unit cell and (b) Brillouin zone of graphene are shown as the dotted rhombus and shaded hexagon, respectively. $\vec{a}_i$ and $\vec{b}_i$ ( $i = 1; 2$ ) are unit vectors and reciprocal lattice vectors, respectively. $\Gamma$ , K and M are defined as the center, the corner and the center of the edge of the Brillouin zone, respectively (picture from Saito, 1998).	18
Figure 2.2	The electronic structure of graphene using tight binding calculations for $\pi$ electrons (Schönenberger, 2000). Here $\gamma_1$ is the nearest-neighbor overlap integral. The inset shows the electronic structure in the vicinity of the Fermi level of graphene.	20
Figure 2.3	The reciprocal lattice vectors, $K_1$ and $K_2$ , for a $C_h = (4,2)$ chiral nanotube. The vectors $K_1$ and $K_2$ are reciprocal lattice vectors corresponding to $C_h$ and $T$ , respectively. The line segment $WW'$ , which is parallel to $K_2$ , represents the Brillouin zone of the nanotube. The figure corresponds to $C_h = (4, 2)$ , $T = (4, -5)$ , $K_1 = (5b_1 + 4b_2)/28$ , $K_2 = (4b_1 - 2b_2)/28$ [Saito, 1998].	21
Figure 2.4	The condition for metallic energy bands: if the ratio of the length of the vector $\vec{YK}$ to that of $K_1$ is an integer, metallic energy bands are obtained (Saito, 1998).	22
Figure 2.5	The carbon nanotubes $(n, m)$ that are metallic and semiconducting, respectively, are denoted by open and solid circles on the map of chiral vectors $(n, m)$ . For very small diameter nanotubes (e.g., $d_t < 0.7$ nm), the tight binding approximation is not sufficiently accurate, and more detailed approaches are needed. For example, small diameter nanotubes, such as the $(4,2)$ nanotube is predicted to be semiconducting by tight binding approximation, though more detailed calculations show $(4,2)$ to be metallic (Saito, 1998).	23
Figure 2.6	One-dimensional electronic structures for (a) armchair $(5, 5)$ , (b) zigzag $(9, 0)$ , and (c) zigzag $(10, 0)$ carbon nanotubes. The X points for armchair and zigzag nanotubes correspond to $k = \pm\pi/a$ and $k = \pm\pi/\sqrt{3}a$ , respectively. Here $\gamma_1$ is the nearest-neighbor overlap integral (Saito, 1992).	24
Figure 2.7	Electronic structure of nanotube $(12, 6)$ . The X point has a wave number near $\pi/a$ . The arrow shows a wave vector corresponding to	25

- the  $K$  point (Hamada, 1992).
- Figure 2.8 Electronic 1D density of states per unit cell of a 2D graphene sheet for two  $(n, 0)$  zigzag nanotubes: (a) the  $(10, 0)$  nanotube which has semiconducting behavior, (b) the  $(9, 0)$  nanotube which has metallic behavior. Also shown as a dashed line in the figure is the density of states for the 2D graphene sheet (Saito, 1993). 26
- Figure 2.9 The 1D electronic bands of a  $(n,m)=(100,100)$  carbon nanotube calculated in the tight binding model with  $|\gamma_1|=2.9$  eV and  $a_0=0.142$  nm, where the energy of the subbands are plotted versus  $K_z$  (the wave number along the tube) by de Heer (Berger, 2002). This  $D = 13.6$  nm diameter nanotube is in the range of diameters typical of the nanotubes studied here (i.e.  $5\text{nm}<D<20\text{nm}$ ). The electronic transport in this metallic nanotube is due to the two subbands that cross the Fermi level (see inset). Above and below the Fermi level are two sets of semiconducting subbands. The gap between these is  $E_{gap} = 6 |\gamma_1| a_0 / D = 180$  mV ( $\sim 7$  kT at room temperature, note that for semiconducting tubes with the same diameter, the gap is a factor of 3 smaller). The transport properties of the conducting subbands are unique and characterized by very low back scattering compared with the semiconducting bands (White, 1998; Charlier, 1998). 29
- Figure 2.10 The density of states versus energy of the nanotube calculated by de Heer (Berger, 2002) shown in Figure 2.9 . The typical van Hove singularities, which occur when the energy coincides with the bottom of the subbands, produce a set of approximately equally spaced spikes. Superimposed is also the DOS after gaussing smoothing with  $\Delta E = 25$  mV to simulate effect of room temperature. This results in a nearly linear dependence of the DOS with energy. For  $|E| < E_{gap}/2 = 90$  mV the DOS is essentially constant (White, 1998; Charlier, 1998). 30
- Figure 2.11 A narrow two-dimensional conductor with width  $W$  and length  $L$  ( $W \ll L$ ) sandwiched between two contacts across which an external bias is applied. 34
- Figure 2.12 The predicted conductance  $G$  versus bias voltage for this nanotube from the Landauer equation, assuming unit transmission for all channels, which states that when the bias voltage increases above the bottom of a subband, then that subband contributes  $G_0$  to the conduction, which gives  $G(V)$  its staircase appearance (calculated by de Heer (Berger, 2002)). Due to the symmetry above and below  $E_F$ , contributions from subbands below  $E_F$  and above  $E_F$  coincide so that the conductance increases in steps of  $2 G_0$ . Thermal smearing at  $T = 300$  K blunt the steps to provide an essentially perfectly linear rise in the conductivity with increasing bias voltage. The linear

	increase in the DOS is common to all metallic nanotubes independent of helicity up to about $V_{bias} = 6V$ (White, 1998; Charlier, 1998).	38
Figure 3.1	TEM image of clean carbon nanotubes protruding from a fiber (on the lower-left corner). The fiber has the length of 1 mm and a diameter of 50 $\mu\text{m}$ . The longest tube shown on this picture is 3.7 $\mu\text{m}$ length and about 25 nm diameter (de Heer, unpublished).	42
Figure 3.2	TEM image of the tip of the longest tube shown in Figure 3.1. The straightness of the tube indicates its high purity (defects are known to bend the tubes) (de Heer, unpublished).	42
Figure 3.3	TEM image shows that the carbon nanotubes protruding from the fiber (on the bottom) are covered with carbon balls (de Heer, unpublished).	43
Figure 3.4	Schematic diagram of the experimental setup. The nanotube contact is lowered under SPM control to a liquid metal surface. After contact is established, the current $I$ is measured as the fiber is moved into the liquid metal. Since the length of the nanotube left outside of the mercury decreases when the fiber is moved into the liquid metal, the conductance can be determined as a function of the length of the nanotube.	44
Figure 3.5	Block diagram of SPM experimental setup. The z-piezo under the liquid metal container can move the container up and down. When the z-piezo moves the container up, the sample fiber is relatively moved lower toward the metal liquid surface. $V_{applied}$ is the applied voltage on the tube and the resistor in series with the tube. $V_{measured}$ is the measured voltage drop on the tube and is used to calculate the current passing through the nanotube.	46
Figure 3.6	Sketch of TEM sample holder specially designed for nanotube experiments (length is 35 mm, width 7 mm). The fiber sample mounted on a conducting wire (on the left) can be manually moved toward the mercury droplet (on the right) using a manipulator. The piezo actuator is used for the final approach. A voltage is applied to the conducting wire connecting with the fiber, and the copper wire wetted with a mercury droplet is grounded. Teflon is used as electrical isolation.	49
Figure 3.7	Block diagram of TEM experimental setup. Two voltage dividers are used to convert the I/O piezo voltages (up to 150 V) to a value in the limit of the DAQ interface (<10 V).	51
Figure 3.8	Schematic sketch showing the relative position of a nanotube and	

the mercury droplet (a) in which the contact point is under the mercury droplet and can't be seen using microscope. (b) in which the contact point can be observed using microscope.

53

Figure 4.1 TEM image of a MWNT fiber tip opposing a mercury surface and the dipping process. (a) The nanotubes protrude from the fiber that is composed of densely packed carbon nanotubes and other graphitic nanostructures. The transport measurements are made by lowering the tip into the liquid metal and measuring the conductance as a function of the position. Inset: Example of cone shaped meniscus attached to the tip of the nanotube which occurs when the nanotube is pulled out of the (non-wetting) liquid just before contact is broken. (b) A full cycle conductance trace (conductance  $G=I/V$  versus position) where the fiber is first lowered to the Hg and subsequently withdrawn (see upper axis). Note the asymmetry with respect to the turning point due to the non-wetting adhesive effects.

55

Figure 4.2 Cleaning of nanotubes and evolution of nanotube fiber properties by repeated dipping in Hg. (a) Conduction trace of the virgin fiber: steps are barely discernable; (b) Steps develop after a few hundred cycles but they still exhibit relatively large slopes and jumps. (c) After several thousand cycles, the conductance steps are well developed and the pattern of conductance curve is stable. The first step evolves from the shoulder seen in (a) (step:  $0.2 G_0$ , slope:  $36 \text{ k}\Omega/\mu\text{m}$ ) to a rounded step in (b) (step:  $0.62 G_0$ , slope:  $4 \text{ k}\Omega/\mu\text{m}$ ), to the well-defined step with a flat plateau in (c). The second conductance step is due to another tube and evolves analogously. (d) TEM micrograph of a virgin fiber tip opposing Hg surface. Note the contaminating graphitic particles and the loose structure of the tip. (e) TEM micrograph of a fiber tip that has previously been repeatedly dipped in Hg, and the nanotubes are straight and free of particles and the fiber is compacted.

58

Figure. 4.3 Effect of a surfactant on  $G(x)$ . (a) For a sodium dodecyl sulfate coated nanotube, its conductance  $G(x)$  continues to increase with increasing  $x$ , in contrast to clean tubes. (b) The resistance  $R(x)=1/G(x)$ . The solid line is the fitting line to the semi-classical model (see chapter 5 (Eq. 5.3)). Note that  $R(x)$  asymptotically approaches the slope  $-dR/dx = 2.3 \text{ k}\Omega/\mu\text{m}$  (dot-dashed line), from which about  $0.1 \text{ k}\Omega/\mu\text{m}$  is due to the metal contact resistance of  $500 \Omega\mu\text{m}$ . The  $-dR/dx$  slope is more than an order of magnitude greater than the slope typically found for clean tubes of similar length i.e.  $-dR/dx = 0.2 \text{ k}\Omega/\mu\text{m}$  (dashed line). Inset: resistance  $R$  as a function of  $1/x$ , showing that contrary to a clean tube the shape of the conductance trace is not only determined by the contact

conductance. (c-d) Example of a clean nanotube of similar length (2  $\mu\text{m}$ ) used for comparison (see chapter 5) (c)  $G(x)$  with a low plateau conductance  $G_{pl}=0.64 G_0$  (d)  $R(x)$  asymptotically approaches the plateau resistance  $R_{pl} = 20.3 \text{ k}\Omega$  ; from the slope at  $x= 2\mu\text{m}$ ,  $-dR/dx = 260 \text{ }\Omega/\mu\text{m}$  (dot-dashed line) which is an upper limit to the resistance of the tube. Also shown is the slope  $-dR/dx= 2.3 \text{ k}\Omega/\mu\text{m}$  (dashed line) corresponding to the surfactant coated tube in (b).

61

Figure 4.4 Conductance versus voltage  $G(V)$ . (a) For a clean nanotube in air from  $V= - 4.0$  to  $+4.0 \text{ V}$  and from  $V= -1.3$  to  $+1.3 \text{ V}$  in the TEM (inset). Note the symmetry of  $G(V)$ . There is no saturation (a decrease in conductivity) with increasing voltage in this case. The current at  $V=4 \text{ V}$  corresponds to  $I=615 \text{ }\mu\text{A}$ . (b)  $G(V)$  of a nanotube for various positions  $x$  into the Hg as indicated on the  $G(x)$  trace in the inset. Inset: open circles show the different positions in situ measurements of  $G(V)$  of a nanotube contacted in the TEM.

63

Figure 4.5 Effect of surfactant on  $G(V)$ . An example of  $G(V)$  for a surfactant coated nanotube. Note the differences with clean tubes, in particular the non-linearity and the asymmetry with respect to  $V=0$ . The conductance saturates for  $V= -1.5 \text{ V}$ . This behavior is reproducible for this nanotube, however the shift and the asymmetry is sample dependent.

64

Figure 4.6 Conductance  $G(V)$  vs.  $V$  for a MWNT contacted to Hg in the TEM for successive voltage sweeps from  $0 \text{ V} \rightarrow V_{\text{max}} \rightarrow 0 \text{ V} \rightarrow -V_{\text{max}} \rightarrow 0 \text{ V}$ . The low bias conductance is initially low (at **a**). When the bias voltage reaches  $1.5 \text{ V}$  the conductance jumps abruptly (**b**). A stable linear pattern develops for many sweeps (**c**). The bias voltage sweep range is then increased, which induces a change (**d**) in the conductance. The new pattern (**e**) is stable. After again increasing the bias voltage sweep range,  $G(0)$  increases again and the stable characteristics (**f**) is obtained. Now the conductance attains a maximum. The bias voltage sweep range was next increased to  $3 \text{ V}$ , and the nanotube failed at  $V=2.9 \text{ V}$ .

67

Figure 4.7 Conductance  $G(V)$  vs.  $V$  for a nanotube (10 nm diameter,  $2.5 \text{ }\mu\text{m}$  long) contacted to Hg in the TEM. (**a**) Initially, the contact to the Hg is small and the nanotube appears to bend over the Hg surface. (**b**) After the fiber is pushed closer to the Hg surface, the contact geometry is more consistent with the nanotube submerging on the order of  $1 \text{ }\mu\text{m}$  below the Hg surface. (**c**) The tube is retracted to produce a small contact, and retracted slightly further in (**d**). In (**e**) the contact area was so small that the nanotube drifted out of contact, causing  $G(V)=0$ . Contact spontaneously reestablished at

$G(V=2.8V)$ , which coincides with the previous voltage sweep **(d)**. The nanotube then failed ( $V_{bias}=3$  V,  $G(3V)=1.2$  G<sub>0</sub>) at the contact with the Hg. **(f-h)** Summary of the  $G(V)$  characteristics observed at small contact for the same tube. Note in particular the variation in  $G(0)$ , the range of  $dG(V)/dV$ , the  $G(V)$  shape variation, the fact that some curves intercept others. Since only the contact with the Hg surface varied, the observed variations should be ascribed to the contact properties.

68

Figure 4.8 Conductance of a highly resistive MWNT submerged over 1 μm in Hg.

71

Figure 4.9 Before and after in situ TEM images of nanotubes contacted with Hg and their failure at high currents. (a-b) Typical failure of a clean nanotube. The failure occurred at the contact with the Hg after applying 4 V leaving a short (~20 nm long) stem at the original contact point. Before the failure the measured resistance was  $12.7 \pm 0.2$  kΩ. (c-d) One kinked and two contaminated nanotubes, showing that the failure occurred at the defects. (e-f) High resolution images of the failure of a clean gold contacted nanotube showing that only the outer layer is affected, which corresponds to the current flow pattern in these tubes (pictured taken by Ugarte). (g) Failure of many tubes in parallel at the contact with the Hg resulting in the “cut grass” appearance. This corresponds to the typical failure of clean tubes as explained in the text.

73

Figure 4.10 TEM picture of a Hg bubble stabilized at the contact of a nanotube to the Hg with a voltage of ~1.5 V. The shape appears to be a spherical segment with a radius of 0.5 μm. This phenomenon occurs when the nanotube is negatively biased with respect to the Hg, when only the tip of the nanotube touches the surface under high current conditions.

75

Figure 4.11 TEM picture of a Hg bubble stabilized at the contact of a nanotube to the Hg with a voltage of ~1.5 V. Note the spherical shape of the bubble and of a meniscus at the nanotube-Hg contact. This phenomenon occurs when the nanotube is negatively biased with respect to the Hg, when only the tip of the nanotube touches the surface under high current conditions.

77

Figure 4.12 Conductance  $G(V)$  versus V for a tube (10 nm diameter) in contact with Hg. **(a)** Hg bubbles are formed. **(b)** The tube drifted away, causing the conductance to decrease. The bubbling phenomenon stopped. After pulling the tube out, contact was re-established in **(c)**. No bubble was observed even for higher bias voltage and current than in **(a)**, indicating the influence of the nature of the contact. In

78

all cases, note the symmetry of the conductance versus polarity.

- Figure 4.13 Conductance  $G(V)$  versus  $V$  for a HOPG sample contacted to a droplet of liquid Hg in air, for several different contacts (the larger the contact, the greater  $G(V=0)$ ). As for MWNT the conductance increases with increasing voltage. The increase is monotonic, essentially linear and remarkably symmetric (Berger, 2002). 79
- Figure 5.1 A representative conductance trace (one of 50 of this nanotube) as a function of the distance  $x$  between tip of the nanotube and the Hg surface (i.e. the depth of the nanotube merged inside the mercury). (a) The conductance  $G(x)$  in units of the conductance quantum, showing the initial conductance jump at  $x=0$  to  $0.85 G_0$ , followed by a rounded step, of which the slope gradually decreases to 0 with increasing  $x$ . (b) The resistance  $R(x)=1/G(x)$ . Note that the slope gradually decreases to 0. Dashed line corresponds to the slope at  $x=2.5 \mu\text{m}$ , which corresponds to the upper limit of the tube resistance:  $\rho < 48 \Omega/\mu\text{m}$ ; line (1) corresponds to  $\rho = 10 \text{ k}\Omega/\mu\text{m}$  found in Reference (Bachtold, 2000) for MWNTs; line (2)  $\rho = 4 \text{ k}\Omega/\mu\text{m}$  found in Reference (Schonenberger, 1999), and line (3)  $\rho = 1.5 \text{ k}\Omega/\mu\text{m}$  found for a SWNT bundle which was characterized as a ballistic conductor in Reference (Bachtold, 2000) (c) Nanotube resistance plotted as a function of  $1/x$ , revealing a straight line:  $R(1/x)=14.1+0.271/x \text{ k}\Omega$ . This demonstrates that the contact resistance indeed determines the shape of the conductance trace. 82
- Figure 5.2 Diagram of a tube in contact with mercury.  $x$  represents the length of the tube submerged inside the mercury. The contact area of a tube with mercury includes the tip area and the area of the sidewall of the tube. The tip area is constant. The area of sidewall is proportional to  $x$ . Thus the total contact area is proportional to  $x$ . 83
- Figure 5.3 The distribution of measured values of nanotube resistance per unit length  $\rho=31\pm 47 \Omega/\mu\text{m}$ . 87

## LIST OF SYMBOLS

MWNTs	Multi-walled carbon nanotubes.	
SWNTs	Single-walled carbon nanotubes.	
HRTEM	High resolution transmission electron microscopy.	
$G_0$	Conductance quantum $G_0 = 2e^2 / h = (12.9 \text{ K}\Omega)^{-1}$ .	$\text{k}\Omega^{-1}$ or $G_0$
$C_h$	The chiral vector $C_h = n\hat{a}_1 + m\hat{a}_2$ , here $\hat{a}_1$ and $\hat{a}_2$ are the unit vectors of the hexagonal honeycomb lattice of the graphene sheet and the coefficients m and n are integers.	
$D_t$	The diameter of the (n,m) nanotube $D_t = \sqrt{3}a_{c-c}(m^2 + mn + n^2)^{1/2} / \pi$ .	nm
$\theta$	The chiral angle $\theta = \tan^{-1}[\sqrt{3}n / (2m + n)]$ .	
CVD	Chemical Vapor Deposition.	
$a_0$	The nearest neighbor distance of graphene $a_0 = 1.42 \text{ \AA}$ .	$\text{\AA}$
$a$	The lattice constant in the real space of graphene $a = \sqrt{3}a_0$ .	$\text{\AA}$
$\gamma_1$	The nearest-neighbor overlap energy integral $\gamma_1 \approx -3 \text{ eV}$ for $\pi$ bands of carbon atoms in graphene (Painter, 1970).	eV
$K_1$	The wave vector associated with the $C_h$ direction.	$\text{nm}^{-1}$
$K_2$	The wave vector associated with the direction along the nanotube axis.	$\text{nm}^{-1}$
$L_m$	The momentum relaxation length (or mean free path), which is the average length that an electron travels before it is scattered by a scattering center.	$\mu\text{m}$
$\lambda_F$	The Fermi wavelength defined by $\lambda_F = 2\pi/k_F$ , which is the de Broglie wavelength for electrons at the Fermi energy.	nm
$G$	The conductance of a system $G = I/R$ .	$\text{k}\Omega^{-1}$ or $G_0$

$\sigma$	The conductivity of 2D conductor, which is a material parameter independent of the sample dimensions.	$k\Omega^{-1}$ or $G_0$
$G_c$	The contact conductance at a interface.	$k\Omega^{-1}$ or $G_0$
$R_c$	The contact resistance $R_c = G_c^{-1}$ .	$k\Omega$
$T$	The average probability that an electron injected at one end of the conductor will transmit to the other end.	
$N$	The number of available conducting subbands inside the conductor.	
$G_s^{-1}$	The scattering resistance $G_s^{-1} = I / (NG_0) \cdot (1-T)/T$ .	$k\Omega$
SPM	Scanning probe microscope.	
TEM	Transmission electron microscope.	
$x$	The length of the tube submerged inside the mercury.	$\mu\text{m}$
$R_{NT-M}$	The metal-tube contact resistance includes the contact resistance at the tip ( $R_{tip}$ ), and at the sidewall of the tube with mercury ( $R_{sidewall}$ ).	$k\Omega$
$R_{NT-F}$	The fiber-tube contact resistance.	$k\Omega$
$\rho$	The nanotube intrinsic resistance per unit length.	$k\Omega/\mu\text{m}$
$R_{NT-M}^*$	$R_{NT-M}^*$ is related to the transmission probability decided by scattering at the sidewall tube-mercury contact.	$k\Omega \cdot \mu\text{m}$

## SUMMARY

Multiwalled carbon nanotubes (MWNTs) are shown to be ballistic conductors at room temperature, with mean free paths of the order of tens of microns. The electrical transport measurements are performed both in air and in high vacuum in the transmission electron microscope on nanotubes pointing out of a nanotube-containing fiber that contact with a liquid metal. These measurements demonstrate that metallic MWNTs are one dimensional conductor that have quantized conductance nearly  $1G_0$  ( $\approx(12.9 \text{ K}\Omega)^{-1}$ ). The intrinsic resistance per unit length is found to be smaller than  $100 \text{ }\Omega/\mu\text{m}$ , indicating a mean free path  $l > 65 \text{ }\mu\text{m}$ . The nanotube-metal contact resistances are in the range from 0.1 to  $1 \text{ k}\Omega\mu\text{m}$ . Contact scattering can explain why the measured conductances are about half of the expected theoretical value of  $2G_0$ . Current-to-voltage characteristic are in accord with the electronic structure. The nanotubes can survive high current (up to 1 mA, i.e., current density on the order of  $10^9 \text{ A/cm}^2$ ). In situ electron microscopy shows that a relative large fraction of the nanotubes do not conduct (even at high bias), consistent with the existence of semiconducting nanotubes. Discrepancies with other measurements are most likely due to damage caused to the outer layer(s) of the nanotubes during processing. The measured mean free path of clean, undamaged arc-produced MWNTs is several orders of magnitude greater than that for metals, making this perhaps the most significant property of carbon nanotubes.

## CHAPTER 1

### INTRODUCTION

#### 1.1 Motivation

The discovery of carbon nanotubes was as early as 1976 when Endo synthesized vapor grown carbon fibers (Endo, 1978). They are hollow, long and thin cylinders made of carbon closed by caps at the ends. Hyperion Catalysis International, Inc. developed the vapor growth method in the 1980's. However, there were no detailed systematic studies of nanotubes reported until 1991, when the field was seriously launched by Iijima. He observed multi-walled carbon nanotubes (MWNTs) in arc-produced carbon soot using High Resolution Transmission Electron Microscopy (HRTEM) (Iijima, 1991). Later he observed single-walled carbon nanotubes (SWNTs) in 1993 (Iijima, 1993).

A SWNT can be considered as a single sheet of graphite that has been rolled into a cylinder. MWNTs consist of a nested coaxial array of SWNT constituents. Their structures are unique. With only a few nanometers in diameter, but up to an order of 100  $\mu\text{m}$  long, their length-to-width aspect ratio is extremely high.

Nanotubes have a broad range of structural and electronic properties that change depending on the different kinds of nanotube (defined by its diameter, length, chirality, doping and defects). Depending on chirality (the direction in which the sheet was rolled up) and diameter, they can behave like metals with high electrical conductivity, or semiconductors with relatively large band gaps. Besides having a single cylindrical wall (SWNTs), nanotubes can have multiple walls (MWNTs)--cylinders inside the other cylinders. These complications make it difficult to discover their properties.

There have been many experimental studies on carbon nanotubes to understand their electronic properties. Those experiments involved both two- and four-probe measurements on a number of different MWNTs and SWNTs. They showed a variety of resistivity behaviors for the different tubes. Earlier experiments with micro-fabricated contacts found very strong evidence that electrons were diffusively scattered in MWNTs (Langer, 1996; Schonberger, 1999; Dai, 1996; Bachtold, 2000; Collins, 2002). However, in 1998, Walt de Heer and colleagues at the Georgia Institute of Technology designed and realized an ingenious way to measure the electrical conductance of MWNTs (Frank, 1998). A macroscopic fiber of MWNTs was gently lowered into liquid metal. Because individual nanotubes stick out from the fiber, it makes it possible to determine the resistance of individual nanotubes by dipping the nanotubes to different depths. This technique also allows any variation of resistance with length to be detected. This method for making electrical contact with nanotubes is very different from techniques that rely on sub-micron fabrication technology. De Heer and colleagues found that all conducting MWNTs had nearly the same conductance,  $G_0 = 2e^2/h = (12.9 \text{ K}\Omega)^{-1}$ , and that the dependence of the resistance on length was very weak. MWNTs were ballistic conductors. At the time this thesis research began, there was no indication for any of those properties either from theory or from other experiments. The question of whether the electron transport in MWNTs is ballistic or diffusive remained debated in the literature and needed to be solved.

This thesis focuses on the electronic transport properties of arc-produced carbon MWNTs and investigates their electrical conductivity. It follows and extends the original experimental setup by de Heer and colleagues, and confirms conductance quantization of

the nanotubes as a one-dimensional conductor. It provides details on the nanotube-metal contacts and a detailed analysis of the length dependence of the resistance, explains and demonstrates why our results are different from other groups' conclusions, and eventually proves that MWNTs are ballistic conductors at room temperature, over a length of microns.

This thesis is organized as follows. The first chapter is the introduction. I will first introduce the atomic structure of carbon nanotubes, and explain the bondings between carbon atoms in carbon nanotubes. Then I will briefly review the different growth methods of nanotubes and also compare the structural qualities of different nanotubes. The second chapter is devoted to the electronic structure and transport properties of carbon nanotubes, which give a foundation to understand the experimental results presented later. The details of our experimental configurations and procedures are explained in the third chapter. Our experimental observations and results are presented in the fourth chapter. Finally the interpretations and conclusions of our experiments are in chapters five and six.

## 1.2 Atomic structure of carbon nanotubes

Recall that a SWNT can be thought of as a single graphite sheet rolled into a cylinder. It is helpful to review the atomic structure of graphite before introducing the atomic structures of carbon nanotubes.

The ideal crystal structure of graphite consists of a stack of identical atomic layers (graphene sheets) (shown in Figure 1.1), in which the carbon atoms are arranged in an open honeycomb network containing two atoms per unit cell. These two atoms are labeled A and B on one layer, and A' and B' on its consecutive layers. The stacking of

the graphene layers is arranged, such that the  $A$  and  $A'$  atoms are on top of one another, but the  $B$  atoms in one plane are over the unoccupied centers of the adjacent layers, and similarly for  $B'$  atoms on the other plane (Wyckoff, 1964). This gives two distinct planes, which are labeled by  $A$  and  $B$ . These distinct planes are stacked in the ' $ABAB$ ' stacking arrangement shown in Figure 1.2, with a very small in-plane nearest-neighbor distance  $a_0$  of  $1.421 \text{ \AA}$ , an in-plane lattice constant  $a$  of  $2.462 \text{ \AA}$ , and an interplane distance of  $3.354 \text{ \AA}$ .

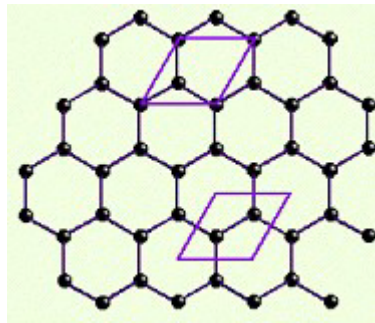


Figure 1.1: The structure of a honeycomb lattice, which contains two atoms per unit cell.

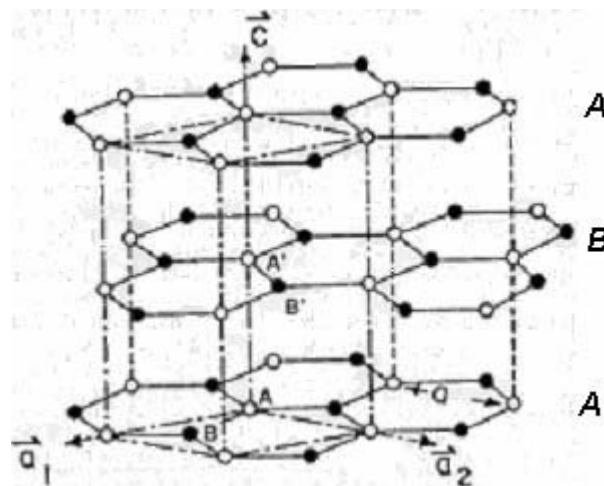


Figure 1.2: The crystal structure of hexagonal single crystal graphite, in which the distinct planes of carbon hexagons are stacked in the  $ABAB$  sequence (Wyckoff, 1964).

As mentioned earlier in this chapter, the structure of SWNTs can be generated by rolling up a graphene sheet into a cylinder. This can be explained using the vectors  $C_h$  and  $T$  in Figure 1.3 (Saito, 1998).  $C_h$  is the chiral vector expressed as  $C_h = n\hat{a}_1 + m\hat{a}_2$ , here  $\hat{a}_1$  and  $\hat{a}_2$  are the unit vectors of the hexagonal honeycomb lattice of the graphene sheet (see Figure 1.3), and the coefficients  $m$  and  $n$  are integers. The chiral vector expresses the circumference of any carbon nanotube and describes the way the graphene sheet is rolled-up, and relates to the chirality of the nanotube. The cylinder is formed by superimposing the two ends of the vector  $C_h$  and the cylinder joint is made along the two lines  $OB$  and  $AB'$  in Figure 1.3. The lines  $OB$  and  $AB'$  are both perpendicular to the vector  $C_h$  at each end of  $C_h$ .

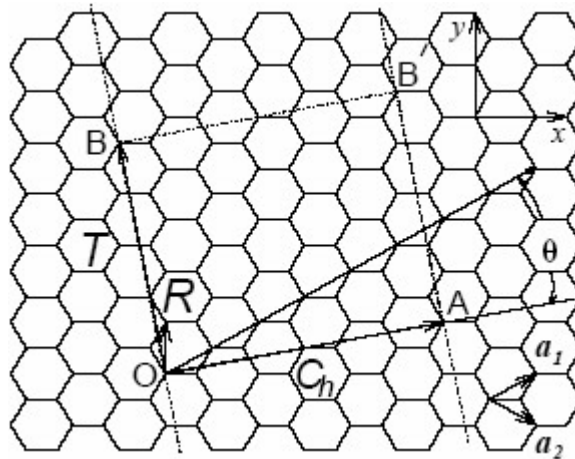


Figure 1.3: The unrolled honeycomb lattice of a nanotube, showing the unit vectors  $\vec{a}_1$  and  $\vec{a}_2$  for the graphene sheet. When connecting sites  $O$  and  $A$ , and  $B$  and  $B'$ , a nanotube can be constructed.  $OA$  and  $OB$  define the chiral vector  $C_h = n\hat{a}_1 + m\hat{a}_2$  and the translational vector  $T$  of the nanotube, respectively. The rectangle  $OAB'B$  defines the unit cell for the nanotube. The figure corresponds to  $C_h = (4,2)$  (Saito, 1998).

The pair of integers  $(n,m)$ , which specify the chiral vector, uniquely defines the nanotube structure. Three distinct types of nanotube structures can be generated. The

vectors  $(n,0)$  or  $(0, m)$  denote zigzag nanotubes and the vectors  $(n,n)$  denote armchair nanotubes. Both armchair and zigzag nanotubes have a mirror plane and thus are considered as achiral. All other vectors  $(n,m)$  correspond to chiral nanotubes (Saito, 1992). Schematic models are shown in Figure 1.4.

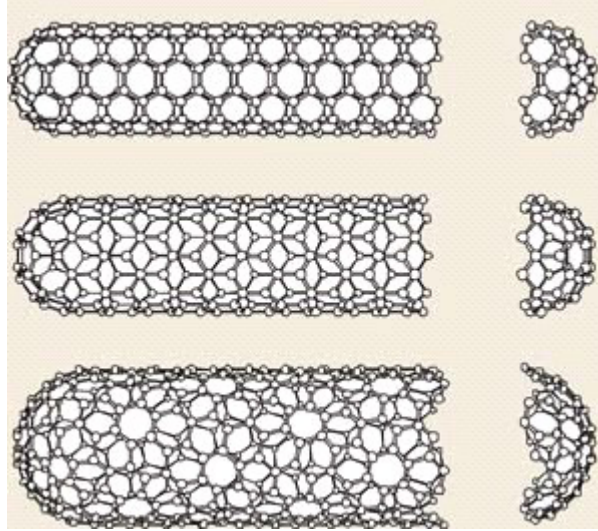


Figure 1.4: Schematic models for SWNTs with the nanotube axis normal to the chiral vector which, in turn, is along: (a) the  $\theta=30^\circ$  direction, [an armchair  $(n,n)$  nanotubes], (b) the  $\theta=0^\circ$  direction, [a zigzag  $(n,0)$  nanotube], and (c) a general  $\theta$  direction, such as OB (see Figure 1.2), with  $0 < \theta < 30^\circ$  [ a chiral  $(n,m)$  nanotubes]. The actual nanotubes shown here correspond to  $(n,m)$  values of: (a)  $(5,5)$ , (b)  $(9,0)$ , and (c)  $(10,5)$ . (Dresselhaus, 1995)

The diameter  $D_t$  of the  $(n,m)$  nanotube is given by

$$D_t = \sqrt{3}a_{c-c}(m^2 + mn + n^2)^{1/2} / \pi \quad (1.1)$$

where  $a_{c-c}$  is the C-C bond length (1.42 Å). The chiral angle  $\theta$  shown in Figure 1.3,

between the chiral vector  $C_h$  and the “zigzag” direction ( $\theta=0$ ), is given by

$$\theta = \tan^{-1}[\sqrt{3}n / (2m + n)] \quad (1.2)$$

If  $\theta$  is limited to be between  $0 \leq \theta \leq 30^\circ$ , the zigzag and armchair nanotubes, respectively, correspond to chiral angles of  $\theta=0$  and  $30^\circ$ , and chiral nanotubes correspond to  $0 < \theta < 30^\circ$ . Differences in the nanotube diameter and chiral angle give rise to difference in the properties of the various carbon nanotubes. The vector  $OB$ , which is normal to  $C_h$ , determines the fundamental one-dimensional translation vector  $T$ .

Recall that a MWNT consists of a nested coaxial array of SWNT constituents, separated from one another by approximately  $3.4 \text{ \AA}$ , which is close to the interlayer spacing of graphite. Like SWNTs, the individual layers of MWNTs are entirely defined by  $(n,m)$ .

It has been confirmed, by HRTEM and Scanning Tunneling Microscopy (STM) techniques, that those carbon nanotubes are seamless cylinders derived from a graphene sheet. In the HRTEM image these rolled-up graphene sheets appear as straight line shown in Figure 1.5 (Zettl, unpublished) and Figure 1.6 (Iijima, 1991). A variety of cap structures are commonly observed and all the layers within the MWNT close at their tips. The structure of the caps is closely related to that of the icosahedral fullerenes, where the curvature is mediated by introducing pentagons and higher polygons into the structure at each carbon atom site.

Because of the different diameters of adjacent cylinders of carbon atoms in a MWNTs, the structural arrangement of the adjacent carbon honeycomb cylinders is essentially uncorrelated with no site correlation between carbon atoms on adjacent nanotubes (Tsang, 1994; Dujardin, 1994). The consequence of this interplanar stacking disorder is a decreased electronic coupling between the layers relative to graphite.

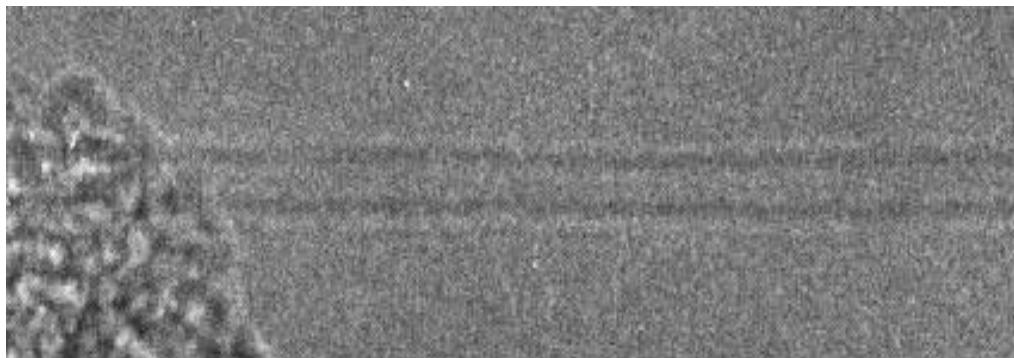


Figure 1.5: HRTEM image of a SWNT (Zettl, unpublished). The diameter of a SWNT is typically in the range of 1-2 nm.

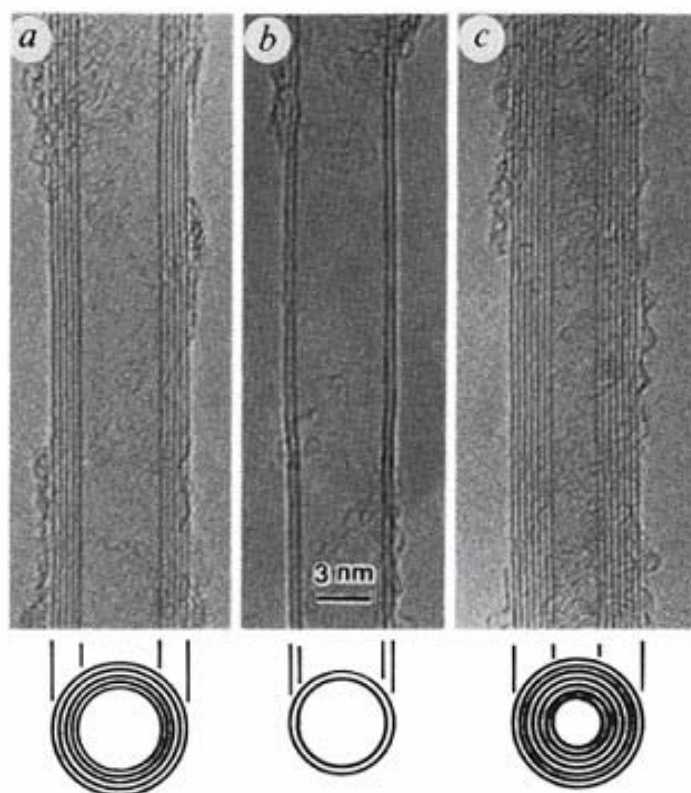


Figure 1.6: The observation by TEM of multi-walled coaxial nanotubes with various inner and outer diameters,  $d_i$  and  $d_o$ , and numbers of cylindrical shells  $N$  reported by Iijima in 1991: (a)  $N=5$ ,  $D_o=67$  Å; (b)  $N=2$ ,  $D_o=55$  Å; and (c)  $N=7$ ,  $D_i=23$  Å,  $D_o=65$  Å (Iijima, 1991).

### 1.3 Bonding between carbon atoms in carbon nanotubes

Carbon is the sixth element of the periodic table and has the lowest atomic number in column IV of the periodic table. Each carbon atom has six electrons, which occupy  $1s^2$ ,  $2s^2$ , and  $2p^2$  atomic orbitals. The  $1s^2$  orbital contains two strongly bound core electrons. Four more weakly bound electrons occupy the  $2s^2 2p^2$  valence orbitals. In the crystalline phase, the valence electrons give rise to  $2s$ ,  $2p_x$ ,  $2p_y$ , and  $2p_z$  orbitals, which are important in forming covalent bonds in carbon materials. Since the energy difference between the upper  $2p$  energy levels and the lower  $2s$  level in carbon is small compared with the binding energy of the chemical bonds, the electronic wave functions for these four electrons can readily mix with each other, thereby changing the occupation of the  $2s$  and three  $2p$  atomic orbitals so as to enhance the binding energy of the carbon atom with its neighboring atoms. The mixing of a single  $2s$  electron with one, two or three  $2p$  electrons is called  $sp^n$  hybridization with  $n=1,2,3$  (Dresselhaus, 1988). The various bonding states correspond to certain structural arrangements:  $sp$  bonding gives rise to chain structures,  $sp^2$  bonding to planar structures and  $sp^3$  bonding to tetrahedral structures. Recall that a carbon nanotube is a graphene sheet appropriately rolled into a cylinder, its bonding is essentially  $sp^2$  (Saito, 1998).

The curvatures of nanotubes mix a small amount of  $sp^3$  bonding so that the bonding in the circumferential direction is slightly weaker than along the nanotube axis. The single wall carbon nanotube has a small number of atoms around its circumference, this constraints leads to quantum confinement of the wavefunctions in the radial and circumferential directions, with essentially plane wave motion occurring only along the nanotube axis, which corresponds to a large number or closely spaced allowed wave

wavevectors (Dresselhaus, 2001). These confinement effects cause nanotubes to behave like one-dimensional objects as will be studied below.

The physical reason why these nanostructures form is that a graphene layer of finite size has many edge atoms with dangling bonds, and these dangling bonds correspond to high energy states. Thus the total energy of a small number of carbon atoms is reduced by eliminating dangling bonds, even at the expense of increasing the strain energy, thereby promoting the formation of closed cage clusters, such as, carbon nanotubes (Dresselhaus, 2001).

#### 1.4 Nanotube Growth Methods

Carbon nanotubes can be produced in several different ways. In this thesis, I will concentrate on arc-produced MWNTs, because of their structural perfection. For the sake of completeness, I also will briefly mention other methods to produce MWNTs and SWNTs.

##### 1.4.1 Arc-produced and Laser-Ablation

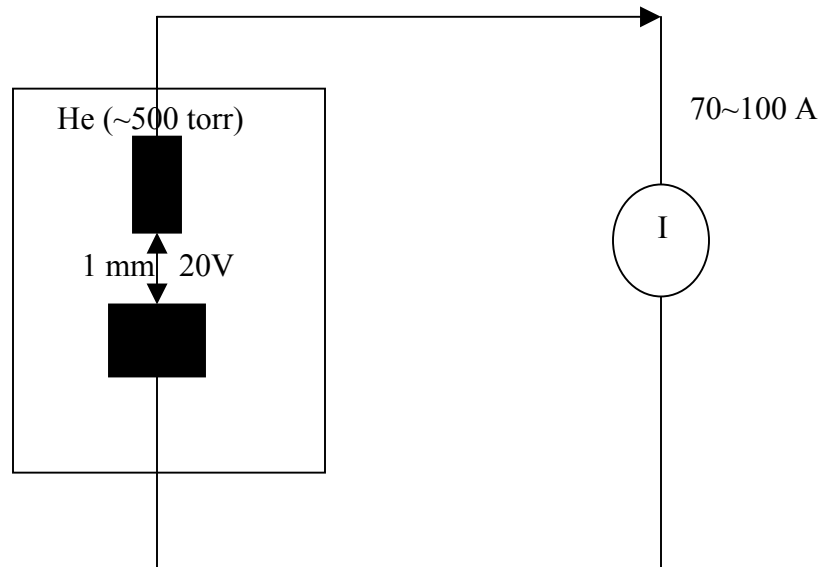
Both arc-produced and laser ablation methods are thought of involving the condensation of carbon atoms generated from evaporation of solid carbon sources. The temperatures involved in these methods are close to the melting temperature of graphite, 3000-4000°C (Iijima, 1991; Ebbesen, 1992; Thess, 1996).

The arc-produced method relies on a carbon arc where a current on the order 70 to 100 A passes through a graphite rod (which serves as the anode) to graphite cathode in a He atmosphere (Ebbesen, 1992). A schematic experimental setup is shown in Figure

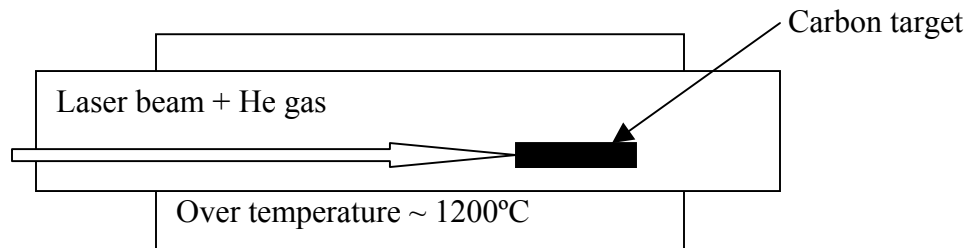
1.7(a). The potential difference between two rods is 20 V. It is assumed that carbon atoms are evaporated by plasma of helium gas ignited by high current passed through opposing carbon anode and cathode. In the arc process, a rod-shaped deposit forms on the cathode as shown in Figure 1.8(a). This deposit has a hard grayish outer shell, which houses a soft deep black material. This material consists of small fibers, which are used as samples in our experiments. These fibers, typically 1 mm in length and a fraction of a mm in diameter, are revealed to be dense bundles of MWNTs under HRTEM (see Figure 1.8(b) (Bonard, 1997)). Several hundred mg of raw material is produced in about 10 min. The material is quite heterogeneous and consists of MWNTs with a rather large dispersion in their outer and inner diameters as shown in Figure 1.8(b). The synthesized MWNTs are typically 10 nm in diameter (in the range of 5-30 nm) and are on the order of 1  $\mu$ m long. The nanotubes are typically bound together by van der Waals interactions and form tight bundles. Arc-produced MWNTs are very straight (shown in next section), indicative of their high crystallinity. Besides MWNTs, this method also produces rather large amounts of graphite materials in the form of multilayered fullerenes (or carbon onions) and amorphous carbon which covers the nanotubes shown in Figure 1.8(b). Purification steps (Forró, 1999; Bonard, 1997) are often used in experiments involving lithographically contacted nanotubes.

A variation of this synthesis method can be used to produce SWNTs (with diameters of the order of 1 nm), by replacing the graphite anode with a hollow graphite tube, which is filled with graphite powder containing powdered metal catalyst, such as, iron, nickel and cobalt (Bethune, 1993).

(a) Arc-produced



(b) Laser ablation



(c) Chemical Vapor Deposition (CVD)

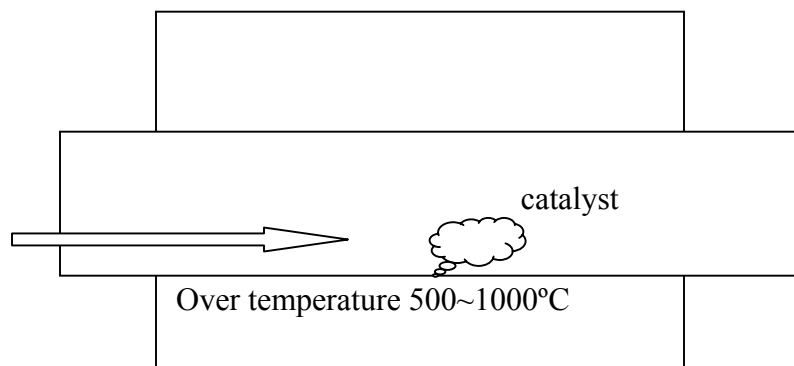


Figure 1.7: Schematic experimental setups for nanotube growth methods.

The method using arc-produce has been developed into an excellent method for producing both high quality MWNTs and SWNTs. MWNTs can be obtained by controlling the growth conditions such as the pressure of inert gas in the discharge chamber and the arcing current.

The laser ablation method utilizes intense laser pulse to ablate a carbon target in a He atmosphere shown in Figure 1.7(b). The target is placed in a tube-furnace heated to 1200°C (Thess, 1996). A flow of inert gas is passed through the growth chamber to carry the grown nanotubes downstream to be collected on a cold finger.

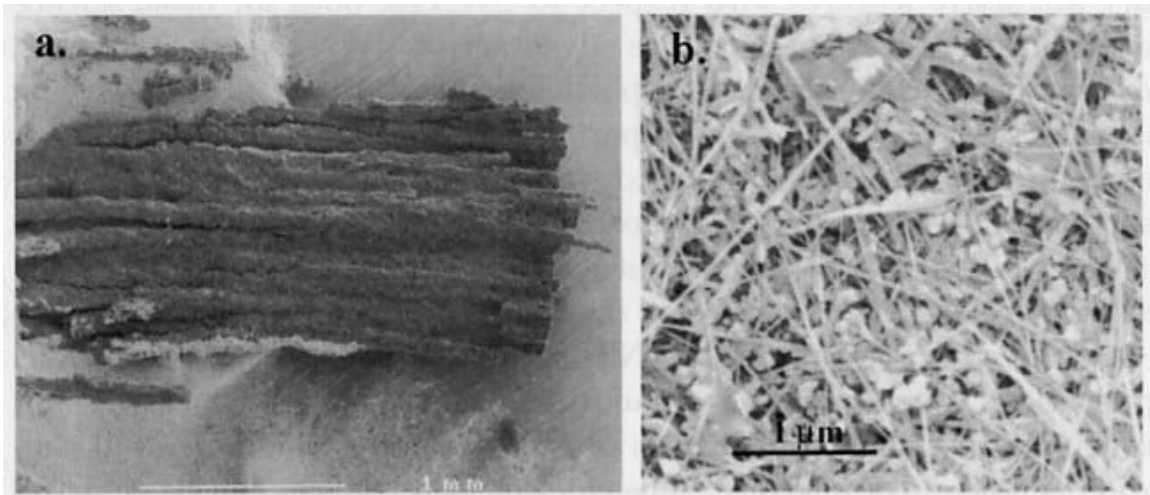


Figure 1.8: Scanning Electron Microscope image of the (a) rod-shaped deposit on the cathode and of (b) a zoomed part of a deposit, which shows the heterogeneous character of the arc-grown nanotube soot. (Bonard, 1997)

#### 1.4.2 Chemical Vapor Deposition (CVD)

A schematic setup for CVD growth is depicted in Figure 1.7(c). This nanotube production method is based on the thermal decomposition of hydrocarbons in the presence of a catalyst. It involves a catalyst material (like iron, nickel and cobalt

nanoparticles) supported on a substrate (like silica) in a tube furnace and a hydrocarbon gas flowing through the tube reactor. The growth temperature is typically held at 1100°C (Endo, 1995; Endo, 1993). Materials grown over the catalyst are collected upon cooling the system to room temperature. The key parameters in nanotube CVD growth are the nature of hydrocarbons, catalysts and growth temperature. The method is relatively simple to apply and produces nanotubes in large quantities. However, grown with catalytic particles, it affects transport of the tubes if residues remain. It's well-known that CVD grown MWNTs have large defect density (discussed below), which results in larger intrinsic resistance compared with the arc-produced MWNTs.

### 1.5 Structural quality of MWNTs grown by different methods

The HRTEM images of arc-produced and CVD grown MWNT are shown in Figure 1.9 and Figure 1.10.

The arc-produced MWNTs have generally the best structures (see Figure 1.9), presumably due to the high temperature of the synthesis process. It is likely that during the growth process, most of the defects are annealed (Tsang, 1994; Hiura, 1995). The MWNTs shown in Figure 1.9 are the ones used in our experiment.

Catalytically produced MWNTs (Dresselhaus, 2001) may be so defective that neither individual layers are distinguished; they may not even have an interior cavity. Many of these graphitic structures should rather be classified as nanoscopic graphite fibers, nevertheless, they are collectively called nanotubes, causing considerable confusion, since the transport properties vary considerably. The MWNTs described here are essentially defect-free multilayered straight tubular graphitic structures produced using the catalyst-free high temperature carbon-arc method (Ebbesen, 1992).

It should be noted that some defects are more difficult to visualize with HRTEM, like point defects, which consist of vacant sites and displacements of atoms to interstitial positions. These are quite costly in energy due to the strength of the C-C bonds, but these defects can be introduced by high-energy electron irradiation (Crespi, 1996). Ultrasonic treatment may also produce defects in MWNTs (Lu, 1996) and SWNTs (Liu, 1998), which become more susceptible to chemical attack after being subjected to high intensity ultrasound treatment. Defective structures may also result after chemical attack (i.e., in hot nitric acid and oxidation at elevated temperature), which has the effect of destroying the tips and opening the tubes. Figure 1.11 shows HRTEM images of arc-produced MWNTs after purified for 45 minutes in ambient air at 750°C and then dispersed in isopropanol and mixed ultrasonically (Roschier, 1999). Note the surface roughness of these treated MWNTs, which may affect the intrinsic resistance of the tubes and also the contact resistance between the tubes and the electrodes.

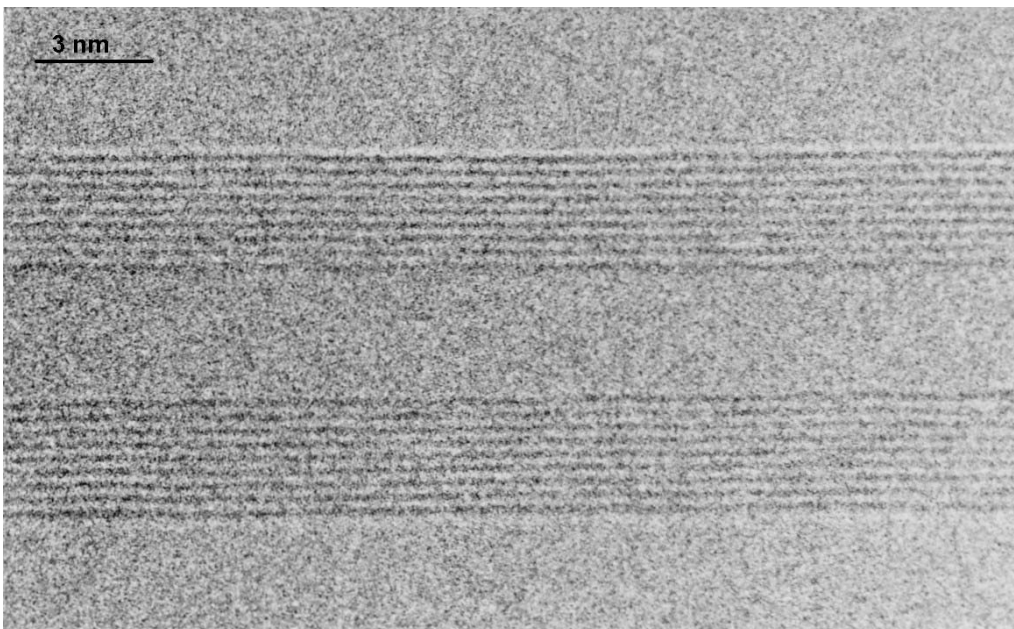


Figure 1.9: HRTEM image of an arc-produced MWNT. Each concentric layer can easily be seen (de Heer, unpublished).

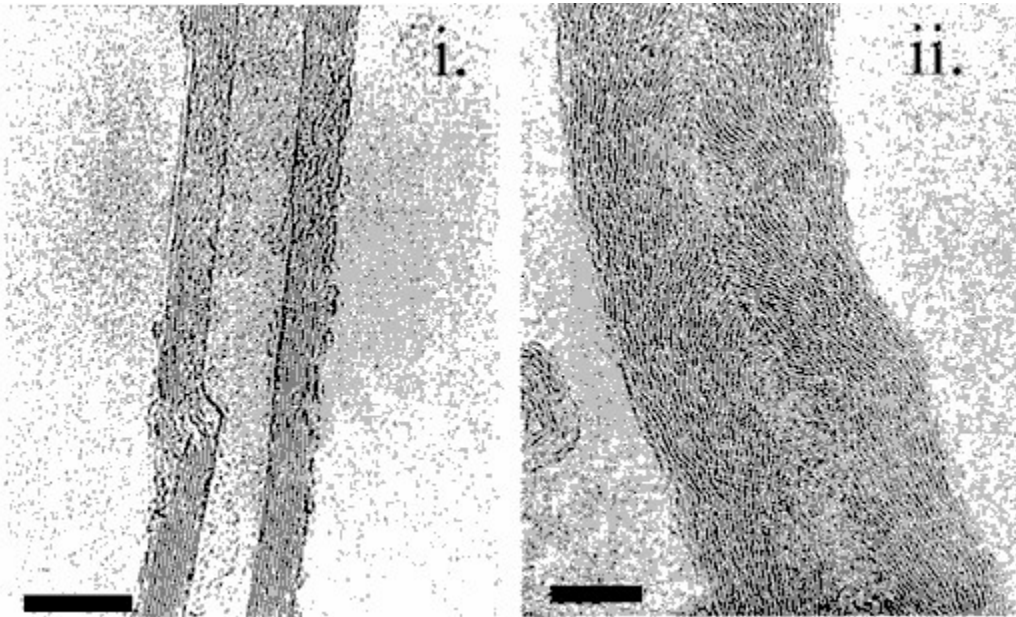


Figure 1.10: HRTEM images of CVD grown MWNTs, which produced by the decomposition of acetylene using a Co/silica catalyst, (i) at 720°C and (ii) at 900°C. All scale bars are 10 nm (Forró, 1999).

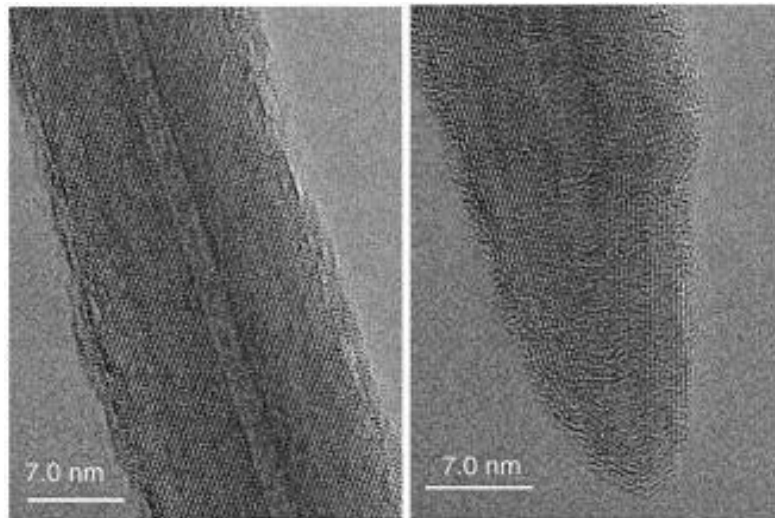


Figure 1.11: HRTEM images of arc-produced MWNTs after purified for 45 minutes in ambient air at 750°C and then dispersed in isopropanol and mixed ultrasonically. (Roschier, 1999). Note the surface roughness of these treated MWNTs.

CHAPTER 2  
ELECTRONIC STRUCTURE AND TRANSPORT PROPERTIES  
OF CARBON NANOTUBES

In this chapter I will introduce the basic concepts and theoretical expectations for transport properties of carbon nanotubes. First tight-binding calculations are used to obtain a simple approximation for the electronic structure of graphene and carbon nanotubes (Mintmire, 1992; Saito, 1992; Saito, 1998). Then the basics of transport of one-dimensional conductors are explained according to the Landauer Model (Landauer, 1989). Then the transport properties of carbon nanotubes are introduced.

### 2.1 Electronic Structures

Recall that three of four valence electrons of carbon, one s-electron and two p-electrons, form the  $sp^2$ -hybrid which has trigonally directed  $\sigma$  bonds in a plane. In the solid, these directed  $\sigma$  orbitals form strong covalent bonds with the  $\sigma$  orbitals from neighboring carbon atoms. The fourth (i.e. the third  $2p$ ) electron is in a  $2p_z$ -orbital perpendicular to the plane and forms a weaker  $\pi$  bond with the  $2p_z$ -orbitals of neighboring C atoms. The resulting  $\pi$ -bands define the Fermi surface and hence they are responsible for the transport properties (Fink, 2001). In contrast, the mechanical properties are mainly caused by the strong covalent bond between the tightly-bund  $\sigma$ -orbitals.

In this section, I will introduce the structure and electronic properties of 2D graphite (graphene) first, and then explain the structure and electronic properties of SWNTs and MWNTs.

### 2.1.1 Structure of graphene

Recall that graphene is a single sheet of carbon atoms arranged in a honeycomb structure. In Figure 2.1, the unit cell (a) and the Brillouin zone (b) of graphene are shown as the dotted rhombus and shaded hexagon, respectively, where  $\vec{a}_1$  and  $\vec{a}_2$  are unit vectors in real space, and  $\vec{b}_1$  and  $\vec{b}_2$  are reciprocal lattice vectors.

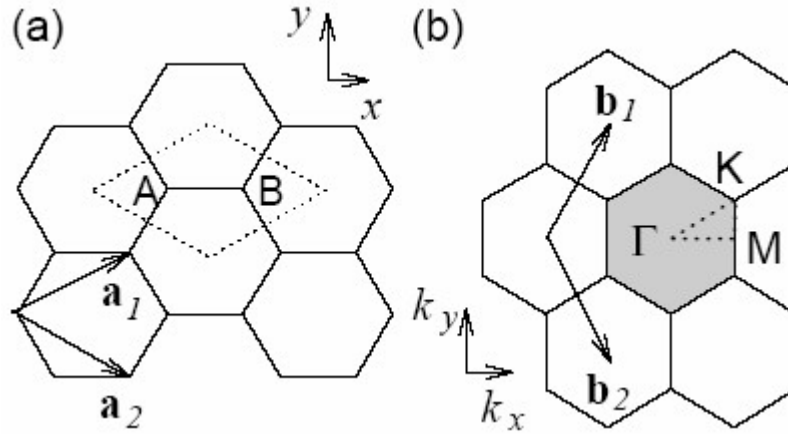


Figure 2.1: (a) The unit cell and (b) Brillouin zone of graphene are shown as the dotted rhombus and shaded hexagon, respectively.  $\vec{a}_i$  and  $\vec{b}_i$  ( $i = 1; 2$ ) are unit vectors and reciprocal lattice vectors, respectively.  $\Gamma$ , K and M are defined as the center, the corner and the center of the edge of the Brillouin zone, respectively (picture from Saito, 1998).

The unit vectors can be written as:

$$\begin{aligned}\vec{a}_1 &= a_0 \sqrt{3} (1/2, \sqrt{3}/2) \\ \vec{a}_2 &= a_0 \sqrt{3} (-1/2, \sqrt{3}/2)\end{aligned}\tag{2.1}$$

in the  $(x,y)$  basis (Saito, 1998) and with  $a_0$  denoting the nearest neighbor distance,  $a_0=1.42 \text{ \AA}$ . The  $p_z$  atomic-orbitals are oriented perpendicular to the plane.

The primitive reciprocal vector  $\vec{b}_1$  and  $\vec{b}_2$  are given by

$$\vec{b}_1 = \left( \frac{2\pi}{\sqrt{3}a}, \frac{2\pi}{a} \right) \quad \text{and} \quad \vec{b}_2 = \left( \frac{2\pi}{\sqrt{3}a}, -\frac{2\pi}{a} \right) \quad (2.2)$$

Here  $a = \sqrt{3}a_0$  and  $|\vec{b}_{1,2}| = \frac{4\pi}{3a_0}$  is a lattice constant in the reciprocal space (Saito, 1998).

Since there are two  $\pi$  electrons per unit-cell, there will be two  $\pi$ -bands (the  $\pi$  and  $\pi^*$  bands). Note that the even number of electrons per unit-cell makes it impossible to determine *a priori* whether the material will be metallic or semiconducting (Schönenberger, 2000).

### 2.1.2 Electronic structure of $\pi$ bands for graphene

Tight-binding calculation considers only nearest-neighbor interactions of carbon atoms. From the tight-binding calculation for  $\pi$  electrons of graphene, a simple approximation for the electronic structure of a graphene layer can be obtained:

$$E_{g2D}(k_x, k_y) = \pm \gamma_1 \sqrt{1 + 4 \cos\left(\frac{\sqrt{3}k_x a}{2}\right) \cos\left(\frac{k_y a}{2}\right) + 4 \cos^2\left(\frac{k_y a}{2}\right)} \quad (2.3)$$

which refers to an on-site energy integral equal to zero, since the on-site integral is small compared with the nearest-neighbor overlap integral and can be neglected. Here  $\gamma_1$  is the nearest-neighbor overlap energy integral, and  $a = \sqrt{3}a_0$  is the lattice constant (Mintmire, 1992; Saito, 1998).  $\gamma_1 \approx -3$  eV for  $\pi$  bands of carbon atoms in graphene (Painter, 1970).

The plot of the electronic structure of graphene using tight-binding calculations for  $\pi$  electrons is shown in Figure 2.2 (Schönenberger, 2000). The valence and conductance bands touch and are degenerate at six  $K(k_F)$  points at the 2D Brillouin zone corner where the Fermi level in reciprocal space is located. Therefore, graphene is a zero-

gap semiconductor. Note that there is no state anywhere at Fermi level but at the K points. The inset in Figure 2.2 shows the electronic structure in the vicinity of the Fermi level.

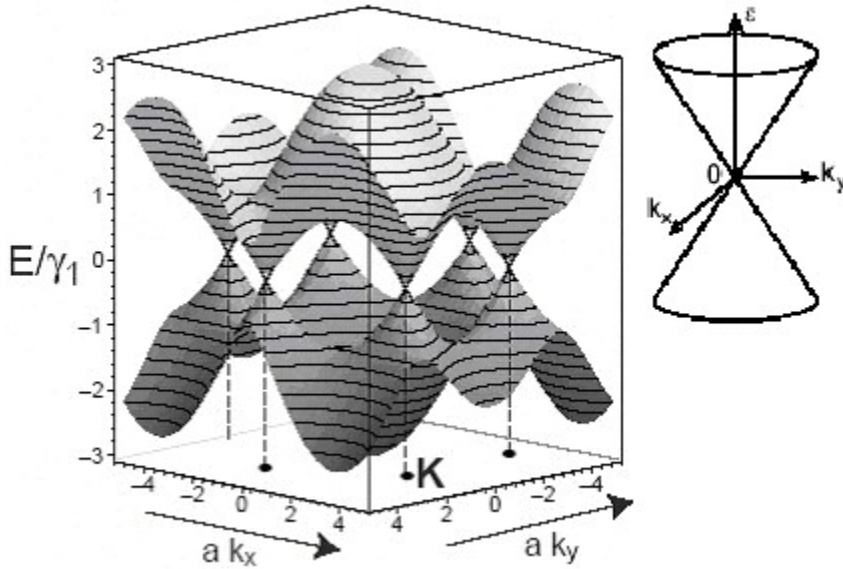


Figure 2.2: The electronic structure of graphene using tight-binding calculations for  $\pi$  electrons (Schönenberger, 2000). Here  $\gamma_1$  is the nearest-neighbor overlap integral. The inset shows the electronic structure in the vicinity of the Fermi level of graphene.

All of the predictions of this tight-binding calculation around the Fermi level have proved to be in good agreement with the first-principles results (Mintmire, 1992).

### 2.1.3 Electronic Structure of Single-Wall Carbon Nanotubes

The electronic structure of a carbon nanotube is closely related to that of graphene. By using the periodic boundary conditions in the circumferential direction imposed by  $C_h$  (see Figure 1.3), the wave vector  $K_1$  associated with the  $C_h$  direction becomes quantized, while the wave vector  $K_2$  associated with the direction of the

translational vector  $T$  along the nanotube axis remains continuous for a nanotube of infinite length. Figure 2.3 shows the reciprocal lattice vectors,  $K_1$  and  $K_2$ , for a  $C_h = (4,2)$  chiral nanotube. The wavevectors of a carbon nanotube are indicated by the parallel lines since  $K_1$  is discrete and  $K_2$  is continuous. The length of all the parallel lines is  $2\pi/T$  which is the length of the one-dimensional first Brillouin zone. Thus the energy bands consist of a set of one-dimensional energy dispersion relations, which are cross-sections of those for graphene (see Figure 2.2).

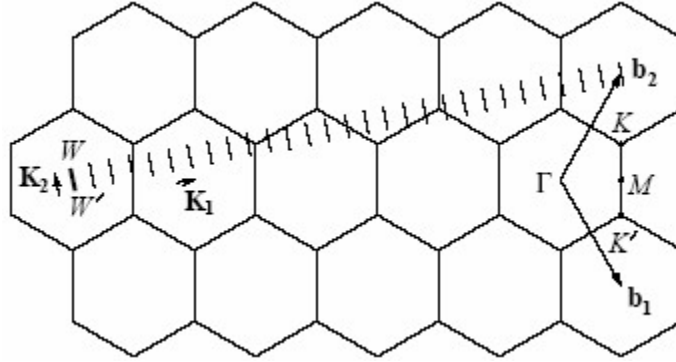


Figure 2.3: The reciprocal lattice vectors,  $K_1$  and  $K_2$ , for a  $C_h = (4,2)$  chiral nanotube. The vectors  $K_1$  and  $K_2$  are reciprocal lattice vectors corresponding to  $C_h$  and  $T$ , respectively. The line segment  $WW'$ , which is parallel to  $K_2$ , represents the Brillouin zone of the nanotube. The figure corresponds to  $C_h = (4, 2)$ ,  $T = (4, -5)$ ,  $K_1 = (5b_1 + 4b_2)/28$ ,  $K_2 = (4b_1 - 2b_2)/28$  [Saito, 1998].

The reciprocal lattice vectors  $K_1$  and  $K_2$  can be obtained from the following relations,

$$\begin{aligned} C_h \cdot K_1 &= 2\pi, & T \cdot K_1 &= 0 \\ C_h \cdot K_2 &= 0, & T \cdot K_2 &= 2\pi \end{aligned} \quad (2.4)$$

If for a particular  $(n,m)$  nanotube, the cross-section line passes through a  $K$  point of the 2D Brillouin zone, where the conductance and valence energy bands of graphene

are degenerate by symmetry, the one-dimensional energy bands have a zero energy gap. In this case, the density of states at the Fermi level has a finite value for these carbon nanotubes, and they therefore are metallic. If, however, the cross-section line does not pass through a  $K$  point, then the carbon nanotube is expected to show semiconducting behavior, with a finite energy gap between the valence and conduction bands.

The condition for obtaining a metallic energy band is that the ratio of the length of the vector  $\vec{YK}$  to that of  $K_1$  (in Figure 2.4) is an integer (Saito, 1998). Since the vector  $\vec{YK}$  is given by

$$\vec{YK} = \frac{2n+m}{3} K_1 \quad (2.5)$$

The condition for metallic nanotubes is that  $(2n+m)$  or equivalently  $(n-m)$  is a multiple of 3. In particular, the armchair nanotubes denoted by  $(n, n)$  are always metallic, and the zigzag nanotubes  $(n, 0)$  are only metallic when  $n$  is a multiple of 3.

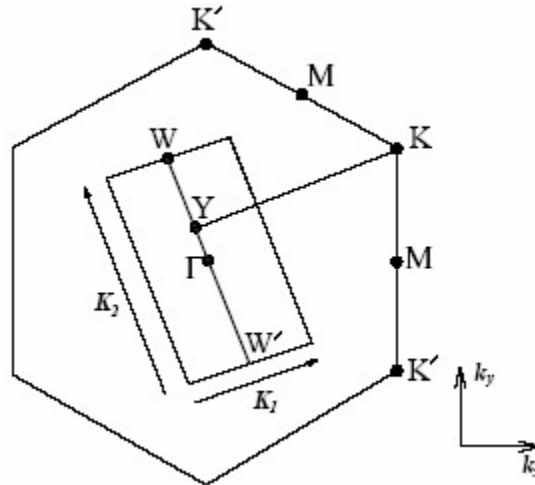


Figure 2.4: The condition for metallic energy bands: if the ratio of the length of the vector  $\vec{YK}$  to that of  $K_1$  is an integer, metallic energy bands are obtained (Saito, 1998).

Figure 2.5 shows which carbon nanotubes are metallic and which are semiconducting, denoted by open and solid circles, respectively. From Figure 2.5, it follows that approximately one third of the carbon nanotubes are metallic and the other two thirds are semiconducting.

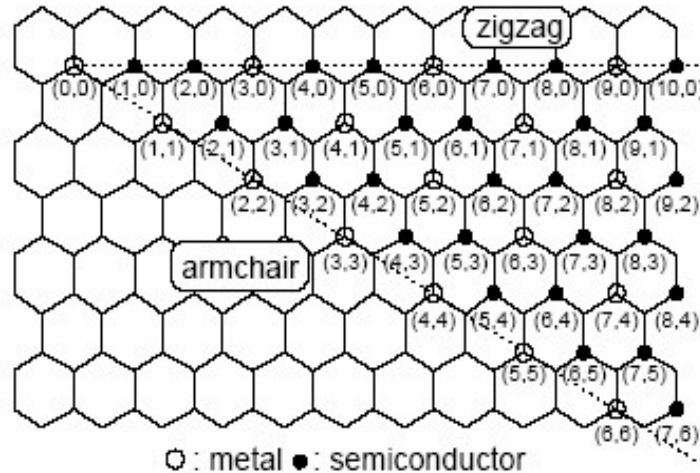


Figure 2.5: The carbon nanotubes  $(n, m)$  that are metallic and semiconducting, respectively, are denoted by open and solid circles on the map of chiral vectors  $(n, m)$ . For very small diameter nanotubes (e.g.,  $d_t < 0.7$  nm), the tight binding approximation is not sufficiently accurate, and more detailed approaches are needed. For example, small diameter nanotubes, such as the  $(4,2)$  nanotube is predicted to be semiconducting by tight binding approximation, though more detailed calculations show  $(4,2)$  to be metallic (Saito, 1998).

The achiral armchair  $(n,n)$  and zigzag  $(n,0)$  nanotubes have the highest symmetry. The calculated 1D electronic structures of a  $(5, 5)$  armchair nanotube,  $(9,0)$  and  $(10,0)$  zigzag nanotubes are shown in Figure 2.6.

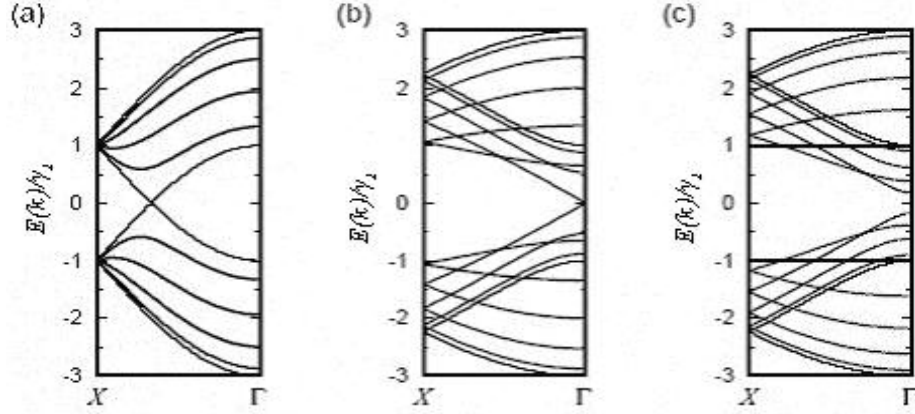


Figure 2.6: One-dimensional electronic structures for (a) armchair (5, 5), (b) zigzag (9, 0), and (c) zigzag (10, 0) carbon nanotubes. The X points for armchair and zigzag nanotubes correspond to  $k_z = \pm\pi/a$  and  $k_z = \pm\pi/\sqrt{3}a$ , respectively. Here  $\gamma_1$  is the nearest-neighbor overlap integral (Saito, 1992).

All (n, n) armchair nanotubes have a band degeneracy between the highest valence band and the lowest conduction band at  $k_z = \pm 2\pi/(3a)$ , where the bands cross the Fermi level. Thus, all armchair nanotubes are expected to exhibit metallic conduction, similar to the behavior of 2D graphene sheets (Saito, 1992).

Since n-m is a multiple of 3, there is no energy gap for the metallic (9, 0) nanotube at  $k = 0$ , whereas the (10, 0) nanotube has an energy gap.

Figure 2.7 shows the electronic structure of a (12,6) chiral nanotube. Two bands, which called  $\pi$  and  $\pi^*$  bands respectively, cross the Fermi level at the same wave vector, exhibiting a metallic nature. The Fermi wave vector is slightly displaced from the ideal  $K$  point (discussed below) shown by an arrow in the figure (Hamada, 1992).

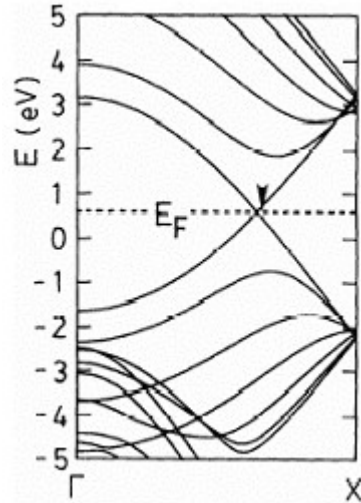


Figure 2.7: Electronic structure of nanotube (12, 6). The X point has a wave number near  $\pi/a$ . The arrow shows a wave vector corresponding to the  $K$  point (Hamada, 1992).

The density of states of nanotubes is energy-dependent. Figure 2.8 compares the density of states for metallic (9, 0) and semiconducting (10, 0) zigzag nanotubes. The density of states at  $E_F$  has a value of zero for semiconducting nanotubes, but it is non-zero (and smaller than 0.1 states/unit cell of graphite) for metallic nanotubes. Note also the van Hove singularities (discussed below). The flatness and linearity of density-of-states in Figure 2.8(b) show that no dispersion occurs in the vicinity of the Fermi level. The comparison between the 1D density of states for the nanotubes and the 2D density of states for a graphene layer is included in the figure.

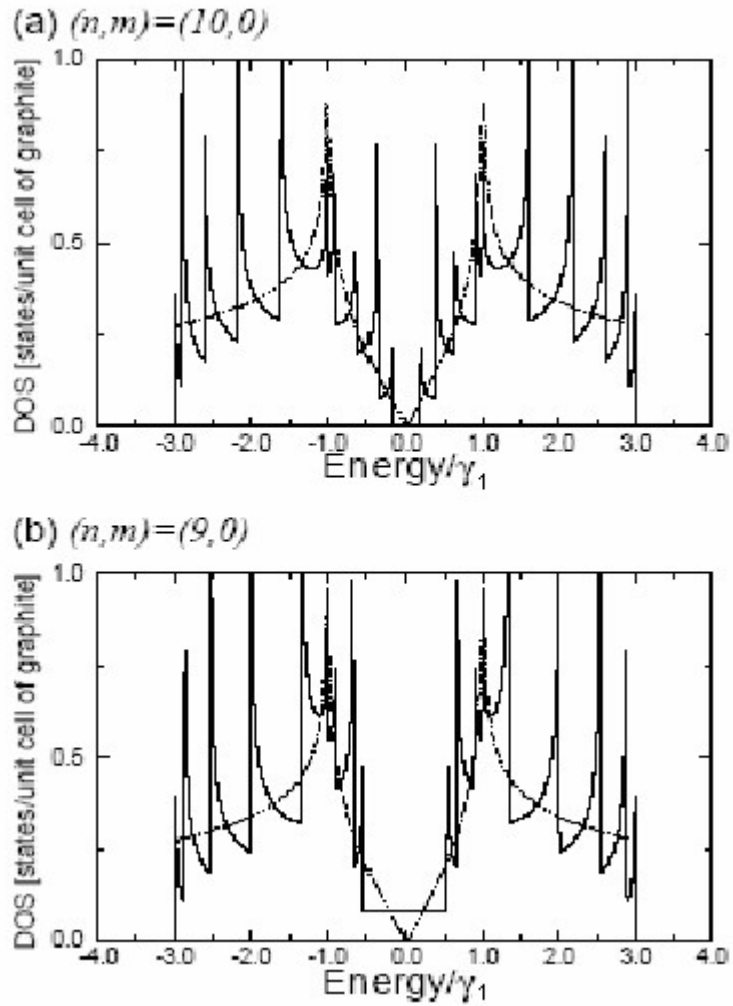


Figure 2.8: Electronic 1D density of states per unit cell of a 2D graphene sheet for two  $(n, 0)$  zigzag nanotubes: (a) the  $(10, 0)$  nanotube which has semiconducting behavior, (b) the  $(9, 0)$  nanotube which has metallic behavior. Also shown as a dashed line in the figure is the density of states for the 2D graphene sheet (Saito, 1993).

Van Hove Singularities (VHS) are signature features in the Density of States (DOS) of a material that appear at the band edges, i.e. at extrema in  $E(k)$ . The VHS of nanotubes, as 1D conductors, are manifested as peaks, since the density of states is proportional to  $(\frac{\partial E}{\partial K})^{-1}$  and  $(\frac{\partial E}{\partial K})$  is zero at the band edge (shown in Figure 2.8).

Theoretically the band-gap for semiconducting nanotubes is of the order of  $\Delta E_{sc} = 2|\gamma_1|a_0/D$ , where  $|\gamma_1| \sim 3$  eV and  $a_0 = 0.14$  nm for graphite and nanotubes, and  $D$  is the diameter of the tube in nm (Kelly, 1981; Venema, 2000). For example, for a 15 nm diameter tube,  $\Delta E_{metal} = 0.056$  eV.

From above, for semiconducting (n,0) and (n,m) tubes, their energy gaps depend inversely on diameter. For metallic tubes (n,0) and (n,m), the curvature of the tubes leads to mixing of the  $\pi/\sigma$  bonding and  $\pi^*/\sigma^*$  antibonding orbitals in carbon. This mixing causes the band crossing ( $k_F$ ) of graphene to shift away from the  $K$  point and produce small gaps (on the order of 0.01 eV) in (n,0) and (n,m) metallic tubes with the magnitude of the gap depending inversely with the square of the diameter (Hamada, 1992; Kane, 1997). Note that this small gap is negligible for nanotubes with large diameters. For metallic (n,n) armchair tubes, they are truly metallic since  $k_F$  remains on the subband of the nanotube (Crespi, 1997).

For metallic undoped tubes, two 1D subbands with a linear dispersion cross exactly at the Fermi level. These are the metallic subbands which give the tube its metallic character. Those subbands do not cross the Fermi level, and hence I refer to them as the semiconducting subbands. Systems of unoccupied and occupied levels of the semiconducting subbands of the metallic tubes are symmetrically positioned above and below the Fermi level with a structure that resembles that of the semiconducting

nanotubes. The gap between the system of unoccupied and occupied levels of semiconducting subbands in metallic nanotubes is three times as large as for the semiconducting tubes (Odom, 1998; Wildover, 1998), that is,  $\Delta E_{metal} = 6|\gamma_1|a_0/D$  (White, 1998; Charlier, 1998). For example, for a 15 nm diameter tube,  $\Delta E_{metal} = 0.17$  eV. These gap sizes have been verified experimentally by Venema *et al.* (Venema, 2000). Note that  $\Delta E_{metal} \gg kT$  for  $T = 300$  K for the typical MWNT diameters ( $D = 5\sim 25$  nm). Hence at room temperature and for bias voltages  $V < \Delta E_{metal}$ , only the metallic subbands are expected to contribute to the transport.

Figure 2.9 shows the band structure calculated in the tight-binding approximation of a (100,100) nanotube by de Heer (Berger, 2002). This is a conducting tube with a diameter  $D = 13.6$  nm (typical value for the nanotubes used in our studies) and  $\Delta E_{metal} = 0.18$  eV. Its density of states is shown in Figure 2.10 (calculated by de Heer (Berger, 2002)). The VHS produce a set of approximately equally spaced spikes. The DOS at room temperature is also shown, which is superimposed in Figure 2.10. Note the VHS which are largely washed out due to the increasing value of  $KT$  at room temperature. The properties of this tube are representative of all conducting nanotubes of this diameter.

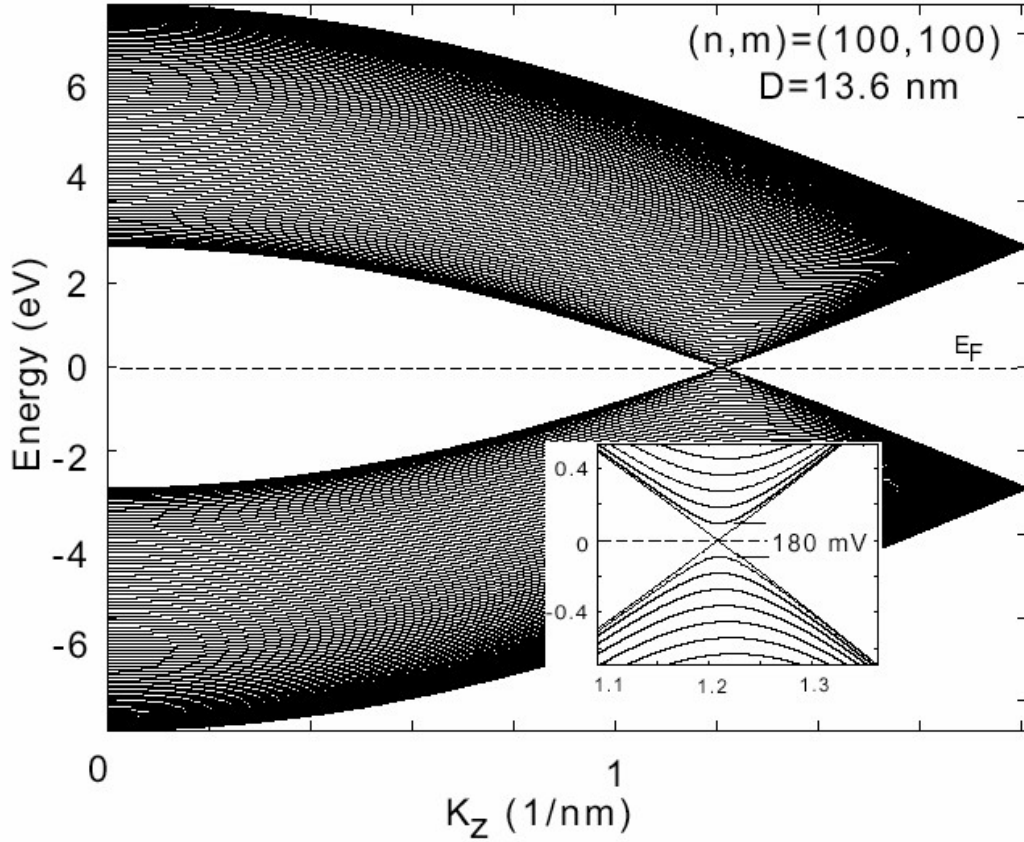


Figure 2.9: The 1D electronic bands of a  $(n,m)=(100,100)$  carbon nanotube calculated in the tight binding model with  $|\gamma_1|=2.9$  eV and  $a_0=0.142$  nm, where the energy of the subbands are plotted versus  $K_z$  (the wave number along the tube) (Berger, 2002). This  $D = 13.6$  nm diameter nanotube is in the range of diameters typical of the nanotubes studied here (i.e.  $5\text{nm} < D < 20\text{nm}$ ). The electronic transport in this metallic nanotube is due to the two subbands that cross the Fermi level (see inset). Above and below the Fermi level are two sets of semiconducting subbands. The gap between these is  $E_{gap} = 6 |\gamma_1| a_0 / D = 180$  mV ( $\sim 7 kT$  at room temperature, note that for semiconducting tubes with the same diameter, the gap is a factor of 3 smaller). The transport properties of the conducting subbands are unique and characterized by very low back scattering compared with the semiconducting bands (White, 1998; Charlier, 1998).

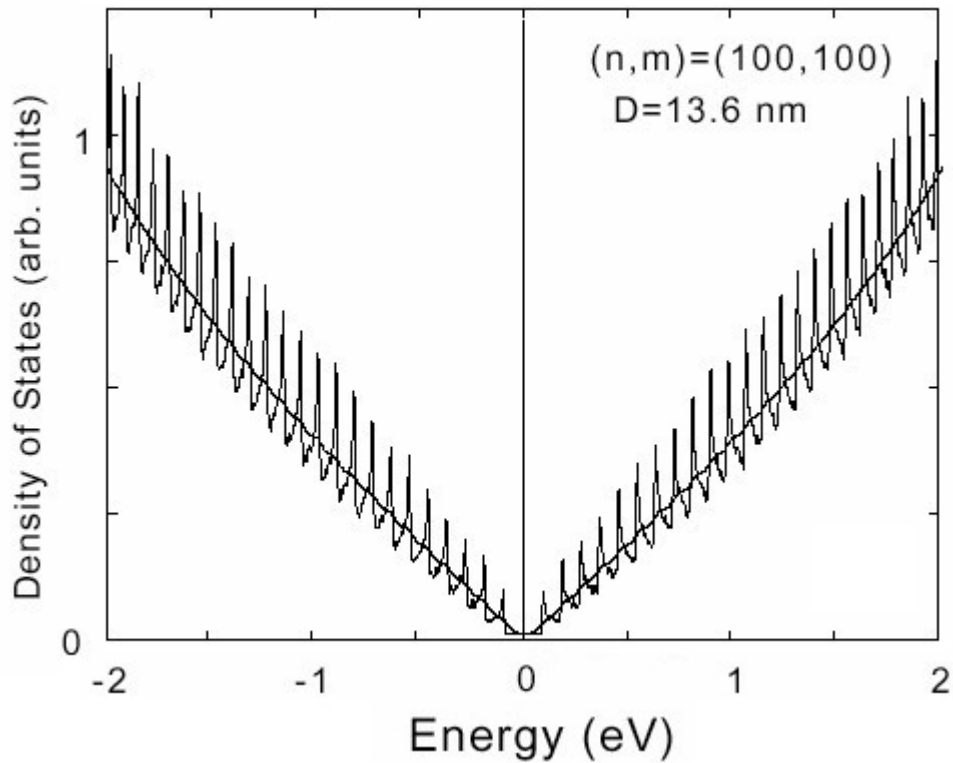


Figure 2.10: The density of states versus energy of the nanotube shown in Figure 2.9 (Berger, 2002). The typical van Hove singularities, which occur when the energy coincides with the bottom of the subbands, produce a set of approximately equally spaced spikes. Superimposed is also the DOS after gaussing smoothing with  $\Delta E = 25$  mV to simulate effect of room temperature. This results in a nearly linear dependence of the DOS with energy. For  $|E| < E_{gap}/2 = 90$  mV the DOS is essentially constant (White, 1998; Charlier, 1998).

The scattering properties of the metallic subbands and the semiconducting subbands of metallic nanotubes are very different. For the former, back scattering is forbidden due to the fact that they are essentially of pure  $\pi$  (bonding) and  $\pi^*$  (anti-bonding) character, in contrast to the semiconducting subbands which are of mixed character and consequently can back-scatter (White, 1998; McEuen, 1999). Hence, even if the states above the gap become populated (thermally, by doping, or by large biasing voltages), it should be expected that (for long nanotubes) the two conducting subbands provide the primary contribution to the current. Thus, it is theoretically expected that the scattering in the metallic subbands of metallic nanotubes is much smaller than in the (doped or thermally populated) semiconducting subbands of the same nanotubes.

Indeed, transport properties of metallic SWNTs and those of doped semiconducting tubes have been measured (McEuen, 1999). The mean free paths of the latter have been found to be much shorter than those of the metallic SWNTs, because the doping introduces scattering centers to the tubes. This confirms the predicted unique low scattering properties of the metallic subbands (White, 1998; Ando, 1998).

The band structure of SWNTs (both metallic and semiconducting) has been experimentally verified (Wildoer, 1998; Odom, 1998). In the tunneling experiments, Schonenberger *et al.* have shown that the electronic density of states of MWNTs corresponds to the theoretical predictions (Schonenberger, 1999). It is similar in structure to a SWNT however with the expected reduced gap size due to the larger diameters.

#### 2.1.4 Multi-walled nanotubes: structure and properties

In the aspect of physical properties, MWNTs present several attractive features compared with SWNTs. They can be grown without magnetic catalytic particles, which affect transport if residues remain. The MWNTs with larger diameters enable to study quantum interference phenomena (Schonenberger, 1999). The more robust structure allows better mechanical stability and higher rigidity, which may be advantageous for applications (i.e. scanning probe tips). As for graphite, the distance between layers of MWNTs is large and the interlayer coupling is weak.

Recall that a MWNT is composed of nested SWNT layers. According to Roche (Roche, 2001), the two consecutive layers of MWNTs are commensurate, if the ratio of their translational vectors  $T_{(n,m)}$  is a rational number, such as, a double-walled nanotube  $(9,0) @ (18,0)$ . Otherwise, they are incommensurate, such as, a double-walled nanotube  $(9,0) @ (10,0)$ . The commensurate layers have interlayer coupling, which resulting in the periodic system. However, for the incommensurate layers, the coupling strengths between nearest-neighbors carbon atoms located at different layers are not translationally invariant along the tube axis. The system is therefore not periodic and the interlayer coupling is different from the commensurate case, and much weaker (Roche, 2001). The probability of having commensurate consecutive layers is much smaller than the one of having incommensurate layers. In this sense, I am only focusing on the incommensurate cases and thus the interlayer coupling can be neglected. Hence the electronic properties of MWNTs are closely related to those of SWNTs (Dresselhaus, 2001). To a certain degree, MWNTs can be viewed as decoupled and unconnected single nanotube layers.

Experimentally MWNTs are found to be either conducting or non-conducting. Since only one in three layers is conducting, if a MWNT is found to conduct, then it is because the outer layer is conducting. In contrast, a MWNT does not conduct when the outer layer is semiconducting.

In short, the transport properties of a MWNT are associated with those of the outer layer, which makes it (like SWNTs) a one-dimensional conductor. In order to fully appreciate the consequences of this, a short review of one-dimensional conductors is necessary.

## 2.2 Basics of One-Dimensional Transport

This section will first introduce the Landauer model to describe mesoscopic transport. The conductance of carbon nanotubes as one-dimensional conductors is discussed next. Details can be found in various reviews and textbooks (e.g. Landauer, 1989; Datta, 1995).

There are two characteristic lengths in a mesoscopic system, which will be used below. The first one is the momentum relaxation length (or mean free path)  $L_m$ , which is the average length that an electron travels before it is scattered by a scattering center. The second one is the Fermi wavelength  $\lambda_F$ , defined by  $\lambda_F = 2\pi/k_F$ , which is the de Broglie wavelength for electrons at the Fermi energy.

### 2.2.1. Resistance of a ballistic conductor

Figure 2.11 shows a narrow two-dimensional conductor with width  $W$  and length  $L$  ( $W \ll L$ ), sandwiched between two large contacts. According to Ohm's law, its

conductance is given by  $G = \sigma \frac{W}{L}$  ( $W \ll L$ ), here the conductivity  $\sigma$  is a material parameter independent of the sample dimensions. However, this ohmic behavior is true only for large dimensions of the conductor.

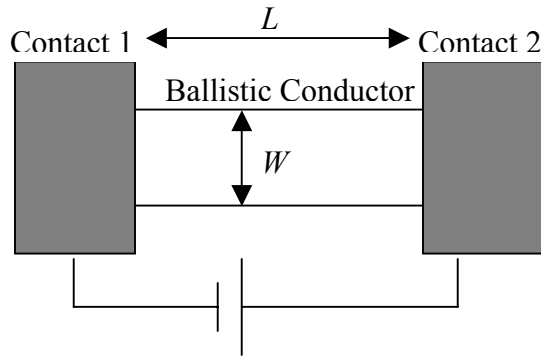


Figure 2.11: A narrow two-dimensional conductor with width  $W$  and length  $L$  ( $W \ll L$ ) sandwiched between two contacts across which an external bias is applied.

When the width ( $W$ ) is large, the associated wavevectors are approximately continuous and there are a large number of conducting bands available. The conductance of this narrow conductor is proportional to  $W$ . When  $W$  is small (on the order of  $\lambda_f$ ), the associated wavevectors become discrete and separated by  $2\pi/W$ . Each wavevector corresponds to a conducting band. Therefore, there are only a limited number of bands available. The conductance of this conductor is not proportional to the width  $W$ . Instead it depends on the number of available bands.

When the width ( $W$ ) is small and the length ( $L$ ) is reduced, then one would expect the conductance of this narrow conductor to grow infinitely if this relation still holds. However, this is not observed experimentally. It is found that the measured conductance approaches a limiting value  $G_c$ , when the length of the conductor becomes shorter than the mean free path ( $L < L_m$ ). The mean free path in this context refers to the momentum

scattering length  $L_m$ , which includes any process that alters the electronic momentum and hence affects the resistance. In this limit, the conductor is ballistic (an ideal conductor without scatters), and so it should have zero scattering resistance. The observed resistance  $R_c = G_c^{-1}$  arises not from scattering in the conductor but rather from the interface between the conductor and the contact. The contacts with large width have more conducting bands available, but the narrow conductor with a small width has only a few available bands. This requires a redistribution of the current at the interface leading to the interface resistance. The contact resistance  $R_c$  is ultimately determined from quantum mechanical considerations discussed in the next section.

### 2.2.2 Landauer formula

As explained above, when the dimension ( $W$  and/or  $L$ ) is made small, the ohmic behavior breaks down. Firstly there is an interface resistance independent of the length  $L$  of the sample. Secondly the conductance does not decrease linearly with the width  $W$ . Instead it depends on the number of subbands in the conductor and goes down in discrete steps. These changes have to make to the Ohm's law.

Landauer's formula incorporates both of these features (Landauer, 1989; Datta, 1995):

$$G = G_0 N T \quad (2.6)$$

The factor  $T$  represents the average probability that an electron injected at one end of the conductor will transmit to the other end, which is determined by the properties of the conductor and also the contacts.  $N$  is the number of available conducting subbands inside

the conductor.  $G_0 = 2e^2/h = (12.9 \text{ K}\Omega)^{-1}$  is the conductance quantum. This model has proved to be very useful in describing mesoscopic transport.

According to the Landauer equation (Eq. (2.6)), in the ideal case, a ballistic conductor with perfect contacts (i.e. transparency=1, no back reflection), the transmission probability ( $T$ ) is unity, the conductance of the system with  $N$  conducting subbands is  $NG_0$  due to the contact resistance.

In the non-ideal case the transmission is reduced due to back-scattering in the narrow conductor and imperfect contacts. Assume the transmission coefficients of all the conducting channels are  $T$  ( $0 \leq T \leq 1$ ), then  $G = NTG_0$ . This resistance can be divided into two parts: the contact resistance originating in the transition to the contacts and the residual scatter's resistance due to the narrow conductor and imperfect contacts:

$$G^{-1} = (NT_1G_0)^{-1} = G_c^{-1} + G_s^{-1} \quad (2.7)$$

here  $G_c^{-1} = 1/NG_0$  and  $G_s^{-1} = 1/(NG_0) \cdot (1-T)/T$  (Datta, 1995). The contact resistance  $G_c^{-1}$  is inversely proportional to the number of available conducting subbands  $N$ . The contact resistance of a single-band conductor is about 12.9 K $\Omega$ . And if  $N$  is very large, the contact resistance may become very small. In that case, the scatter resistance  $G_s^{-1}$  dominates, which is determined by the properties of the scatter, that is, the transmission probability  $T$ . In the case, a ballistic conductor with imperfect conducts, the reduced transmission probability  $T$  is only due to back-scattering in the contacts. Similarly, in the case, a conductor with perfect contacts, the reduced transmission probability  $T$  is due to back-scattering in the conductor only.

Our experiment is designed to discriminate the different origins of the reduced transmission probability  $T$ . As mention earlier, in our experiment, a fiber of MWNTs was

gently lowered into liquid metal. The resistance of a single nanotube sticking out from the fiber can be measured by dipping the tubes to different depths. This also allows the measurement of the resistance as a function of the depth of the tube. If the contact resistance and the scattering resistance (due to the contacts) remain constant, the scattering resistance due to the conductor itself can be distinguished, which varies as the length of the tube changes. Choosing liquid metal as a contact makes the measurements possible.

### 2.3 Transport properties of carbon nanotubes

A metallic SWNT has two conducting subbands as explained previously (refer to section 2. 1.3). For an ideal case, a ballistic SWNT with ideal contacts, the transmission coefficient for both subbands equals to unity. According to the Landauer equation (Eq. (2.6)), the conductance of the system is  $G = 2 G_0$ . In the non-ideal case, a SWNT with perfect contacts, assume the transmission coefficients of both the conducting channels are  $T_I (0 \leq T_I \leq 1)$ , then  $G = 2T_I G_0$ .

For an ideal case, a ballistic nanotube with ideal contacts, the transmission coefficient for all N available subbands equals to unity. According to the Landauer equation (Eq. (2.6)), the conductance of the system is  $G = N G_0$ . In the non-ideal case, assume the transmission coefficients of all the conducting bands are  $T_I (0 \leq T_I \leq 1)$ , then  $G = N T_I G_0$ .

Figure 2.12 shows the conductance as a function of bias voltage for the tube (100, 100) according to the Landauer equation, assuming a transmission coefficient  $T=1$  (calculated by de Heer (Berger, 2002)).

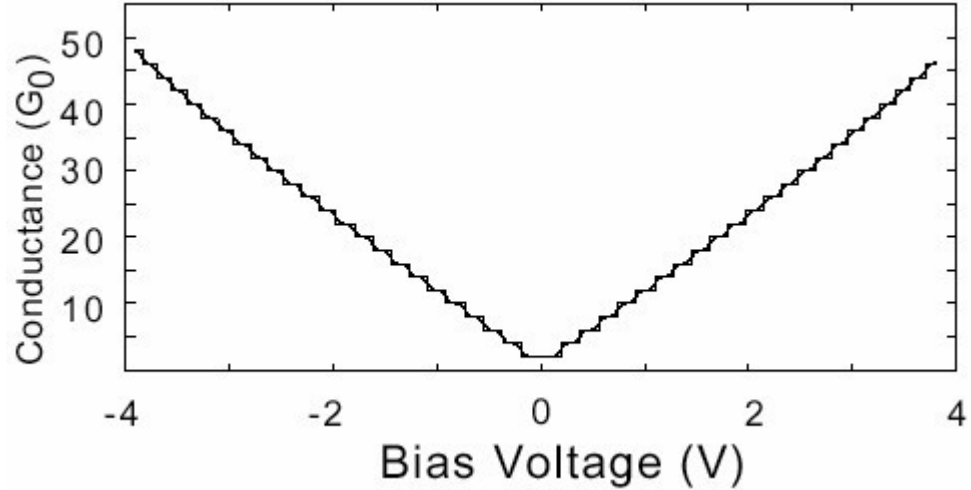


Figure 2.12: The predicted conductance  $G$  versus bias voltage for the nanotube (100, 100) from the Landauer equation, assuming unity transmission for all channels, which states that when the bias voltage increases above the bottom of a subband, then that subband contributes  $G_0$  to the conduction, which gives  $G(V)$  its staircase appearance (Berger, 2002). Due to the symmetry above and below  $E_F$ , contributions from subbands below  $E_F$  and above  $E_F$  coincide so that the conductance increases in steps of  $2 G_0$ . Thermal smearing at  $T = 300$  K blunt the steps to provide an essentially perfectly linear rise in the conductivity with increasing bias voltage. The linear increase in the DOS is common to all metallic nanotubes independent of helicity up to about  $V_{bias} = 6$  V (White, 1998; Charlier, 1998).

The intrinsic resistance of the nanotube (due to scattering in the tube) is related to the transmission probability using the Landauer formula (Datta, 1995; Bachtold, 2000; Bockrath, 2001). Assuming there are 2 conducting channels, according to Eq. (2.7),

$$R_{intr} = (1/2 G_0) \cdot (1 - T_l) / T_l \quad (2.8)$$

Note that the transmission coefficient  $T_l$  is for electrons along the length of the tube since the contacts are assumed perfect. Following Bachtold *et al.* (Bachtold, 2000), ballistic transport is unambiguously demonstrated when  $T > 1/2$ , because then the majority of electrons traverse the nanotube without scattering.

In 1999 when I started my thesis, the experiment by de Heer and colleague were the only ones found that MWNTs were ballistic conductors. They used arc-produced unprocessed MWNTs.

While recently it appears to have been reached that SWNTs are ballistic conductors under favorable conditions (Liang, 2001; Kong, 2001; Javey, 2003). They observed ballistic conduction at 10 K occurs in untreated SWNTs from quantum oscillations in a Fabry-Perrot experiment. Two-probe resistances at room temperature as low as 7 k $\Omega$  have been measured suggesting low scattering at room temperature as well.

There is still some controversy surrounding MWNTs, some concluding that they are diffusive conductors (Langer, 1996; Dai, 1996; Schonberger, 1999; Collins, 2001), and others that they are ballistic conductors (Frank, 1998; Poncharal, 2002; Berger, 2003; Urbina, 2003).

Langer, *et al.* conclude that MWNTs have 2D diffusive transport governed by electronic interference down to a temperature of 20 mK (Langer, 1996). They use arc-discharge produced MWNTs, which are dispersed on an oxidized Si wafer covered with an array of large square gold pads. Then they deposited a gold film on the top of the gold pads to make electrical contacts with the nanotubes by STM lithography (Langer, 1996).

Measurements by Schonberger *et al.* on individual MWNTs concluded that the transport in MWNTs is one dimensional, diffusive at room temperature and quasi-ballistic at low temperatures (Schonberger, 1999). The nanotubes were purified and ultrasonically dispersed in liquid using surfactants as described by Bonard *et al.* (Bonard, 1997).

Bachtold *et al.* used lithographically contacted nanotubes and found that the room temperature resistance of MWNT is  $\rho = 10 \text{ k}\Omega/\mu\text{m}$ , while  $\rho < 1.5 \text{ k}\Omega/\mu\text{m}$  was found for the SWNT bundle. They concluded that SWNTs are ballistic conductors and MWNTs are diffusive conductors (Bachtold, 2000).

Collins and Avouris *et al.* find complex conduction behavior for lithographically contacted MWNTs (Collins, 2001). The nanotubes were applied to prepatterned Au electrodes, after dispersing them in dichloroethane, centrifugation and a thermal treatment. The transport properties were interpreted in terms of the interplay of the contributions from multiple semiconducting and metallic layers where up to 8 layers contribute to the transport in the high current (non-linear transport) regime (Collins, 2001).

Urbina *et al.* prepared solutions of multiwalled carbon nanotubes in a mixture of polychlorinated biphenyls. Transport measurements were performed using a scanning-tunneling probe on a sample prepared by spin coating the solution on gold substrates. Conductance steps were clearly seen. A histogram of a high number of traces shows maximum peaks at integer values of the conductance quantum  $G_0 = 2e^2/h$ , demonstrating ballistic transport at room temperature along the carbon nanotube over distances longer than  $1.4 \mu\text{m}$ . (Urbina, 2003).

Transport in layers below the outmost layer in MWNTs was shown to be phase coherent over distances of order  $1\mu\text{m}$  (Buitelaar, 2003; Buitelaar, 2002).

The reasons for these discrepancies between the various nanotube measurements are clarified in this thesis.

## CHAPTER 3

### EXPERIMENT CONFIGURATION AND PROCEDURES

First I will introduce the methods that were used to prepare clean MWNT samples. Then the experimental configurations and procedures of the experiments using scanning probe microscope (SPM) and transmission electron microscope (TEM) are explained in detail, including conductance measurements and current-voltage measurement.

#### 3.1 Sample Preparation

The MWNTs used in this thesis were produced using the pure carbon arc discharge method. The samples were prepared at the EPFL (École Polytechnique Fédérale de Lausanne, Swiss). Electric power is supplied with a full-wave rectified AC power supply (80 A, 20 V). The 7 mm diameter graphite anode and the 50 mm diameter graphite cathode are placed in a 500 Torr Helium atmosphere with an electrode separation of 1 mm (see Figure 1.7a). The MWNTs are found on the cathode in a soft, sooty deposit inside a hard carbonaceous shell. The soot is composed of loosely packed fibers that are approximately aligned with the direction of the current. The fibers are typically 1 mm long and 0.1 mm in diameter. The fibers consist of compacted MWNTs (80%) and other graphitic objects including amorphous flakes and polyhedral particles that cover the nanotubes. These MWNTs were fully characterized by HRTEM by D. Ugarte (at EPFL). The tubes protruding from the fibers are typically 1-10  $\mu\text{m}$  long and 5 - 25 nm in diameter (in Figure 3.1 and Figure 3.2). The straightness of the tube indicates its high purity (defects are known to bend the tubes), as verified in the HRTEM.

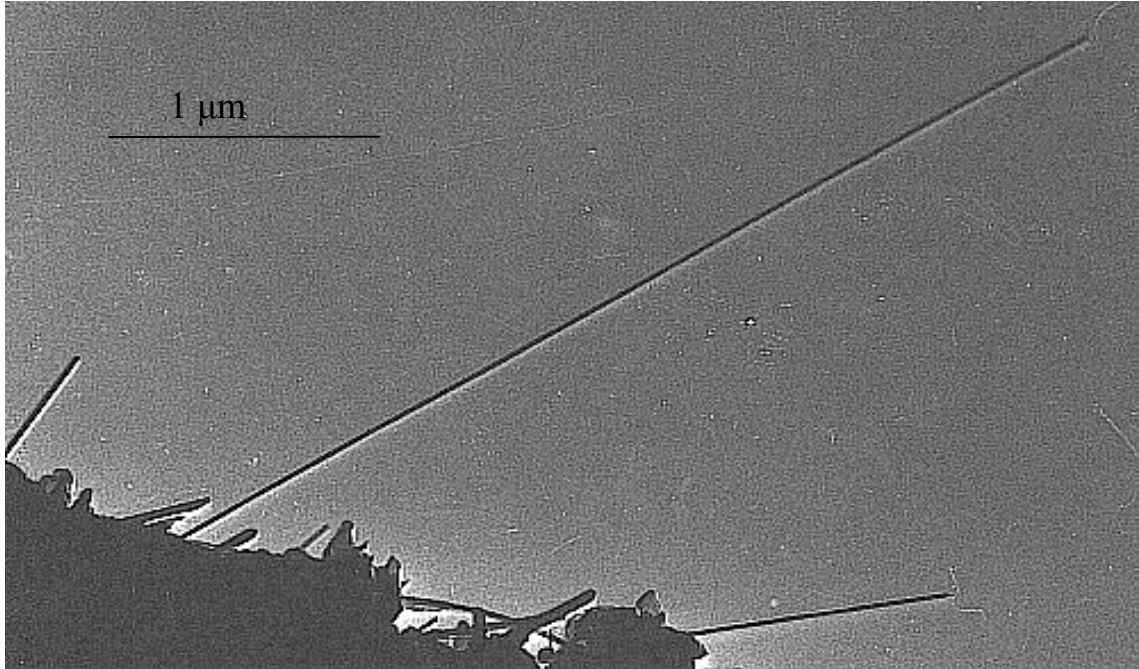


Figure 3.1: TEM image of clean carbon nanotubes protruding from a fiber (on the lower-left corner). The fiber has the length of 1 mm and a diameter of 50 μm. The longest tube shown on this picture is 3.7 μm length and about 25 nm diameter (de Heer, unpublished).

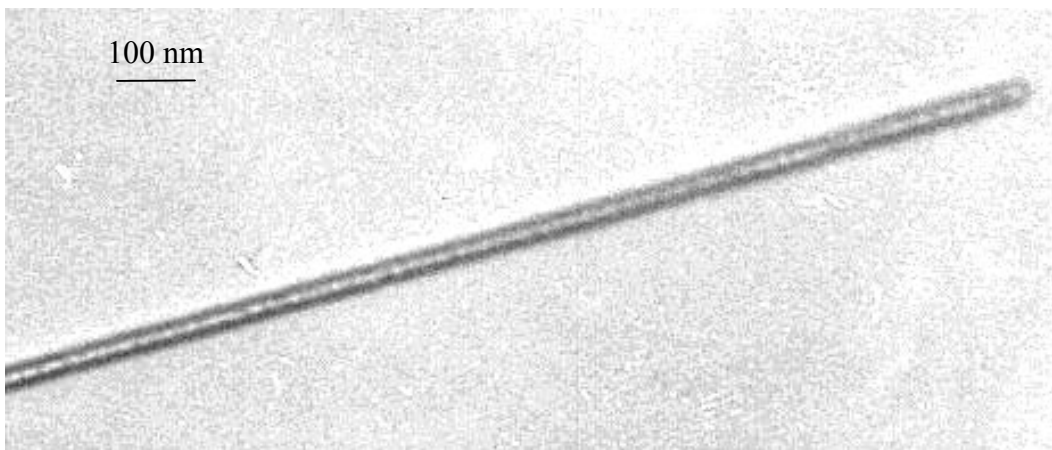


Figure 3.2: TEM image of the tip of the longest tube shown in Figure 3.1. The straightness of the tube indicates its high purity (defects are known to bend the tubes) (de Heer, unpublished).

For the transport measurements, an intact and non-treated fiber is carefully selected with uniform narrow width, and separated (mechanically broken using tweezers) from the deposit under an optical microscope. Frequently the nanotubes on the surface of the fibers are coated with amorphous carbon balls (shown in Figure 3.3). For this reason, the tips of the fibers are carefully removed to expose the inside nanotubes without balls. Next the cut fiber is attached to a conducting wire using silver epoxy (Epoxy Technology Eop-Tek417). It takes two days to cure the epoxy at room temperature, or takes two hours if it is heated up to 80°C. Since microscopic images show that nanotubes can still be covered with graphite particles, the fiber is usually repeatedly dipped into clean mercury hundreds to thousands of times. We have discovered that this process removes the graphite particles and cleans up the protruding nanotubes, and ensures that only those nanotubes that are well anchored remain in place. The dipping process causes a dark deposit to appear on the metal surface, which can be observed with the SPM alignment microscope. This deposit comes from carbon particles from the nanotubes (as verified in in-situ TEM experiments). And this dipping process also separates the tubes. The cleaned fiber sample is ready for the use of TEM and in-Air SPM experiments.

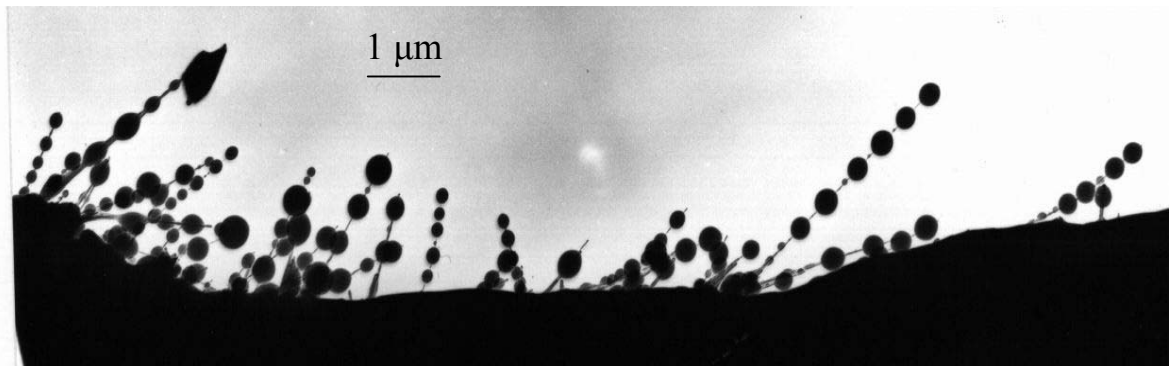


Figure 3.3: TEM image shows that the carbon nanotubes protruding from the fiber (on the bottom) are covered with carbon balls (de Heer, unpublished).

### 3.2 Experiment using the Scanning Probe Microscope

A scanning probe microscope (SPM) (Park Scientific Instruments Autoprobe CP) is used with the software Proscan1.7. This microscope's cartridge holder is modified to hold the conducting wire on which the clean fiber sample mounts. The schematic sketch of the experimental configuration is shown in Figure 3.4. The z-piezo under the liquid metal container can move the container up and down. When the z-piezo moves the container up, the sample fiber is relatively moved lower toward the metal liquid surface. This microscope is covered by an Al-cylinder put on a floating-table to reduce noise and vibration, and also to provide electromagnetic shielding.

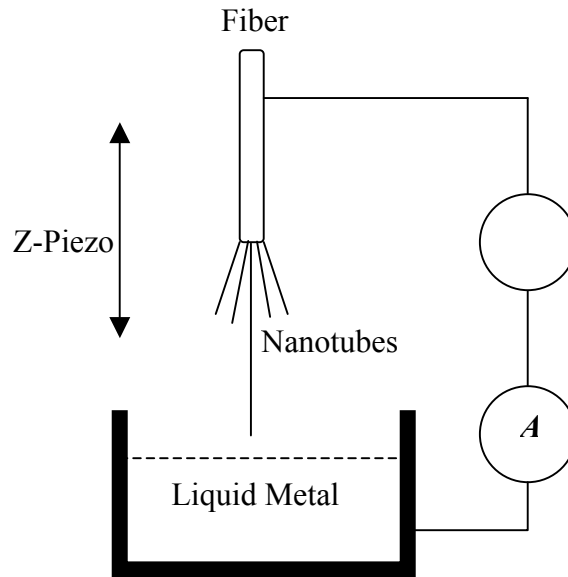


Figure 3.4: Schematic diagram of the experimental configuration. The nanotube contact is lowered under SPM control to a liquid metal surface. After contact is established, the current  $I$  is measured as the fiber is moved into the liquid metal. Since the length of the nanotube left outside of the mercury decreases when the fiber is moved into the liquid metal, the conductance can be determined as a function of the length of the nanotube.

Two-probe measurements are used in this experiment to measure the conductance of a nanotube as the tube is lowered into liquid metal. The fiber is lowered under SPM control to a liquid metal surface. When the fiber sample is lowered toward the liquid metal surface, the longest nanotube contacts the liquid metal first. This makes it possible to measure the conductance of a single nanotube as the tube is lowered into mercury.

After contact is established, the current  $I$  is measured as the fiber is moved into the liquid metal. Since the length of the nanotube left outside of the liquid metal decreases when the tube is moved into the liquid metal, the conductance can be determined as a function of the length between the tip nanotube and the liquid metal surface. Mercury is used typically as the liquid metal. Gallium and various low-melting point metals have also been used. Since gallium oxidizes very quickly in air, the experiments with gallium are performed under high purity silicon oil.

A series resistor is added to the circuit to measure the current. The block diagram showing the connections between the equipments is shown in Figure 3.5.

A voltage of 100 mV usually is applied to the tip. The current, passing through the tube, is measured using a fast transient digital oscilloscope (LeCroy 574AM). The position of the nanotube with respect to the liquid metal surface is also recorded. The process of moving a tube down toward the liquid metal, making a contact with the liquid metal, and then moving the tube up back to the original place is called one cycle. The corresponding curve showing the change of the conductance of the tube is called one trace. In a more recent version, a data acquisition (DAQ) device is used instead of the oscilloscope. This DAQ device includes a National Instruments BNC-2110 interface, which has BNC connectors for analog output/input with a shielded enclosure. A LabView

program was specially designed to control the experiment, and to collect and record the data.

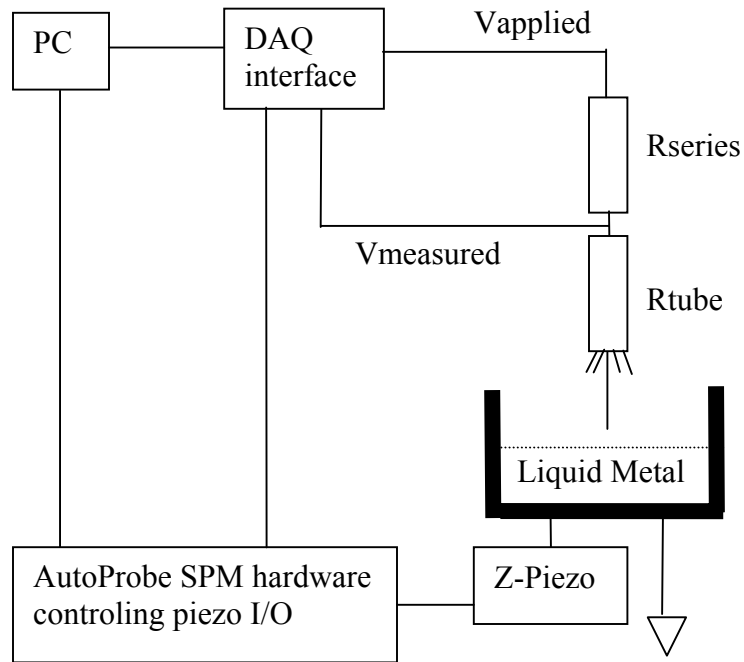


Figure 3.5: Block diagram of the in-air SPM experimental configuration. The z-piezo under the liquid metal container can move the container up and down. When the z-piezo moves the container up, the sample fiber is relatively lowered toward the metal liquid surface.  $V_{applied}$  is the applied voltage on the tube and the resistor in series with the tube.  $V_{measured}$  is the measured voltage drop on the tube and is used to calculate the current passing through the nanotube.

The experiment is repeated at a typical rate of 1-10 Hz for several hundreds to thousand of cycles where the tip is raised and lowered in the range 1-10  $\mu\text{m}$ . Up to 100,000 data points per single trace are collected. Data are automatically collected in sequence of 50 or 100 traces.

As mercury in the container oxidizes in air, white oxide layers build up on the Hg surface after some time, which may interfere with the contact to the nanotube. It is required to clean the mercury surface every 30 minutes to few hours by scraping the surface of the mercury to remove this oxide. The copper container (in contact with mercury) reacts with Hg to form a white compound, which pollutes Hg. To avoid such contamination, the copper container has to be cleaned each day.

In another series of experiments, we have measured the current-voltage characteristics measurements, which are made by applying voltage in swept on the nanotube and the series resistor when the tube is in contact with the mercury, and measuring the current passing through the tube. This experiment can be done either continuously by using a fast high-resolution digitizer, or point by point by using the Data Acquisition Interface Board. The latter one uses a LabView program and can sweep the voltage between 0 and +10 V, or between 0 and -10 V, which gives the opportunity to investigate the properties of nanotubes at different voltage polarity. We usually used the sweeping rate at 500 points per cycle.

For comparison we have also measured the current-voltage characteristics of a Hg droplet touching an HOPG (Highly Oriented Pyrolytic Graphite) surface. We attached a

small Hg droplet to a fine wire, which was manipulated in air using a scanning probe microscope (SPM). Hence the droplet was brought into contact with a freshly cleaved Highly Oriented Pyrolytic Graphite (HOPG) surface, and the conductance was measured as a function of the applied voltage, as for the nanotube experiments above. The contact area of the droplet to the graphite surface can be adjusted using the SPM positioning mechanism: at first contact, the conductance is small, when the droplet is lowered further, then the conductance increases. Even though the contact area is not calibrated, these experiments can provide important insights into the properties of very small metal contacts to graphitic systems. We concentrated on the conductance as a function of voltage.

### 3.3 Experiment using TEM

The TEM experiments are primarily performed to characterize the condition of the fibers and to verify the processes observed in the in-air experiments. So we can observe the phenomena of nanotubes getting into contact with mercury at a microscopic scale.

A JEOL 100CX II scanning transmission electron microscope (TEM) is used. It has an accelerating voltage 20-120 kV. A beam of electrons is accelerated and aimed at a sample under study within a vacuum chamber. After the electron beam passes through the sample, it is focused and projected onto either a screen or photographic film to provide an image of the structure. Its point resolution is 0.7 nm. Its stage has  $xy$ -translation.

Since we want to observe the contact point where the longest nanotube protruding from the sample fiber gets into contact with mercury, and also we need to apply a voltage to the sample fiber, the TEM sample holder was specially designed to hold a fiber sample

inside the microscope shown in Figure 3.6. In this device, the clean fiber mounted on the conducting wire is on the left. A copper wire, facing the fiber, wetted with a mercury droplet is on the right.

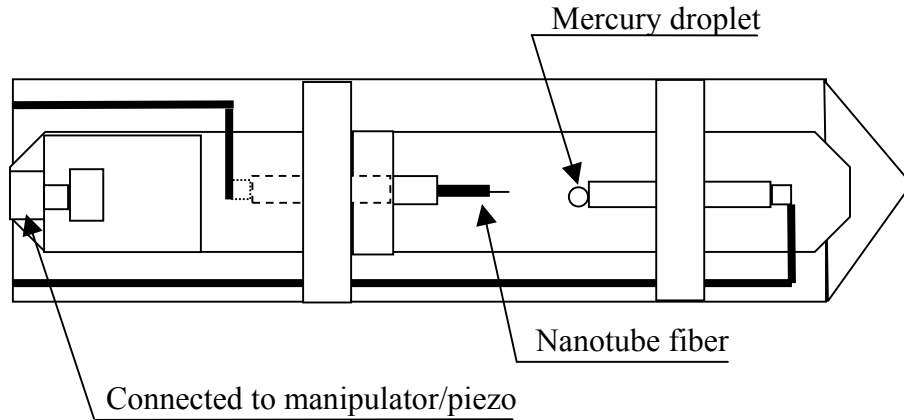


Figure 3.6: Sketch of TEM sample holder specially designed for in-situ TEM nanotube experiments (length is 35 mm, width 7 mm). The fiber sample mounted on a conducting wire (on the left) can be manually moved toward the mercury droplet (on the right) using a manipulator. The piezo actuator is used for the final approach. A voltage is applied to the conducting wire connecting with the fiber, and the copper wire wetted with a mercury droplet is grounded. Telfon is used as electrical isolation.

The fiber is brought into contact with the mercury droplet under TEM observation. The fiber can be manually moved toward the mercury droplet using the manipulator from outside the vacuum chamber. This manipulator is designed to get a coarse control in translating in x- and y-direction, tilting in z-direction, and also rotating the sample. A piezoelectric stack Thorlabs NECAE0505D16 is used for fine adjustment in z-direction. The nanotubes protruding from the sample fiber are then brought into contact with the mercury droplet, and the conductance is measured.

In order to have the mercury drop stay at the tip of copper rod, we first pull the tip of the copper rod to a rounded shape in which the tip provides more contact area with the mercury droplet. Second, the tip is dipped into clean mercury for an hour before each experiment in order to wet the tip with clean mercury. Since the used copper rods get wetted by the mercury and become contaminated after used in TEM experiments, they are not recycled. New copper rods have to be prepared for each TEM experiment.

The piezoelectric stack consists of many piezoelectric ceramic layers that are assembled in series mechanically and in parallel electrically. The displacement at Maximum Drive Voltage (150 V) is  $17.4 \pm 2.0 \mu\text{m}$ . The voltage range (0 ~ 150 V) is used to get maximum z-displacement. A KEPCO bipolar operational power supply / amplifier (model BOP 1000M) is used as the power supply to provide the voltage (0 ~ 150 V) to the piezo.

The sketch of electric connections inside the specially designed sample holder is also shown in Figure 3.6. A voltage is applied to the conducting wire connecting with the fiber, and the copper wire wetted with a mercury droplet is grounded. The sample holder is grounded to remove the electron accumulated on the sample holder. The block diagram of the experimental configuration is shown in Figure 3.7. Since the DAQ interface board has a I/O limit of 10 V, but the piezo requires a voltage up to 150 V and our KEPCO power supply / amplifier has a fixed voltage amplification ( $\times 600$ ). Therefore, two voltage-dividers are added in the I/O as shown in Figure 3.7.

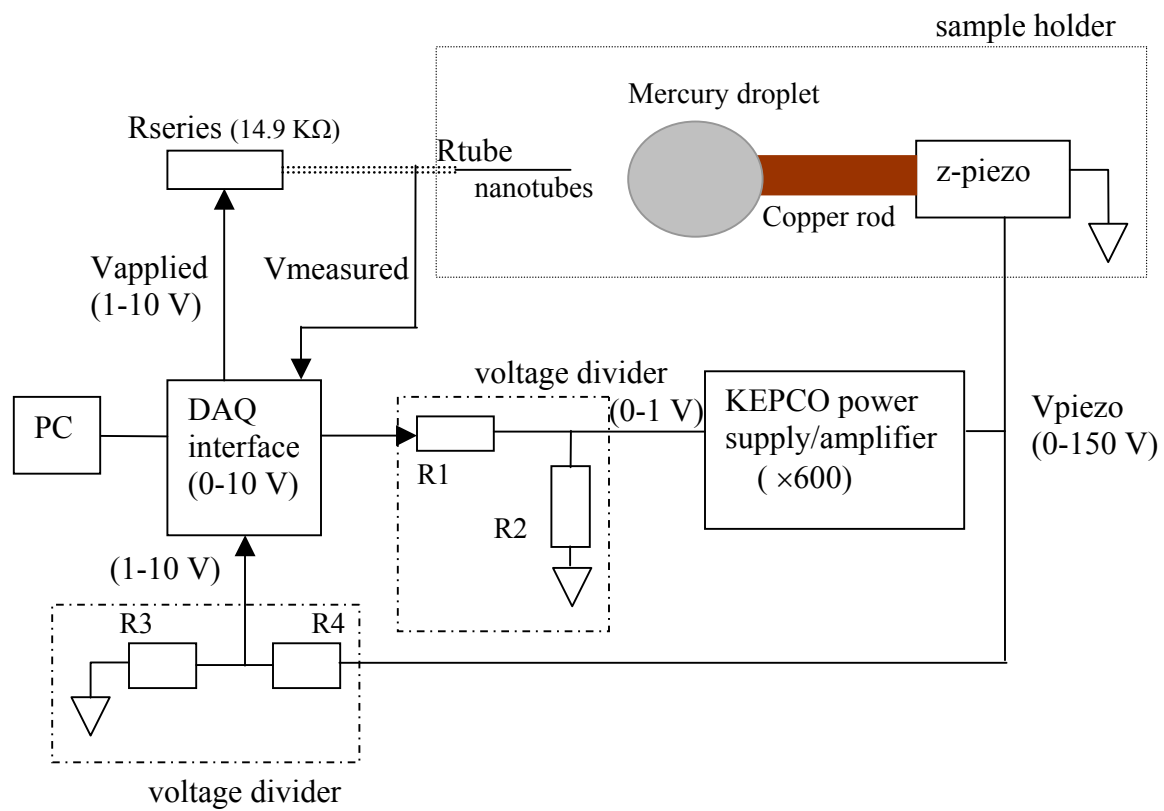


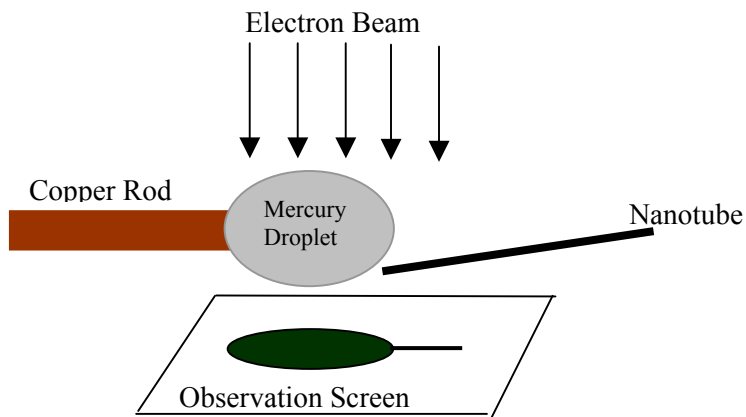
Figure 3.7: Block diagram of TEM experimental configuration. Two voltage dividers are used to convert the I/O piezo voltages (up to 150 V) to a value in the limit of the DAQ interface ( $<10$  V).

Experimental procedures are as follows. First, we load a previously Hg dipped fiber sample mounted on a conducting wire into the sample holder. Next, a small mercury drop is separated from a large drop in a clean plate and suspended to the copper rod tip in the sample stage. Then the sample holder is introduced into the TEM vacuum chamber. It takes a few minutes to evacuate the chamber. Sometimes the microscopic image shows that there is no long and/or clean tube in view on the fiber. In that case, we take the sample holder out and cut the tip of the fiber again to expose fresh tubes.

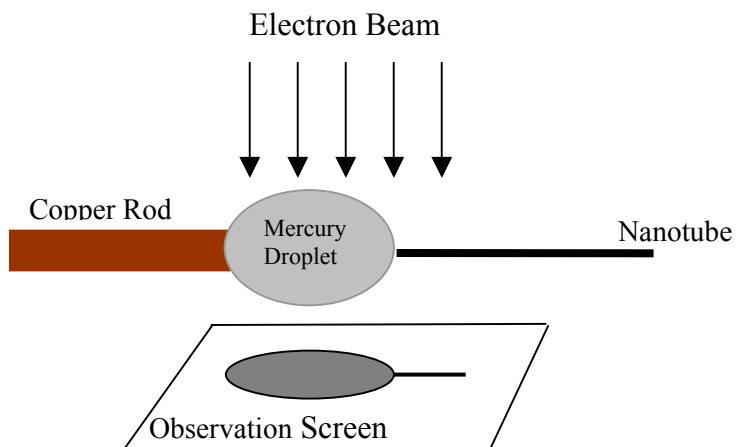
In a typical day, nanotubes on several fibers are measured. Between the measurements of different fibers, the mercury droplet has to be cleaned to remove the contamination. Since it is very difficult to align the electron beam at the TEM with the fiber-metal contact in order to observe the contact point shown in Figure 3.8, only a limited number of measurements produce useful results. Since the tubes are fully suspended and vibrate, this reduces the resolution of the observation.

This TEM experiment is complex requiring three persons to operate TEM, to run the computer, to take notes and pictures.

About fifty nanotubes have been measured in TEM experiments. More than 200 nanotubes have been measured in SPM experiments.



(a) The contact point of the nanotube with the mercury droplet is masked.



(b) The contact point of the nanotube with the mercury droplet is observable.

Figure 3.8: Schematic sketch showing the relative position of a nanotube and the mercury droplet (a) in which the contact point is under the mercury droplet and can't be seen using microscope. (b) in which the contact point can be observed using microscope.

## CHAPTER 4

### OBSERVATIONS AND RESULTS

SPM and TEM experiments are conducted to measure a MWNT's electrical conductance as a function of its length and of applied voltage at room temperature. The observations and results will be described and reported starting by the low-bias  $G(L)$  experiments, then high-bias current-voltage experiments and finally insulating tubes.

#### 4.1 Low-Bias Experiments

Experiments using low-bias voltages ( $\sim 10$  mV) have been conducted to measure conductance of MWNTs both in air and in vacuum. These experiments have been performed on clean nanotubes and also on surfactant-coated nanotubes.

##### 4.1.1 Clean Nanotubes

Figure 4.1 shows a TEM image of a MWNT fiber tip opposing a mercury surface and a conductance trace of the dipping process. Many nanotubes protrude from the fiber that is composed of densely packed carbon nanotubes and other graphitic nanostructures shown in Figure 4.1(a). The transport measurements are made by measuring the conductance as a function of the position of the tube while lowering its tip into the liquid metal. One full cycle conductance trace versus position, defined as the fiber is first lowered to the Hg and subsequently withdrawn, is shown in Figure 4.1(b). The upper axis in the Figure 4.1(b) shows the position of the tip relative to the mercury surface. The negative sign of the depth indicates that the tip is lowered into the mercury, and the positive sign indicates that the tip is withdrawn from the mercury. Thus the depth at zero is the turning point.

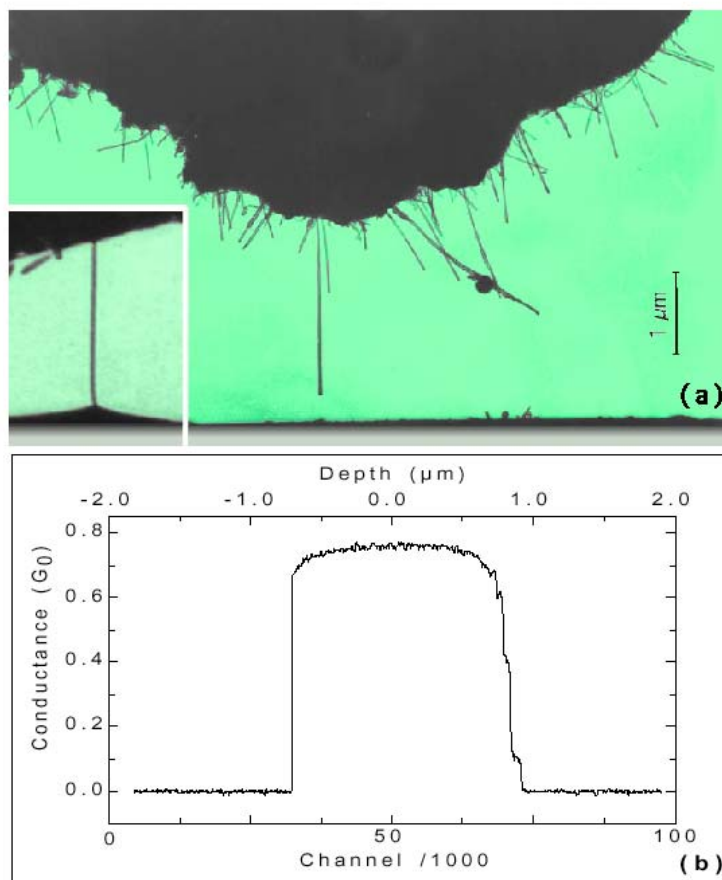


Figure 4.1: TEM image of a MWNT fiber tip opposing a mercury surface and the dipping process. (a) The nanotubes protrude from the fiber that is composed of densely packed carbon nanotubes and other graphitic nanostructures. The transport measurements are made by lowering the tip into the liquid metal and measuring the conductance as a function of the position. Inset: Example of cone shaped meniscus attached to the tip of the nanotube which occurs when the nanotube is pulled out of the (non-wetting) liquid just before contact is broken. (b) A full cycle conductance trace (conductance  $G=I/V$  versus position) where the fiber is first lowered to the Hg and subsequently withdrawn (see upper axis). Note the asymmetry with respect to the turning point due to the non-wetting adhesive effects.

Electron microscopy studies reveal that as the nanotube is pulled away from the surface, just prior to breaking contact, a cone shaped meniscus is drawn from the mercury shown in Figure 4.1(a) inset. It causes an offset of the position of the conductance step coming out the mercury compared with the one going into shown in Figure 4.1(b). This effect is due to non-adhesive wetting, which can be demonstrated by using a simple experiment with a glass rod touching a mercury surface. Due to this effect, only conductance traces of tubes going into the Hg are analyzed and not the ones as the tubes are withdrawn.

Nanotube wetting has been extensively studied. Dujarding *et al.* find that there is an upper limit for the surface tension of the liquid ( $= 180 \text{ mN/m}$ ) beyond which wetting of MWNTs is no longer favorable. The surface tension of mercury ( $490 \text{ mN/m}$ ) and gallium ( $710 \text{ mN/m}$ ) are too high for wetting, and neither gallium nor mercury wet nanotubes (Dujardin, 1998). The earlier experiments show that Hg does not fill opened nanotubes by capillarity (Ugarte, 1996). Moreover, if nanotubes were wetted by mercury, then the highly porous nanotube fiber would become soaked with mercury, which does not occur. Finally electron microscopy of MWNTs in contact with Hg shows no evidence for wetting. Since wetting is required for the formation of a liquid film on the nanotubes, we can confidently assert that no such film exists on the tubes.

Figure 4.1(b) shows the conductance  $G(x) = I/V$  measured as a function of distance  $x$  that the fiber is lowered into mercury. Contact of the nanotube with the mercury surface results in a jump of conductance followed by a flat plateau with some rounding at the beginning of the step in the conductance. Figure 4.2 also shows the conductance  $G(x)$  measured as a function of distance  $x$ . Figure 4.2(a-c) shows the evolution of the conductance steps with cycling time. The successive steps in a trace result from several tubes that

successively come into contact with the mercury. Initially the steps in  $G(x)$  are poorly defined shown in Figure 4.2(a-b), and a dark deposit is found to appear on the mercury surface, which can be observed with the SPM alignment optical microscope. This deposit comes from material from the fiber, which was verified in TEM experiments. The fiber is then displaced to a fresh area of the mercury surface. A stable pattern of steps is established after some time shown in Figure 4.2(c), which is typically reproduced for several hundred cycles. While the plateau lengths may vary somewhat from one cycle to the next, the values of the conductances at the steps are stable within about 5%, which is also observed in the earlier work (Frank, 1998).

Occasionally the experiment fails to produce conductance steps and the conductance jumps immediately from zero to full contact, corresponding to the resistance values decreasing from infinite to (10-100  $\Omega$ ). TEM examination of some of these tips showed that there were no tubes extending from the fiber.

Well-defined and reproducible conductance steps usually evolve only after repeated dipping into the liquid metal. Initially the steps are poorly defined with large slopes. The slope of the first step in Figure 4.2(a) corresponds to  $-dR/dx = 36 \text{ k}\Omega/\mu\text{m}$ ; the slope of the step in Figure 4.2(b) corresponds to  $-dR/dx = 4 \text{ k}\Omega/\mu\text{m}$ . The ultimate conductance plateaus are very flat with some rounding at the beginning of steps. The typical ultimate conductance values of the first plateau ranges from  $G_{pl} = 0.5 \sim 1 G_0$ . Sometimes even lower values are seen, however initial plateaus with  $G_{pl}$  substantially greater than  $1 G_0$  are not observed. A typical conductance trace consists of several upward conductance steps when the fiber is pushed down into the liquid metal. The sequence is reversed when the fiber is retracted from the metal. Typically  $G_{pl}$  varies slightly from trace to trace by a few percent.

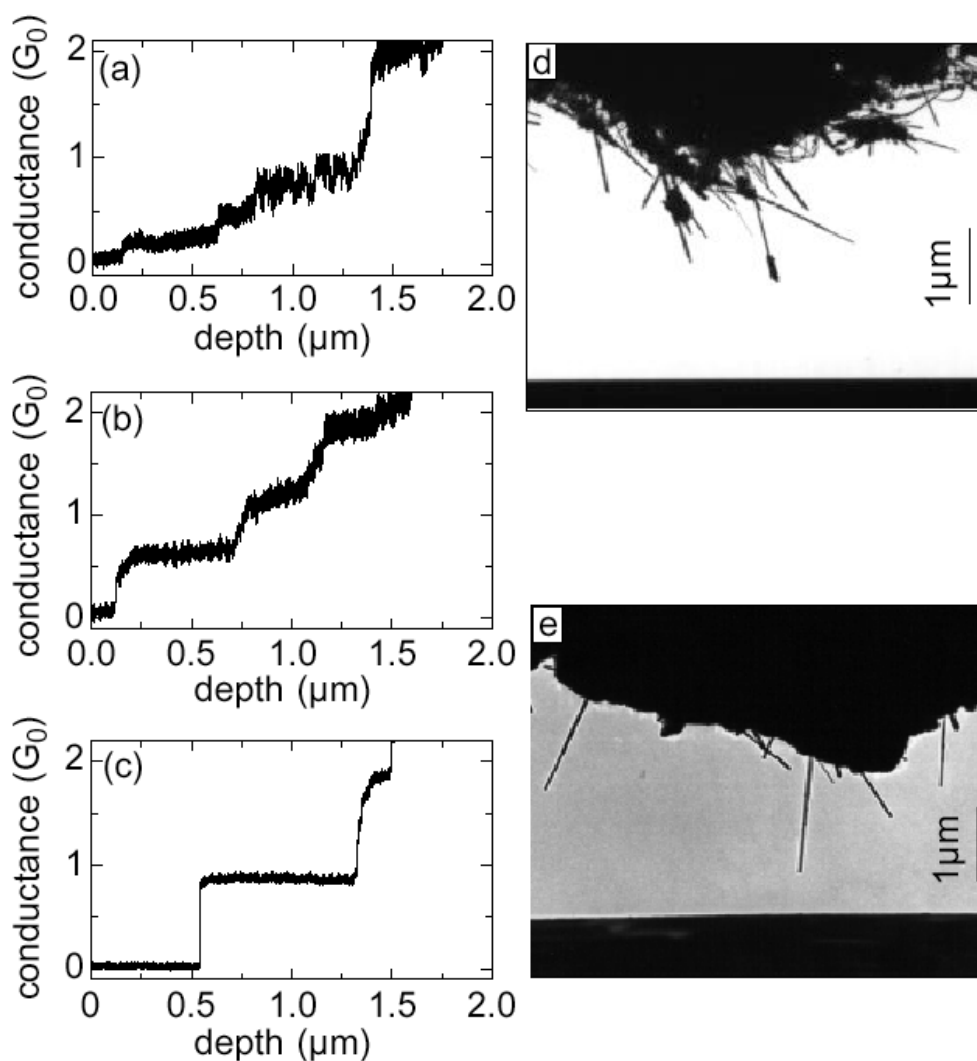


Figure 4.2: Cleaning of nanotubes and evolution of nanotube fiber properties by repeated dipping in Hg. (a) Conduction trace of the virgin fiber: steps are barely discernable; (b) Steps develop after a few hundred cycles but they still exhibit relatively large slopes and jumps. (c) After several thousand cycles, the conductance steps are well developed and the pattern of the conductance steps is stable. The first step evolves from the shoulder seen in (a) (step:  $0.2 G_0$ , slope:  $36 \text{ k}\Omega/\mu\text{m}$ ) to a rounded step in (b) (step:  $0.62 G_0$ , slope:  $4 \text{ k}\Omega/\mu\text{m}$ ), to the well defined step with a flat plateau in (c). The second conductance step is due to another tube and evolves analogously. (d) TEM micrograph of a virgin fiber tip opposing Hg surface. Note the contaminating graphitic particles and the loose structure of the tip. (e) TEM micrograph of a fiber tip that has previously been repeatedly dipped in Hg, and the nanotubes are straight and free of particles and the fiber is compacted (Berger, 2002).

Poorly defined steps correlate with the degree of contamination on the nanotubes. Nanotubes that have not been in contact with Hg tend to be covered with graphitic particles as can be seen in the electron microscopy images shown in Figure 4.2(d). The dipping process initially causes some changes in the morphology of the nanotubes protruding from the fiber. In particular, some tubes move from their original positions. Occasionally large fragments are transferred from the fiber to the liquid metal as observed in the TEM. The evolution of the conductance steps and the TEM images shown in Figure 4.2(a-e) suggest that the dipping process not only cleans the graphite particles from the tubes but also insures that only those nanotubes that are well anchored remain in place. The former process causes the plateaus to become flatter and less noisy whereas the latter process raises the plateau value, when better contact of the nanotube with the fiber is established.

We have observed that the nanotubes that protrude from specific fibers often produced flat conductance plateaus with significantly lower conductance values (about 0.3-0.5  $G_0$ ). These might be attributed to poor contacts with the fiber, since these plateaus are prone to jump to larger values and ultimately to stabilize.

#### 4.1.2 Surfactant-coated Nanotubes

The effect of surfactants and solvents on nanotubes has been investigated as shown in Figure 4.3. Nanotube fibers were dipped in an aqueous solution of sodium-dodecyl-sulfate (SDS) and dried. SDS is a surfactant that is often used to suspend nanotubes (Bonard, 1997). Prior to this treatment these fibers produced the typical flat plateau structures. Figure 4.3(a-b) shows a typical conductance trace (one of 100

recorded in this series). The steps of the surfactant-coated tubes have reduced conductance values and the resistance decreases linearly with increasing  $x$  shown in Figure 4.3(b) indicating a resistive nanotube. Surfactants affect the conductance properties of the nanotubes. Figure 4.3(c-d) also shows the  $G(x)$  and  $R(x)$  for a clean nanotube of similar length with a low plateau resistance for comparison with the surfactant-coated tubes (detailed analysis in chapter 5).

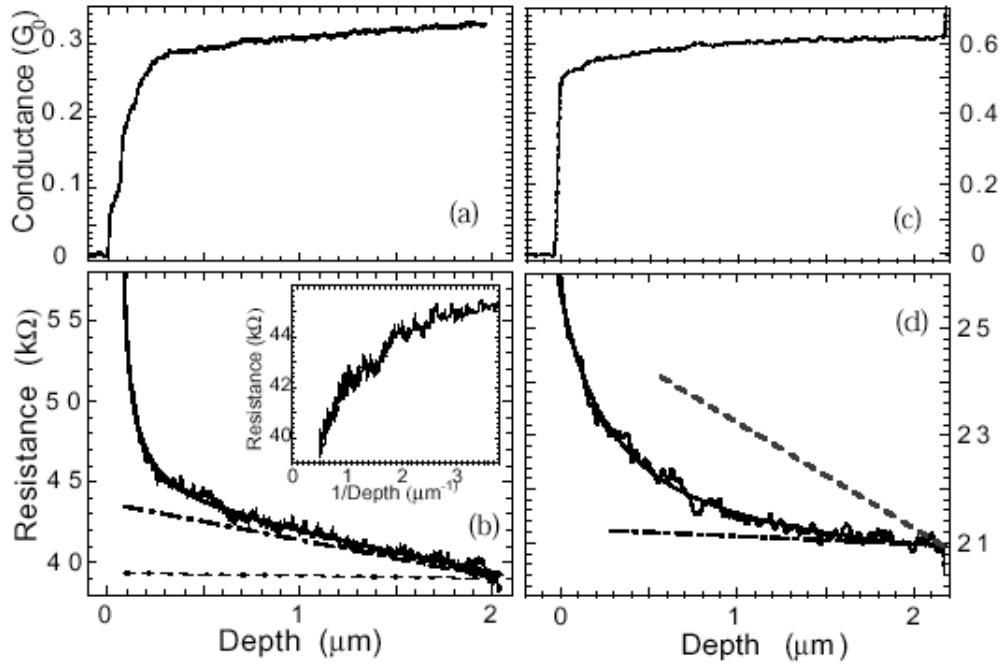


Figure. 4.3: Effect of a surfactant on  $G(x)$ . (a) For a sodium-dodecyl-sulfate-coated nanotube, its conductance  $G(x)$  continues to increase with increasing  $x$ , in contrast to clean tubes. (b) The resistance  $R(x) = 1/G(x)$ . The solid line is the fitting line to the semi-classical model (see chapter 5 (Eq. (5.3))). Note that  $R(x)$  asymptotically approaches the slope  $-dR/dx = 2.3 \text{ k}\Omega/\mu\text{m}$  (dot-dashed line), from which about  $0.1 \text{ k}\Omega/\mu\text{m}$  is due to the metal contact resistance of  $500 \text{ }\Omega\mu\text{m}$ . The  $-dR/dx$  slope is more than an order of magnitude greater than the slope typically found for clean tubes of similar length i.e.  $-dR/dx = 0.2 \text{ k}\Omega/\mu\text{m}$  (dashed line). Inset: resistance  $R$  as a function of  $1/x$ , showing that contrary to a clean tube the shape of the conductance trace is not only determined by the contact conductance. (c-d) Example of a clean nanotube of similar length ( $2 \mu\text{m}$ ) used for comparison (see chapter 5) (c)  $G(x)$  with a low plateau conductance  $G_{pl} = 0.64 G_0$  (d)  $R(x)$  asymptotically approaches the plateau resistance  $R_{pl} = 20.3 \text{ k}\Omega$ ; from the slope at  $x = 2 \mu\text{m}$ ,  $-dR/dx = 260 \text{ }\Omega/\mu\text{m}$  (dot-dashed line) which is an upper limit to the resistance of the tube. Also shown is the slope  $-dR/dx = 2.3 \text{ k}\Omega/\mu\text{m}$  (dashed line) corresponding to the surfactant coated tube in (b).

## 4.2 High-Bias Experiments

High-bias experiments are used to measure conductance of nanotubes as a function of applied voltage at room temperature, either in air or in vacuum. These experiments have been performed on clean nanotubes and also on surfactant-coated nanotubes.

### 4.2.1 Clean Nanotubes

Conductance versus voltage measurements  $G(V)$  of clean nanotubes show typically symmetric patterns as seen in Figure 4.4. The conductance curve is constant at low-bias up to about 100 mV, and then it rises with a constant slope, typically  $dG/dV = 0.3\sim 0.5 G_0/V$ . The slope is constant up to  $V = 4$  V. The curves are symmetric about the  $V = 0$  axis with a slight offset (typically less than 10 mV). Saturation of the current (or a decrease in conductance) with increasing voltage is not observed in this case for the voltage up to  $|V| = 4$  V where  $I = 615 \mu\text{A}$  shown in Figure 4.4(a). Measurements made in the electron microscope also show the linear conductance increase and confirm the in-air results. For example, a 15 nm diameter, 0.5  $\mu\text{m}$  long nanotube measured *in-situ*, shows a linear rise of about  $0.5 G_0/V$  for  $V > 0.2$  V shown in the inset of Figure 4.4(a).

Figure 4.4(b) shows  $G(V)$  measurements of a nanotube submerged to various depths in the liquid metal, which do not show significant changes from one depth to the next. The  $G(V)$  curve appears to be only weakly dependent on  $x$ .

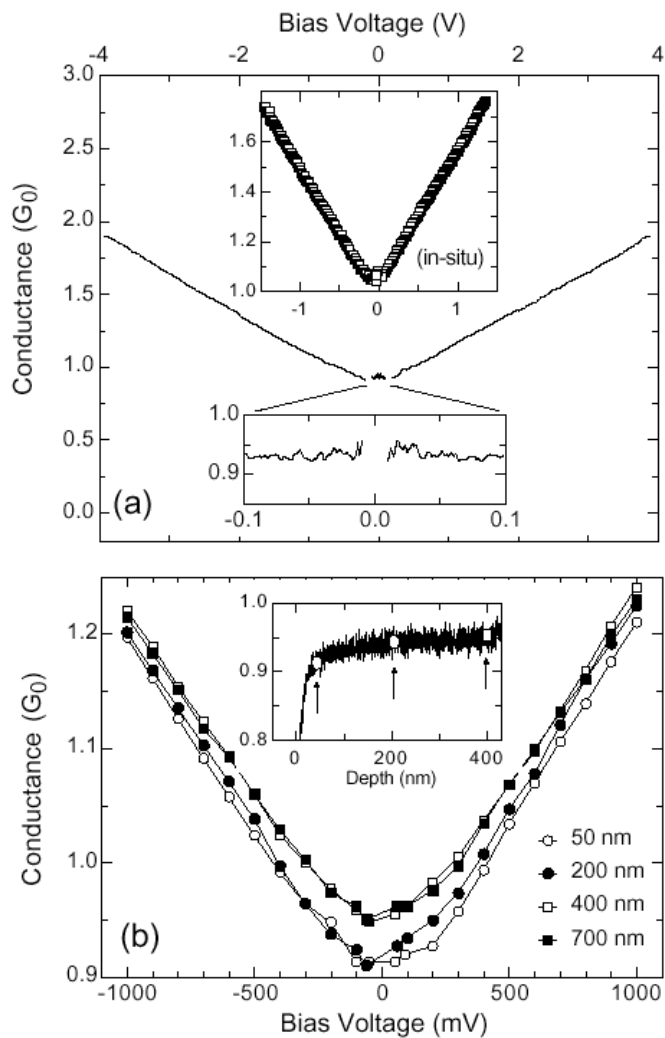


Figure 4.4: Conductance versus voltage  $G(V)$ . (a) For a clean nanotube in air from  $V = -4.0$  to  $+4.0$  V and from  $V = -1.3$  to  $+1.3$  V in the TEM (inset). Note the symmetry of  $G(V)$ . There is no saturation (a decrease in conductivity) with increasing voltage in this case. The current at  $V = 4$  V corresponds to  $I = 615 \mu\text{A}$ . (b)  $G(V)$  of a nanotube for various positions  $x$  into the Hg as indicated on the  $G(x)$  trace in the inset. Inset: open circles show the different positions in situ measurements of  $G(V)$  of a nanotube contacted in the TEM.

### 4.2.2 Surfactant-coated Nanotubes

Nanotubes coated with a surfactant have anomalous  $G(V)$  properties. An example is shown in Figure 4.5. The conductance rises but neither linearly nor is it symmetric with respect to  $V = 0$ . This behavior is representative of the modification effect observed with surfactants, which show various degrees of asymmetries and shifts compared with the pure case.

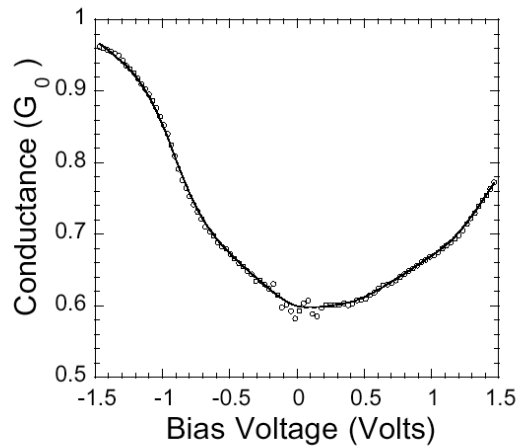


Figure 4.5: Effect of surfactant on  $G(V)$ . An example of  $G(V)$  for a surfactant coated nanotube. Note the differences with clean tubes, in particular the non-linearity and the asymmetry with respect to  $V = 0$ . The conductance saturates for  $V = -1.5$  V. This behavior is reproducible for this nanotube, however the shift and the asymmetry is sample dependent.

### 4.3 Measurements of variable contacts

The increased conductance with increasing bias voltage is a universal feature of all the nanotubes we have measured. Variation in the linear behavior is observed at higher voltages due to variable contacts between nanotubes and metal. Figure 4.6 shows

an example of transport of a carbon nanotube measured in the TEM. The distance from contact to contact measured along this 16 nm diameter nanotube was 0.8  $\mu\text{m}$ . Only a small segment of the nanotube and its tip contacted the Hg surface in the course of this measurement. The MWNT was slightly bent due to the stress. The conductance is measured as a function of voltage continuously, where the voltage is swept at a rate of 2 Hz spanning the voltage range from  $-V_{max}$  to  $+V_{max}$  with  $V_{max} = 1.6 \sim 2.4$  V. The pattern evolves in time as the contact of the MWNT with the Hg surface changes due to drift. Hence the differences from one sweep to the next primarily reflect slight changes in the contact of the nanotube with the Hg.

The initial conductance was quite low (shown in Figure 4.6-a). When the bias voltage reached 1.5 V the conductance jumped abruptly (in Figure 4.6-b) from about 0.1  $G_0$  to 0.22  $G_0$ . A stable pattern developed for many sweeps (in Figure 4.6-c). Both the slope ( $\sim 0.13$   $G_0/\text{V}$ ) and the zero-bias conductance,  $G(V=0) \sim 0.07$   $G_0$  gradually increased slightly. After about 20 sweeps the bias voltage sweep range was increased, which induced a change in  $G(V)$  (shown in Figure 4.6-d-e) :  $G(V=0) \sim 0.22$   $G_0$ ;  $dG/dV \sim 0.2$   $G_0/\text{V}$ . The patterns remain remarkably symmetric. After further increasing the bias voltage sweep range the conductance increases (shown in Figure 4.6-f),  $G(V = 0 \text{ V}) \sim 0.52$   $G_0$ ,  $dG/dV \sim 0.2$   $G_0/\text{V}$ , however now the conductance attains a maximum:  $G(1.6 \text{ V}) = 0.77$   $G_0$ . Although the conductance decreases above  $\sim 1.5$  V in this case, the current  $I = V \cdot G$  continues to increase but at a lower rate. The  $G(V)$  pattern is stable. Subsequently, the bias voltage sweep range was expanded to  $\pm 3$  V, and the nanotube is burned and failed at  $V = 2.9$  V. At that point  $G(2.9 \text{ V}) = 0.6$   $G_0$ . The failure occurs near the Hg contact (where also some contamination was observed).

Another example of the TEM observations is presented in Figure 4.7. The nanotube is 10 nm diameter of which a length of 2.5  $\mu\text{m}$  spans the distance from the fiber to Hg. In Figure 4.7-a, the nanotube was slightly bent at the tip where it contacted the Hg, causing an angle of about 45 degrees of the nanotube with the Hg surface. Initially, the contact to the Hg was small and the nanotube did not appear to penetrate through the Hg surface. In this configuration the conductance  $G(V=0) \sim 0.15 G_0$  with a slope  $dG/dV \sim 0.05 G_0/V$ , maximizing at 2.3 V:  $G(2.3 \text{ V}) = 0.27 G_0$ , and decreasing at higher applied voltages. This pattern was reproducible and stable. When the fiber was pushed closer to the Hg surface (Figure 4.7-b), the geometry abruptly changed. This change was consistent with the nanotube submerging on the order of  $1\mu\text{m}$  below the Hg surface, as expected when the pressure of the nanotube exceeds the Hg surface tension. At this point the conductance increased to  $G(V=0) = 0.48 G_0$  with a slope  $dG/dV \sim 0.2 G_0/V$ . In this configuration the conductance did not maximize up to bias voltages of 2.2 V. The current at 2 V is about 140  $\mu\text{A}$ , with no sign of saturation in this case. The earlier configuration was reproduced by retracting the fiber, giving similar  $G(V)$  behavior as before, displaying a maximum conductance.

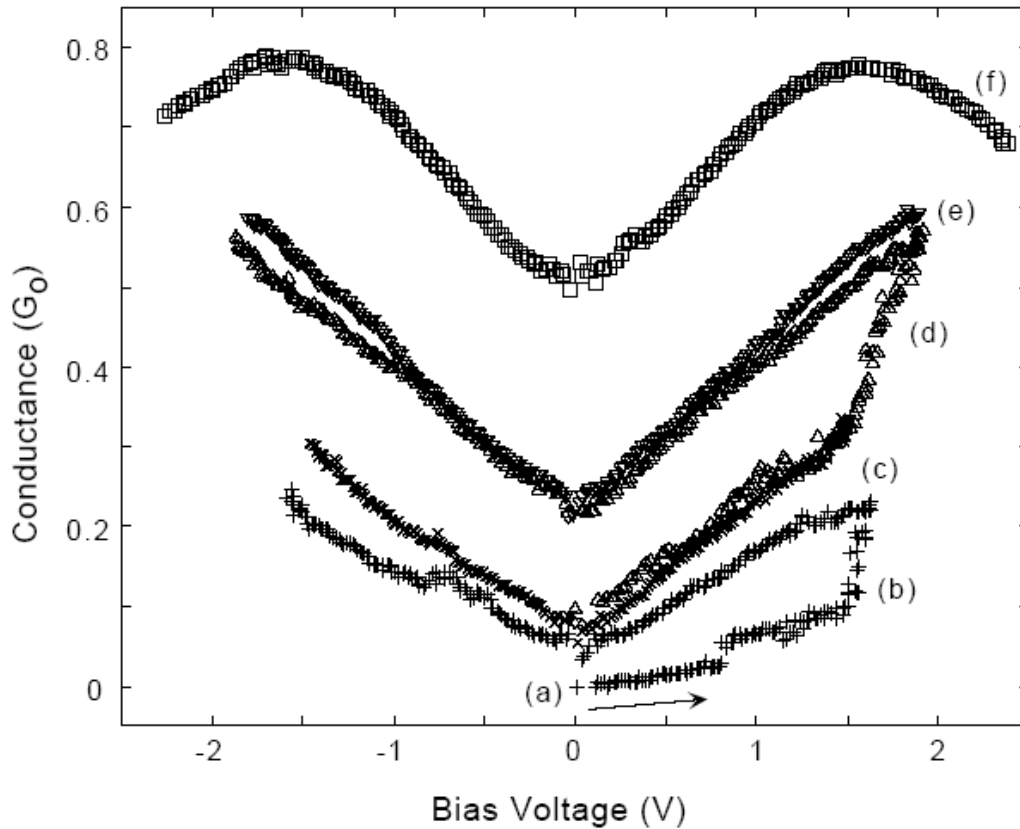


Figure 4.6: Conductance  $G(V)$  vs.  $V$  for a MWNT contacted to Hg in the TEM for successive voltage sweeps from  $0 \text{ V} \rightarrow V_{max} \rightarrow 0 \text{ V} \rightarrow -V_{max} \rightarrow 0 \text{ V}$ . The low-bias conductance is initially low (at **a**). When the bias voltage reaches 1.5V the conductance jumps abruptly (**b**). A stable linear pattern develops for many sweeps (**c**). The bias voltage sweep range is then increased, which induces a change (**d**) in the conductance. The new pattern (**e**) is stable. After again increasing the bias voltage sweep range,  $G(0)$  increases again and the stable characteristics (**f**) is obtained. Now the conductance attains a maximum. The bias voltage sweep range was next increased to 3V, and the nanotube failed at  $V=2.9 \text{ V}$ .

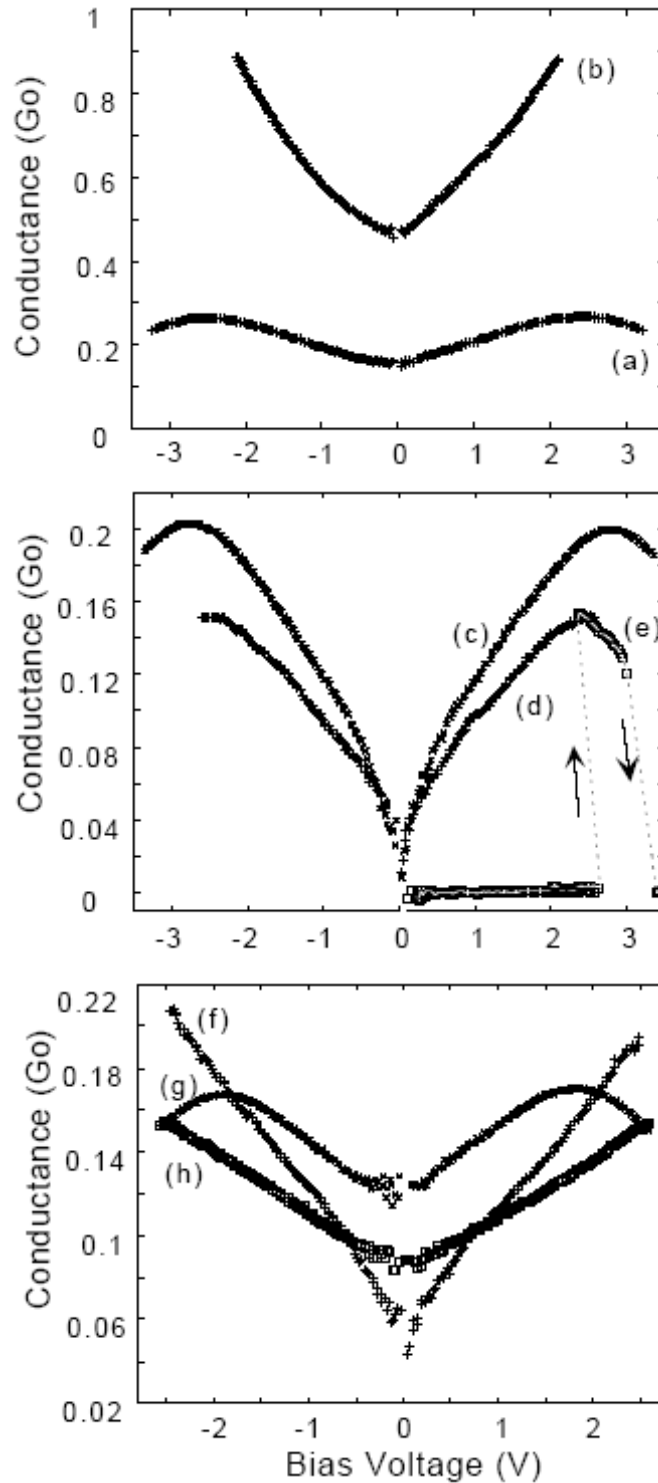


Figure 4.7: Conductance  $G(V)$  vs.  $V$  for a nanotube (10 nm diameter, 2.5  $\mu\text{m}$  long) contacted to Hg in the TEM. **(a)** Initially, the contact to the Hg is small and the nanotube appears to bend over the Hg surface. **(b)** After the fiber is pushed closer to the Hg surface, the contact geometry is more consistent with the nanotube submerging on the order of 1  $\mu\text{m}$  below the Hg surface. **(c)** The tube is retracted to produce a small contact,

and retracted slightly further in **(d)**. In **(e)** the contact area was so small that the nanotube drifted out of contact, causing  $G(V) = 0$ . Contact spontaneously reestablished at  $G(V=2.8V)$ , which coincides with the previous voltage sweep **(d)**. The nanotube then failed ( $V_{bias}=3$  V,  $G(3V)=1.2 G_0$ ) at the contact with the Hg. **(f-h)** Summary of the  $G(V)$  characteristics observed at small contact for the same tube. Note in particular the variation in  $G(0)$ , the range of  $dG(V)/dV$ , the  $G(V)$  shape variation, the fact that some curves intercept others. Since only the contact with the Hg surface varied, the observed variations should be ascribed to the contact properties.

The nanotube was then further retracted to produce a small contact giving rise to the  $G(V)$  in Figure 4.7-c. As for Figure 4.7-a,  $G(V=0)$  is small and  $G(V)$  maximizes. The nanotube was retracted slightly further, producing  $G(V)$  in Figure 4.7-d. The contact area was so small that the nanotube drifted out of contact at the next voltage sweep, causing  $G(V)=0$ . Contact spontaneously reestablished at  $G(V= 2.8 V)$  (Figure 4.7-e), which coincides with the previous voltage sweep in Figure 4.7-d. The nanotube then failed ( $V_{bias} = 3$  V,  $G(3 V) = 0.12 G_0$ ) at the contact with the Hg, obliterating a fraction of the nanotube at the Hg contact.

The  $G(V)$  behavior of this MWNT is representative of many tubes we have measured. Note in particular the variation in  $G(V=0)$ , which ranges from 0.01 to 0.5  $G_0$ , the range of  $dG(V)/dV$  which is always symmetrical and positive up to at least  $\pm 1.5$  V, the fact that a maximum  $G$  is observed in some of the scans but not in others. Most strikingly, as seen in Figure 4.7 (f-h) when the tube makes a small contact with Hg some curves intercept others. Since only the contact with the Hg surface varied, the observed variations should be ascribed to the contact properties.

#### 4.4 Observations of non-conducting MWNTs

In situ TEM investigations show that not all nanotubes conduct. Nanotubes that are clearly in contact with the liquid metal may exhibit resistances above our measurement limit of  $1 \text{ M}\Omega$ . Moreover, these nanotubes ( $\sim 1 \text{ }\mu\text{m}$  from contact to contact) typically can withstand voltages exceeding 5 V. This indicates that these tubes are robust insulators, and tunneling into deeper metallic layers is apparently inhibited.

Figure 4.8 is an example of the conductance of a highly resistive MWNT. The tube, clean and straight, was  $6 \text{ }\mu\text{m}$  long. It was submerged straight into Hg by at least one  $1 \text{ }\mu\text{m}$ . Great care was taken to make contact with a clean spot of Hg. At a certain point a clear meniscus was formed at the tip touching the Hg surface. The conductance is low  $G(V=0) = 10^{-3} G_0$  and increases very slightly with voltage with  $dG/dV = 9 \cdot 10^{-3} G_0/V$ .

In two cases a conducting MWNT contacted the Hg. The conductance was  $G(V=0) \sim 0.6$  and  $\sim 0.1 G_0$  respectively. The conductance increased with increasing bias voltage and maximized at 1.5 V and 2.5 V respectively. The tube failed about 1V above the maximum of  $G$  and the remaining stem was re-contacted to Hg. But this time the conductances were very low ( $G(V=0) \sim 10^{-3} G_0$ ) and the stem eventually failed at a voltage above 7 V.

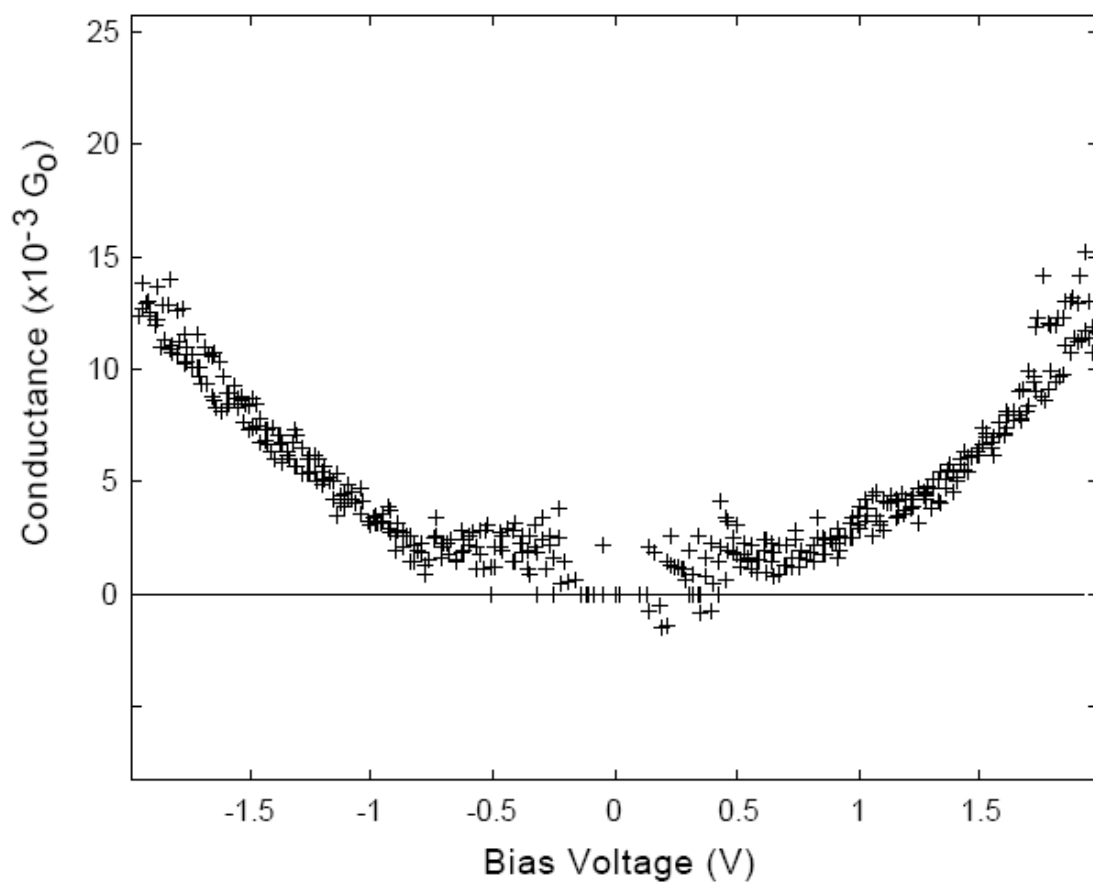


Figure 4.8: Conductance of a highly resistive MWNT submerged over 1  $\mu\text{m}$  in Hg.

## 4.5 Observations of Nanotube Failure

Observations of nanotube failure at high currents are summarized in Figure 4.9. Clean defect-free conducting MWNTs typically break at the Hg contact shown in Figure 4.9(a-b), at a bias voltage ranging from  $V_{bias} = 2.5\sim 4$  V, for both positive and negative polarities. It is remarkable that we have never observed nanotubes failing at the fiber contact. Highly resistive nanotubes have also been observed to fail at the Hg contact.

Defective MWNTs typically fail at the defect as shown in the TEM micrographs in Figure 4.9(c-d). A defective nanotube has a higher than usual resistance, which is ascribed to scattering at the defect, leading to a large potential drop at the defect, and likely (but not necessarily) to dissipation at the defect. Figure 4.9(c-d) shows TEM picture before and after failure for one MWNT with a kink and two contaminated MWNTs, showing that the failure occurred at the defects. This resulted in two tapered endings, with one protruding from the liquid mercury. We have not observed nanotubes, which broke in the middle (as observed by Collins, *et al.* (Collins, 2001)).

The HRTEM image of a nanotube in Figure 4.9(e-f) (pictured taken by Ugarte) shows how the nanotube surface (possibly only a single layer) was disrupted at the end of the nanotube that contacted the solid metal electrode (gold in this case) due to the high current, giving it the molted appearance. These properties are typical and others have obtained similar results (Cumings, 2000; Collins, 2001).

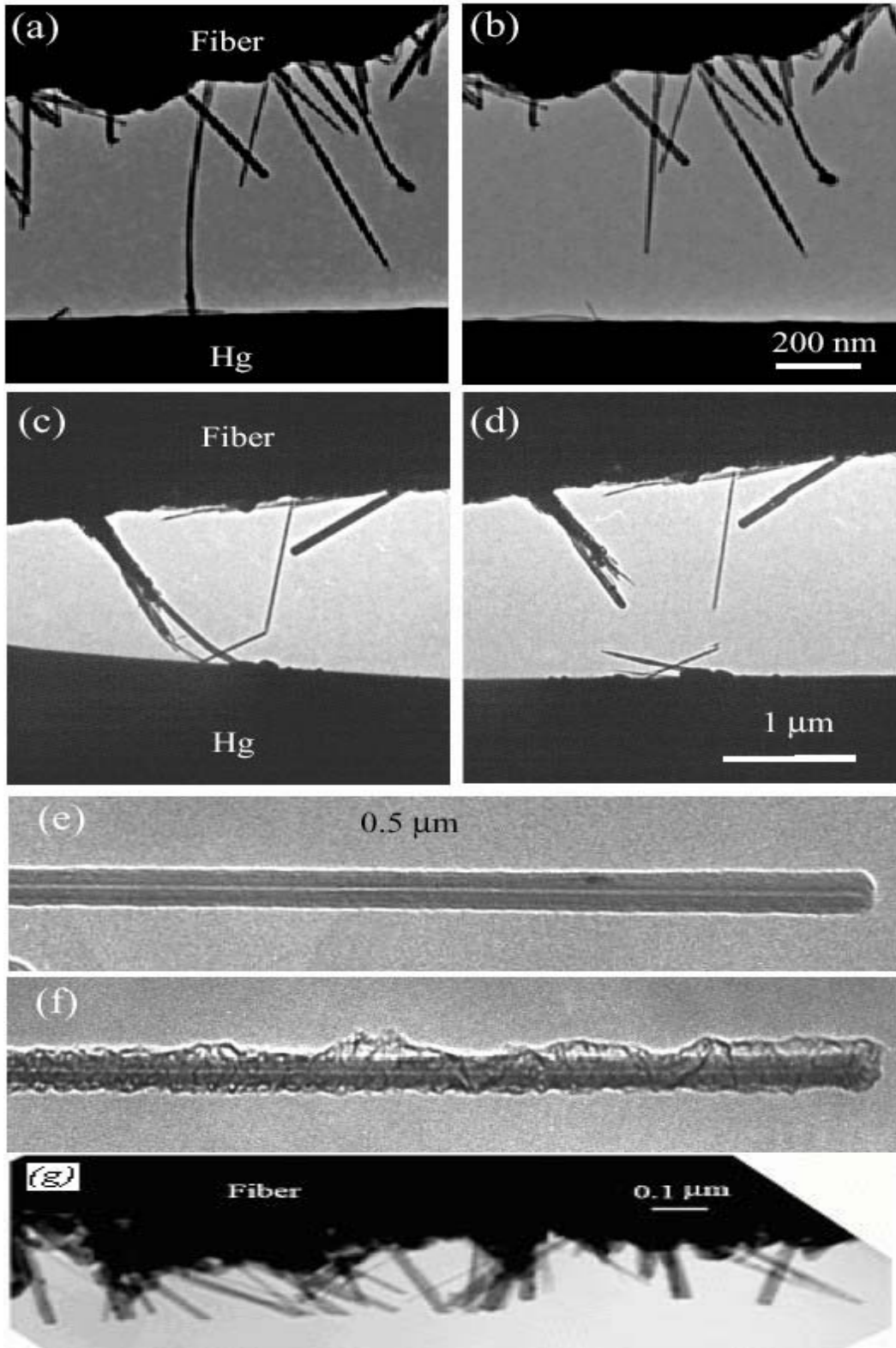


Figure 4.9: Before and after in situ TEM images of nanotubes contacted with Hg and their failure at high currents. (a-b) Typical failure of a clean nanotube. The failure occurred at the

contact with the Hg after applying 4 V leaving a short (~20 nm long) stem at the original contact point. Before the failure the measured resistance was  $12.7 \pm 0.2$  k $\Omega$ . (c-d) One kinked and two contaminated nanotubes, showing that the failure occurred at the defects. (e-f) High resolution images of the failure of a clean gold contacted nanotube showing that only the outer layer is affected, which corresponds to the current flow pattern in these tubes (pictured taken by Ugarte). (g) Failure of many tubes in parallel at the contact with the Hg resulting in the “cut grass” appearance. This corresponds to the typical failure of clean tubes as explained in the text.

The TEM image of Figure 4.9(g) dramatically illustrates the failure of many MWNTs that all contacted the Hg after the bias voltage was ramped from 0 V to 8 V. This resulted in the “cut grass” appearance. (At some point a Hg bubble was formed which made contact with the tubes; the phenomenon is described in details below.) This observation indicates that most of the power is dissipated at the Hg contact.

#### 4.6 Observations of Hg bubble formation

One of the most spectacular *in-situ* TEM observations is the formation of a Hg bubble-shape feature near the contact of a nanotube to the Hg surface. This phenomenon occurs when the nanotube is negatively biased with respect to the Hg, when only the tip of the nanotube touches the surface under high current conditions.

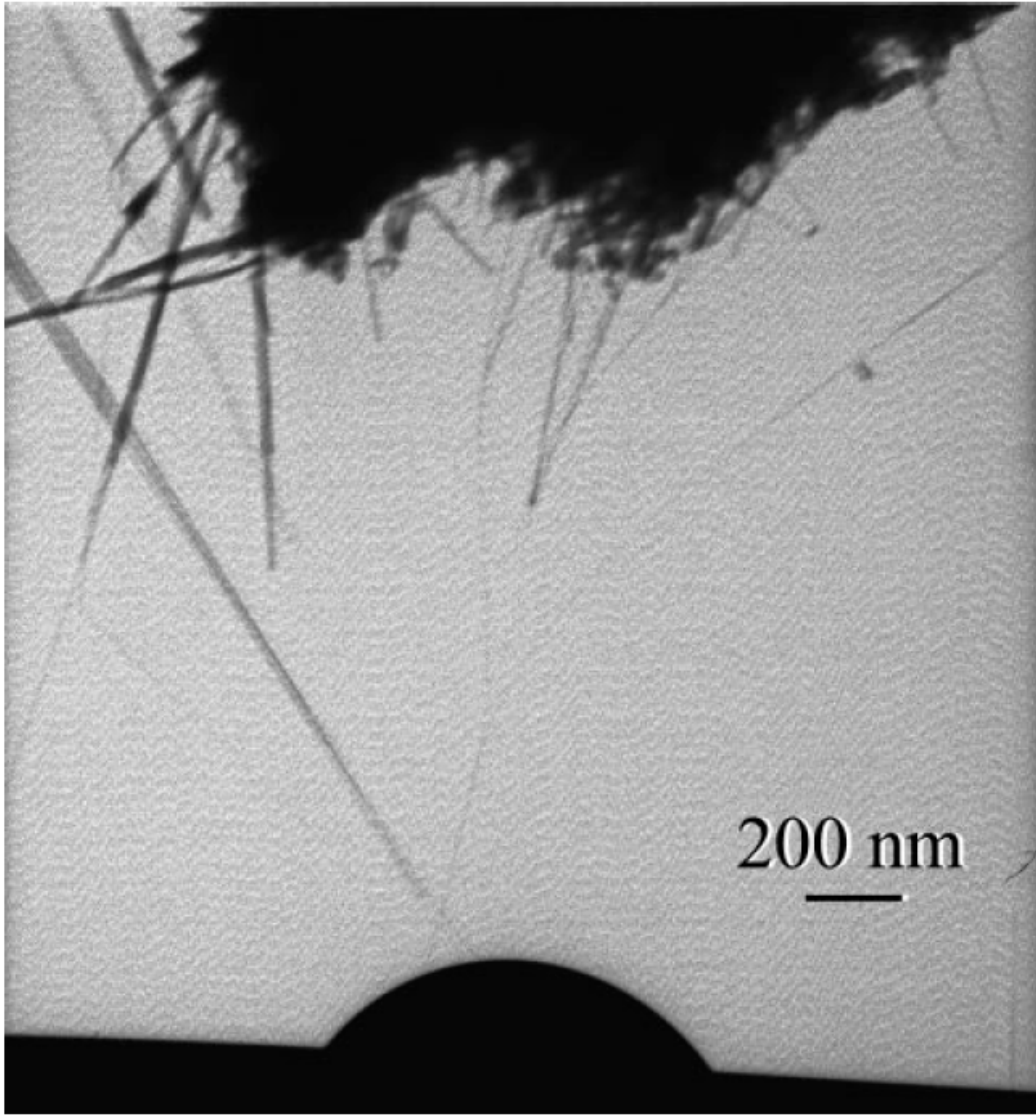


Figure 4.10: TEM picture of a Hg bubble stabilized at the contact of a nanotube to the Hg with a voltage of  $\sim 1.5$  V. The shape appears to be a spherical segment with a radius of  $0.5 \mu\text{m}$ . This phenomenon occurs when the nanotube is negatively biased with respect to the Hg, when only the tip of the nanotube touches the surface under high current conditions.

The Hg bubble can be stabilized by appropriately adjusting the voltage. In the case of Figure 4.10, a bubble of radius  $\sim 0.5 \mu\text{m}$  was kept stable for a bias voltage of 1.5 V (current  $\sim 0.14 \text{ mA}$ ). When the bias voltage is swept, then the bubble emerges and submerges synchronous with the applied voltage, much like a rising and setting moon. The bubble has been seen to burst after which a new one forms. The bubble does not form when the nanotube is positively biased. The fact that the bubble is spherical suggests that it is indeed liquid Hg (Figure 4.11), This is further strengthened by the observation of a meniscus at the nanotube-Hg contact (Figure 4.11). Furthermore, the bubbles are conducting, since such a bubble caused the failure of the nanotubes in Figure 4.9-g.

This phenomenon appears to occur only for specific small contacts to the Hg. The 10 nm diameter MWNT contacting the Hg contact produced bubbles for positive  $V$  (i.e. nanotube negatively biased with respect to the Hg).  $G(V)$  is shown in Figure 4.12-a. In Figure 4.12-b the tube had drifted away, causing the conductance and consequently the current to decrease for the same bias voltage. The bubbling phenomenon stopped. After re-approaching the tube to the Hg, contact was re-established in Figure 4.12-c, but this time no bubble formation was observed even for higher bias voltage and current than in Figure 4.12-a. Note that even when the bubbles are formed (Figure 4.12-a),  $G(V)$  is symmetric with respect to  $V=0$ .

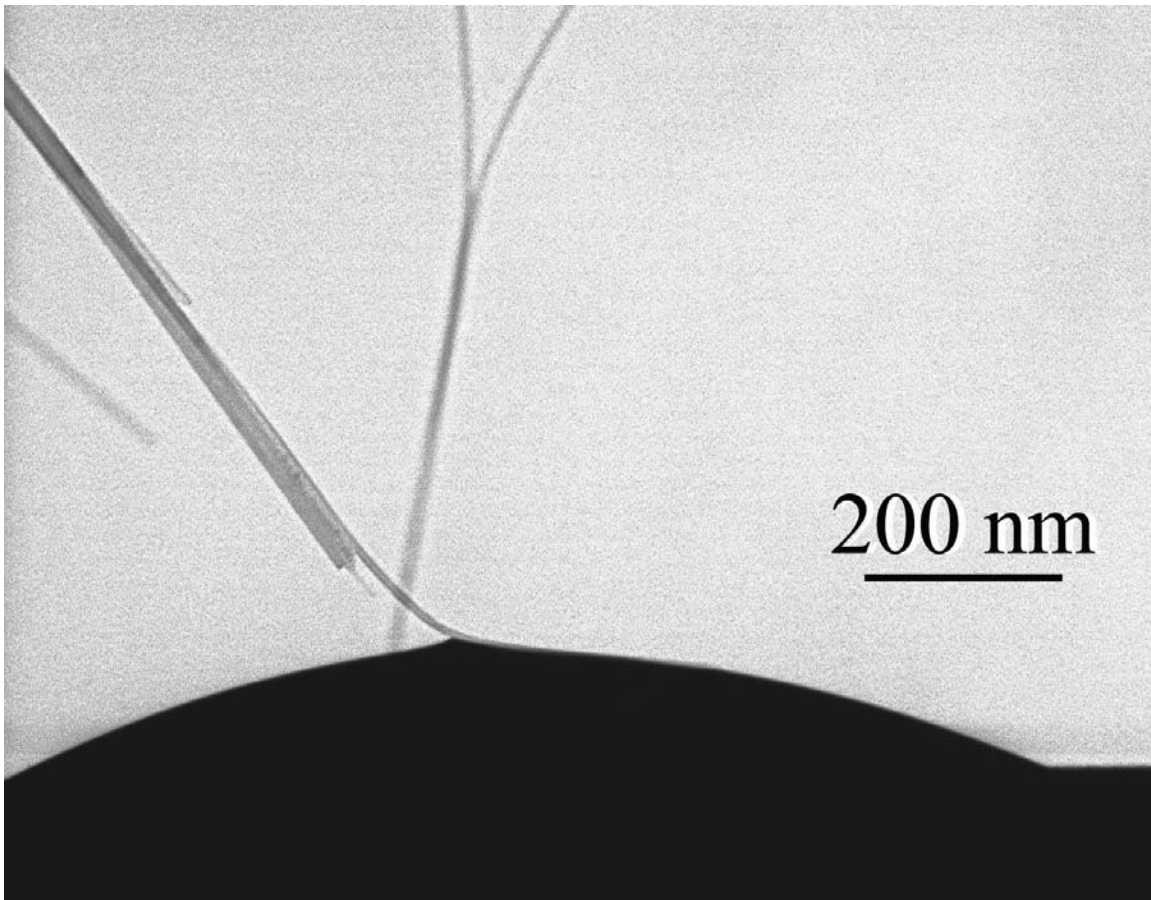


Figure 4.11: TEM picture of a Hg bubble stabilized at the contact of a nanotube to the Hg with a voltage of  $\sim 1.5$  V. Note the spherical shape of the bubble and of a meniscus at the nanotube-Hg contact. This phenomenon occurs when the nanotube is negatively biased with respect to the Hg, when only the tip of the nanotube touches the surface under high current conditions.

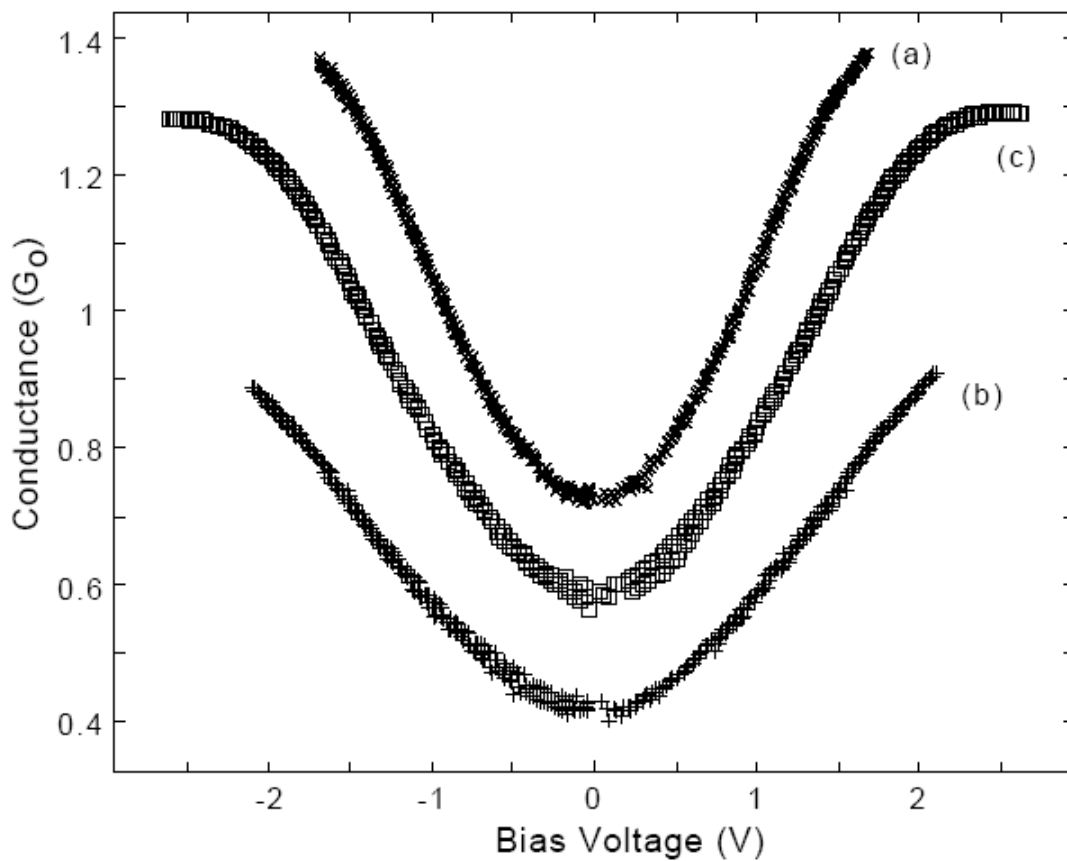


Figure 4.12: Conductance  $G(V)$  versus  $V$  for a tube (10 nm diameter) in contact with Hg. **(a)** Hg bubbles are formed. **(b)** The tube drifted away, causing the conductance to decrease. The bubbling phenomenon stopped. After pulling the tube out, contact was re-established in **(c)**. No bubble was observed even for higher bias voltage and current than in **(a)**, indicating the influence of the nature of the contact. In all cases, note the symmetry of the conductance versus polarity.

#### 4.7 Experiments with a small Hg droplet touching an HOPG surface

Figure 4.13 shows the measurement of the current-voltage characteristics of a Hg droplet touching an HOPG (Highly Oriented Pyrolytic Graphite) surface (Berger, 2002). It gives deeper insight into the nature of the contact. As shown in Figure 4.13, the conductance increases with increasing voltage. The increase is monotonic, essentially linear and reminiscent of the Hg-MWNT properties discussed above. The patterns are remarkably symmetric (a slight asymmetry is sometimes observed, that causes  $|dG/dV|$  to be slightly lower for the negatively biased Hg tip compared to the positively biased Hg tip).

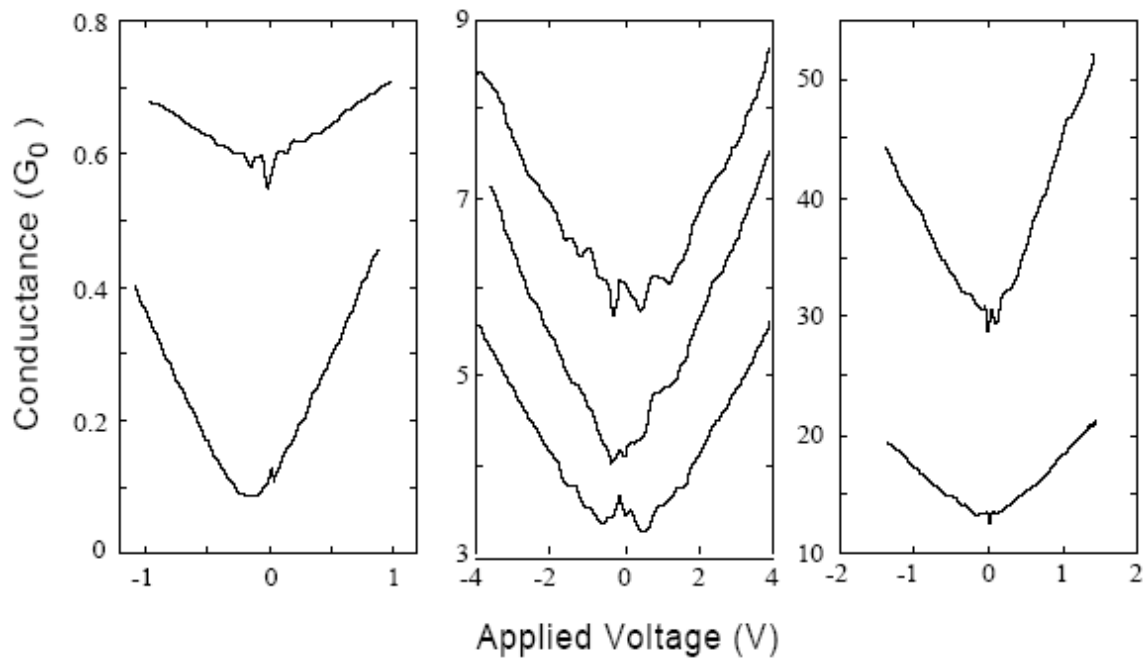


Figure 4.13: Conductance  $G(V)$  versus  $V$  for a HOPG sample contacted to a droplet of liquid Hg in air, for several different contacts (the larger the contact, the greater  $G(V=0)$ ). As for MWNT, the conductance increases with increasing voltage. The increase is monotonic, essentially linear and remarkably symmetric (Berger, 2002).

When  $G(V=0) > 1 G_0$ , the pattern approximately scales with the  $G(V=0)$ :  
 $(dG(V)/dV)/G(V=0) \sim 0.3 /V$ . For  $G(V=0) < 1 G_0$  the slope appears to be relatively  
constant:  $(dG(V)/dV) \sim 0.3 G_0/V$ .

## CHAPTER 5

### ANALYSIS AND INTERPRETATION

In this chapter the results and observations of SPM and TEM experiments on MWNTs are analyzed. At the end of this chapter the comparisons of our experimental results with theoretical expectations and with other labs' experimental results are given.

#### 5.1 Analysis of conductance curves

This section presents a detailed analysis of the conductance traces. The plateau curvature is determined by the increase in the total conductance of the system as the contact area with the Hg becomes larger and at the same time as the distance along the nanotube from contact to contact becomes shorter. Only the first rising steps are analyzed. The first rising step is the one following the first significant rise from  $G = 0$ , which corresponds to one nanotube in contact with the Hg.

The conductance properties of nanotubes are reflected at  $x = 0$  in the conductance traces  $G(x)$ , where  $x$  is the displacement of the SPM. Here we have set  $x = 0$  corresponds to the point where contact between the tube and the liquid metal is made and the conductance jumps up from 0. We concentrate primarily on longer plateaus to accurately quantify the resistance per unit length  $\rho$  of the nanotube. We provide two examples in detail, one of a typical nanotube with a plateau value near  $1 G_0$ , and another with a significantly reduced plateau value. These are representative results of many measurements of these plateaus. These experiments and their analysis have been carried out over the past five years and the results we present here are clear examples of typical behavior.

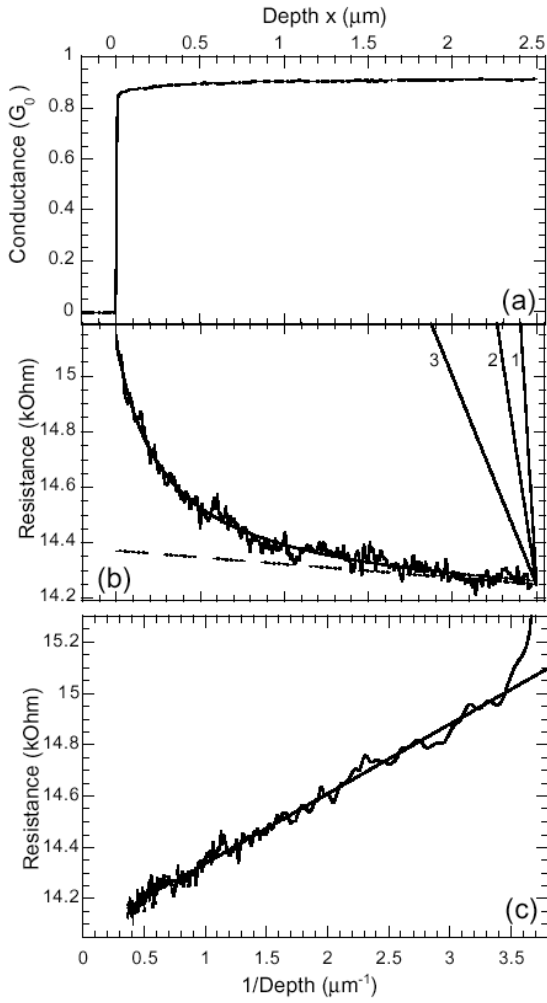


Figure 5.1: A representative conductance trace (one of 50 of this nanotube) as a function of the distance  $x$  between tip of the nanotube and the Hg surface (i.e. the depth of the nanotube merged inside the mercury). (a) The conductance  $G(x)$  in units of the conductance quantum, showing the initial conductance jump at  $x=0$  to  $0.85 G_0$ , followed by a rounded step, of which the slope gradually decreases to 0 with increasing  $x$ . (b) The resistance  $R(x)=1/G(x)$ . Note that the slope gradually decreases to 0. Dashed line corresponds to the slope at  $x = 2.5 \mu\text{m}$ , which corresponds to the upper limit of the tube resistance:  $\rho < 48 \Omega/\mu\text{m}$ ; line (1) corresponds to  $\rho = 10 \text{ k}\Omega/\mu\text{m}$  found in Reference (Bachtold, 2000) for MWNTs; line (2)  $\rho = 4 \text{ k}\Omega/\mu\text{m}$  found in Reference (Schonenberger, 1999), and line (3)  $\rho = 1.5 \text{ k}\Omega/\mu\text{m}$  found for a SWNT bundle which was characterized as a ballistic conductor in Reference (Bachtold, 2000) (c) Nanotube resistance plotted as a function of  $1/x$ , revealing a straight line:  $R(1/x) = 14.1 + 0.271/x \text{ k}\Omega$ . This demonstrates that the contact resistance indeed determines the shape of the conductance trace.

Figure 5.1(a) shows a typical conductance trace and consists of a rapid rise in the conductance at  $x = 0$ , followed by a rounded step with a flat plateau near  $G_{pl} = 0.9 G_0$ . This trace is typical of the 50 recorded traces of this plateau. This plateau is long and extends for  $2.5 \mu\text{m}$  and has the characteristic rounded shape close to  $x = 0$ .

Figure 5.1(b) shows the same plateau, but now represented in terms of resistance  $R(x) = 1/G(x)$ . Assume that the length of the exposed nanotube outside the fiber is  $L$ . Recall that  $x$  is the length of the tube submerged inside the liquid metal, so  $(L-x)$  is the length of the tube between the fiber-tube contact and the mercury-tube contact. If we assume that the nanotube resistance per unit length is  $\rho$ , then the intrinsic tube resistance is  $(L-x)\rho$ . Let  $R_C$  represents the combined contact resistances, by Ohms law, the total resistance is

$$\begin{aligned} R(x) &= R_C + R_{tube} \\ &= R_C + (L-x) \rho \end{aligned} \tag{5.1}$$

$$dR(x)/dx = dR_C(x)/dx - \rho \tag{5.2}$$

Since  $R(x)$  is not at all represented by a straight line indicates that the contact resistance also depends on  $x$ .

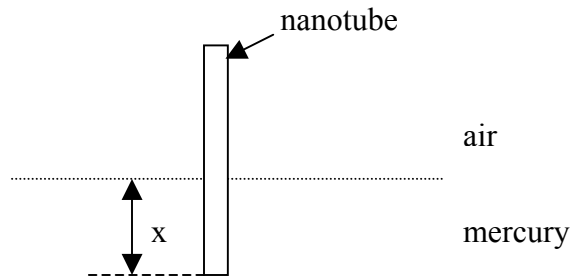


Figure 5.2: Diagram of a tube in contact with mercury.  $x$  represents the length of the tube submerged inside the mercury. The contact area of a tube with mercury includes the tip area and the area of the sidewall of the tube. The tip area is constant. The area of sidewall is proportional to  $x$ . Thus the total contact area is proportional to  $x$ .

The combined contact resistances include the metal-tube and fiber-tube contact resistances. The metal-tube contact resistance includes the contact resistance at the tip ( $R_{tip}$ ), and at the sidewall of the tube with mercury ( $R_{sidewall}$ ).  $R_{tip}$  is constant, and  $R_{sidewall}$  varies inversely proportionally with the contact area (see in Figure 5.2). Hence  $R_{NT-M} = (R_{tip}^{-1} + R_{sidewall}^{-1})^{-1} = (R_{tip}^{-1} + (R_{NT-M}^*/x)^{-1})^{-1} \approx R_{NT-M}^*/x$  (for large  $x$ ), here  $R_{NT-M}^*$  is related to the transmission probability decided by scattering at the sidewall tube-mercury contact. The resistance of the contact to the fiber  $R_{NT-F}$  is constant. In total, the classical nanotube resistance is given by

$$R(x) = R_{NT-F} + (L-x) \rho + R_{NT-M}^*/x \quad (5.3)$$

Because  $dR(x)/dx = - (R_{NT-M}^*/x^2 + \rho)$ , we can immediately establish an upper bound for  $\rho$  by measuring the  $dR(x)/dx$  for large  $x$ . From Eq. (5.3) it is clear that:

$$\rho < | -dR(x)/dx | \quad (5.4)$$

For this trace we find the upper bound (at  $x = 2.5 \mu\text{m}$ ):  $\rho < 48 \Omega/\mu\text{m}$  shown in Figure 5.1(b). Hence, from this elementary analysis of this trace we find that the contribution to the total resistance per micron length is at most  $50 \Omega$ , which is a factor of 260 less than  $13 \text{ k}\Omega$  ( $\sim 1/G_0$ ). The significance of this is presented below.

Figure 5.1(b) also shows results  $\rho = 4 \text{ k}\Omega/\mu\text{m}$  (Schonenberger, 1999) and  $\rho = 10 \text{ k}\Omega/\mu\text{m}$  (Bachtold, 2000), which are much larger than the upper limit found here. To refine this value, we must evaluate the contact term  $R_{NT-M}$ .

When  $\rho$  is small, the plateau resistance is classically approximately given by  $R_{plateau} = R_{NT-F} + R_{NT-M}^*/x \approx R_{NT-F}$  according to Eq. (5.3), since  $x$  is large at plateau, in this case,  $x = 2.5 \mu\text{m}$ , the term of  $R_{NT-M}^*/x$  is negligible.

Plotting the resistance  $R$  with respect to  $1/x$  (while appropriately accounting for the conductance step at  $x = 0$  is given below) clearly demonstrates the contact resistance effect shown in Figure 5.1(c). The result is a straight line which intercepts  $1/x = 0$  at  $R_{plateau} = 14.1 \text{ k}\Omega$  and which has a slope  $R_{NT-M}^* = 270 \text{ }\Omega\cdot\mu\text{m}$ . This unambiguously demonstrates that the shape of the conductance step is dominated by the contact resistance and not by the intrinsic nanotube resistance  $\rho$ .

The conductance curves are found to make a step at  $x = 0$ , which indicates a jump-to-contact of the metal to the nanotube tip. This effect is included in the contact resistance. Since  $(R_{NT-M})^{-1} = R_{tip}^{-1} + (R_{sidewall})^{-1} = R_{tip}^{-1} + (R_{NT-M}^*/x)^{-1}$ , for  $x = 0$ , its resistance is  $R_{tip}$ .

The smooth line running through the experimental data in Figure 5.1(b) represents the result of an unconstrained fit to Eq. (5.3) (including the  $R_{tip}$ ). The fitting equation is the following:

$$\begin{aligned}
R(x) &= R_{NT-F} + (L-x) \rho + R_{NT-M} \\
&= R_{NT-F} + (L-x) \rho + (R_{tip}^{-1} + R_{sidewall}^{-1})^{-1} \\
&= R_{NT-F} + (L-x) \rho + (R_{tip}^{-1} + (R_{NT-M}^*/x)^{-1})^{-1} \tag{5.5}
\end{aligned}$$

Here  $R_{NT-F}$  is assumed to be a constant,  $\rho$ ,  $R_{NT-M}^*$  and  $R_{tip}^{-1}$  are variables. For this trace  $\rho = 14 \text{ }\Omega/\mu\text{m}$ . Hence, only a small fraction of the slope at  $x = 2.5 \text{ }\mu\text{m}$  can be due to the intrinsic resistance of the tube. Furthermore, the contact resistance is found to be  $R_{NT-M}^* = 256 \text{ }\Omega\cdot\mu\text{m}$  from this fit (i.e. close to the value found from the slope in Figure 5.1(c)). The refinement on  $R_{tip}$  produces a better fit to the experimental data near the step. Typical values for  $R_{tip}$  are 3-6 k $\Omega$ .

The above procedure was incorporated in an automated fitting Matlab programs and applied to analyze the 50 measurements of this step. The slope of  $R$  at  $x = 2.5 \mu\text{m}$  is  $dR/dx = 87 \pm 52 \Omega/\mu\text{m}$ . The unconstrained fit (which allows negative values) gives a distribution of measured values with  $\rho = 31 \pm 47 \Omega/\mu\text{m}$  (shown in Figure 5.3). These values are typical for MWNTs investigated in this study.

Furthermore, the contact resistance found from the fit of the 50 measurements is  $R^*_{NT-M} = 167 \pm 55 \Omega \cdot \mu\text{m}$ . Note that others find comparable contact resistances. In particular, Schonberger *et al.* use conventional nano-fabrication technology to make the NT-metal contact and find  $3.8 \text{ k}\Omega$  average contact resistances for 100-200 nm wide MWNTs, which corresponds to a resistance per unit length:  $R^*_{NT-M} = 380\text{-}760 \Omega \cdot \mu\text{m}$  (Schonberger, 1999).

Another series of 70 measurements of a  $2 \mu\text{m}$  plateau with a particularly low plateau conductance ( $\sim 0.5 G_0$ ) in Figure 4.3(c) similarly analyzed is presented next. From the distribution of the measurement values of this plateau, we find that  $\rho = 40 \pm 45 \Omega/\mu\text{m}$  and  $R^*_{NT-M} = 1100 \pm 130 \Omega \cdot \mu\text{m}$ . From the TEM experiments, we know that the nanotubes typically protrude a few microns out from the fiber, so the maximum contribution to the resistance due to the nanotube is of the order of a few hundred Ohms. Hence, this analysis shows that the reduced plateau value (i.e.  $G_{pl} \sim 0.5 G_0$  rather than  $\sim 1 G_0$ ) is not due to the nanotube intrinsic resistance, but rather due to a larger than normal contact resistance at the nanotube-fiber contact, which is discussed in detail next.

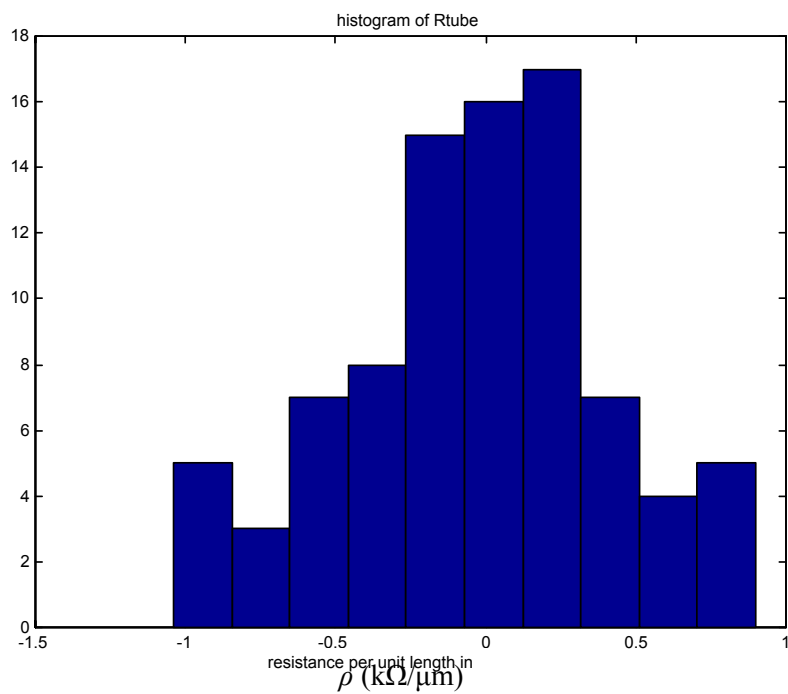
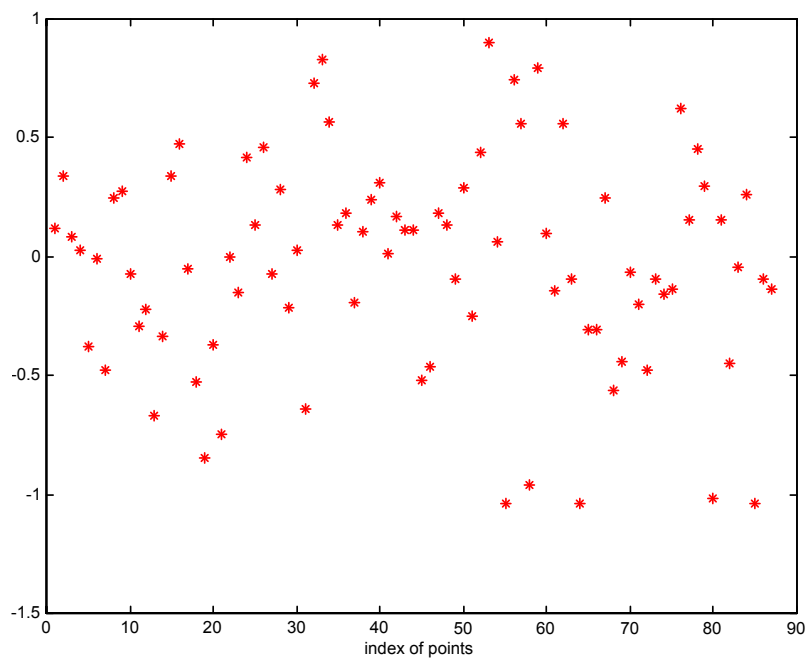


Figure 5.3: The distribution of measured values of nanotube resistance per unit length  $\rho = 31 \pm 47 \Omega/\mu\text{m}$ .

The important messages we gain from above analysis is that the intrinsic MWNT resistances are very low; in fact they are orders of magnitude lower than those reported by others including both MWNTs and SWNTs. We stress that because the contributions both from the contacts and from the nanotube act to increase the conductance with increasing  $x$ , therefore the contact contribution cannot possibly compensate the resistive contribution of the nanotube. Furthermore, since the two contributions have different functional dependences on  $x$ , they can be isolated as was done in the above analysis.

## 5.2 Ballistic transport in carbon nanotubes

Following Bachtold *et al.* (Bachtold, 2000), ballistic transport on a length scale of 1  $\mu\text{m}$  is unambiguously demonstrated when  $T > \frac{1}{2}$  in Eq. (2.8) for a 1  $\mu\text{m}$  nanotube, because then the majority of electrons traverse the nanotube without scattering. Because  $R = L\rho$ , this criterion is satisfied up to distances  $L_{max}$  defined by

$$L_{max} = (h/4e^2)/\rho \quad (5.6)$$

Here  $\rho$  is the intrinsic tube resistance per unit length. In our experiments, we will try to find the value of  $\rho$  in order to calculate the distance  $L_{max}$ .

As explained earlier, the slope in the conductance trace provides an upper limit for  $\rho$ . For the plateau of Figure 5.1,  $\rho < 50 \Omega/\mu\text{m}$  and hence  $L_{max} = 130 \mu\text{m}$  according to Eq. (5.6). Nanotubes shorter than this are room-temperature ballistic conductors over their entire length. Correcting for the contact resistance (i.e. using refinement on  $R_{tip}$ ) yields  $\rho = 31 \pm 61 \Omega/\mu\text{m}$ , which implies

$$L_{max} \sim 200 \mu\text{m}. \quad (5.7)$$

This length is much longer than the length of the nanotubes. It implies that MWNTs are

ballistic conductors at room temperature for lengths up to at least a fraction of one mm. Even if as many as 10 layers were involved in the transport (so that the total number of conducting subbands  $N=20$ ), then the mean free path is still larger than  $1 \mu\text{m}$  and the tube would still be ballistic on the micron length scale. We emphasize that this is really the worst possible case: all layers contribute to the transport (in contrast to several experimental findings) and the resistivity is over estimated (that is, the contact length-dependent resistivity is ignored: all the dependence is ascribed to the intrinsic nanotube resistivity). Hence, on the basis of this analysis, these free standing clean nanotubes are indeed ballistic conductors at room temperature.

The results found here are typical for the nanotubes studied. Hence MWNTs are not only unambiguously room-temperature ballistic conductors, but over unprecedented distances. The results cannot coherently be explained in term of multiple conducting subbands (with reduced transmission coefficients). First, in order to have diffusive behavior with  $\rho=100 \Omega/\mu\text{m}$  with a mean free path of the order of  $L_m = 0.2 \mu\text{m}$  (which is the quasi-ballistic scattering length quoted in Reference (Schonenberger, 1999)), because  $G = NG_0 = L_m \rho$  (ballistic conductor  $T_i = 1$ ), it would require by Landauer theory (Datta, 1995).

$$N = (L_m \rho G_0)^{-1} = 650 \text{ Channels.} \quad (5.8)$$

In contrast, the number of participating channels is experimentally found to be of order unity (Schonenberger, 1999; Liu, 2001) as expected theoretically as well, and even for deliberately heavily doped samples (Martel, 1998). Bachtold *et al.* demonstrated that only the top layer participates to the transport (at least at low temperatures) (Bachtold, 1999).

Second, our measured two-probe conductance values are always near  $1 G_0$ . There is no physical reason the contact resistances of spuriously doped nanotubes with a large variety of diameters would exhibit such an effect.

### 5.3 Scattering at Contacts

During these experiments over several years, we find that plateau conductances  $G_{plateau} \leq 1 G_0$  and that these values near  $0.9 \pm 0.1 G_0$  are the most common. Many cases have been recorded for which the  $G_{plateau} < 1 G_0$ , and examples are given here. In particular,  $G \sim 0.5 G_0$  are observed relatively frequently, although these plateaus often (but not always) abruptly progress to plateaus near  $1 G_0$ . In contrast, we have not observed initial conductance steps that are significantly greater than  $1 G_0$ . Furthermore, the plateaus are invariably flat (not sloped) with a rounded step. Hence, even allowing for a distribution in plateau values, the cutoff at  $1 G_0$  appears to indicate that only one quantum of conductance is involved rather than two. One of possible explanations for the ‘missing’ quantum of conductance is due to the fiber-NT contact pointed out in de Heer’s earlier work (Frank, 1998; Poncharal, 1999). Another possible explanation is related to the properties of the metal-nanotube contact. The  $\pi$  and  $\pi^*$  bands couple very differently to the electrodes (such as Al and Au) and one of them is almost shut down for transport for end-contact, which results in only one metallic band for transport (Palacios, 2003). Below we give another possible explanation in terms of reflections from the nanotube-fiber contact.

To proceed, we first develop a semi-classical model for the contacts. This development, presented in Reference (Berger, 2002), follows that originally proposed in

References (de Heer, 1997 in Nanowires; de Heer, 1997 in Z. Phys. D), which is based on the Landauer theory (Datta, 1995) and related to the Datta's semi-classical discussions (Datta, 1995). The methods were developed to explain fractional conductances observed in gold nanowires (de Heer, 1997 in Nanowires) and carbon nanotube networks (de Heer, 1997 in Nanowires; de Heer, 1997 in Z. Phys. D). The point of the model is to find expressions for the transmission coefficients in the Landauer equation. The model assumes that the elastic scattering of an electron at interfaces and scattering centers is isotropic. Hence an incoming electron scatters with equal probability into each of the outgoing channels (similar to the isotropy condition (Beenakker, 1997)). Quantum interference effects are ignored, but multiple reflections are considered. Accordingly, the total resistance of a nanotube of length  $(L-x)$  with two conducting channels, contacted to a metal contact of length  $x$  at one end and to a non-reflecting contact at the other end, is

$$R(x) = (2G_0)^{-1} ((C_I x)^{-1} + (L-x)/L_0 + I) \quad (5.9)$$

This resembles the classical Ohmic expression (Eq. (5.3)) although it does not assume diffusive transport but rather it relies on transmission and reflection of electrons at the interfaces of the various elements. The first term represents the nanotube-metal contact;  $C_I$  is an empirical constant that can be estimated from the Sharvin equation (Sharvin, 1965)

$$C_I \sim \pi r / \lambda_F^2 \quad (5.10)$$

here  $r$  is the nanotube radius and  $\lambda_F$  is the Fermi wavelength in the nanotube. With  $\lambda_F \sim 40$  nm for graphite (Kelly, 1981), and  $5 \text{ nm} < r < 10 \text{ nm}$  then the conductance of the metal-nanotube contact is  $2G_0C_I$  and  $30 \mu\text{m}^{-1} < C_I < 60 \mu\text{m}^{-1}$ . The experimental values, found from the previous analysis range from  $10\sim 35 \mu\text{m}^{-1}$  (since  $R_{NT-M} = (2G_0C_I)^{-1}$ ), hence

in surprisingly good agreement with this very simple estimate. The second term in Eq. (5.9) is due to scattering along the nanotube with a mean free path  $L_0$  discussed above, and the third term represents the quantization of conductance in 1D systems.

The nanotube-metal conductances found here are in line with the contact transmission coefficients calculated by Anantram *et al.* for SWNTs (Anantram, 2000). It is shown that the transmission coefficient increases linearly with contact area of various types of nanotubes with metals, hence in agreement with the semi-classical model used here and the analysis.

The nanotube-fiber contact is more complex. It consists of a series of nanotube-nanotube contacts. In the model, an electron scatters isotropically at the junctions between nanotubes. Considering an infinite series of such junctions (as an approximation to the real nanotube-fiber contact) then the transmission probability from the nanotube to the fiber  $T_{NT-F} \sim 0.7$  (Berger, 2002). On the other hand, crossed nanotubes have been studied and the transconductance from metallic to metallic singlewalled nanotubes have been determined (Fuhrer, 2000). The probability that an electron on one tube tunnels from to the next is found to be about  $T = 0.06$  (Fuhrer, 2000). Using this value, we find for an array of these junctions that  $T_{NT-F} = 0.3$  (Berger, 2002). Therefore,  $0.3 < T_{NT-F} < 0.7$ .

If we assume that two channels contribute to the transport in the nanotubes, then from the empirical values  $0.5 G_0 < G < G_0$ , we conclude that  $T$  is a distribution with  $0.25 < T_{NT-F} < 0.5$  which peaks at  $T_{NT-F} \sim 0.5$ . This may explain the origin of the missing quantum in terms of the transmission coefficient into the fiber.

#### 5.4 Scattering from defects and contaminants

Scattering on the nanotubes, from static scattering sites (defects and surface contaminants), are proven to increase the resistance. As shown by Chico *et al.*, a defect (such as vacancies) in an (n,n) nanotube reduces the conductance (Chico, 1996): a vacancy on a 10 nm diameter tube reduces the conductance by about  $\Delta G = 0.15 G_0$  (for a 1.4 nm diameter SWNT the reduction is about  $1 G_0$ ). Consequently, if a nanotube with a defect is contacted with a liquid metal electrode, then the conductance should make an upward step of  $\Delta G$  when the defect becomes submerged in the liquid metal (thereby shorting out its effect). These relatively large steps are readily visible in conductance traces of contaminated tubes shown in Figure 4.2(a-b), but they are seldom seen on clean tubes. More specifically, since the plateaus of conditioned tubes are smooth indicates that they are essentially free of point defects over extended lengths (order of  $\mu\text{m}$ ).

The relatively high frequency with which  $G \sim 0.5 G_0$  plateaus are observed (shown in Figure 4.2) deserves special note and in particular that these plateaus often evolve to stable plateaus with  $G \sim 1 G_0$  during the execution of the experiment. Conductance jumps of a factor of about 2 have been observed in the TEM and they were correlated with significant changes in the contact to the fiber. In particular, a pseudo-contact, i.e. a graphitic flake on the tube, essentially reduces the transmission by a factor of 2 (Datta, 1995). Hence it is likely that these reduced plateaus are due to pseudo-contacts.

Surfactants dramatically affect the transport behavior. Figure 4.3 shows a conductance step and its associated resistance step. Note the absence of a flat plateau. Rather the resistance changes uniformly with  $x$  and with a slope that corresponds to  $\rho =$

2.2 k $\Omega/\mu\text{m}$ . (The metal-nanotube contact resistance is 500  $\Omega\cdot\mu\text{m}$  for this step). The  $\rho$  value is at least an order of magnitude greater than observed for clean tubes. Contrary to clean tubes, the resistance is not linear with  $l/x$  (inset of Figure 4.3b), which indicates that the shape of the conductance is not determined only by the contact conductance. Note also that (as for clean MWNTs) the plateau is smooth, and that there is no evidence for abrupt steps that would result from strong scattering centers (as for the tubes contaminated with particles). These results demonstrate that surfactants greatly increase the resistance of the nanotube. The current-voltage characteristics are also strongly affected as discussed below.

Currents typically greater than 1 mA destroy the tubes as shown in Figure 4.9. Defect-free-gold-contacted nanotubes tend to shed their outer layer or layers over their entire length shown in Figure 4.9 (e-f) (Frank, 1998). The contact is disrupted at the liquid metal-nanotube contact.

This observation (also see Reference (Cumings, 2000)) confirms that only the outer layer (or layers) participates to the transport even at high current densities. It has also been concluded by others (Cumings, 2000; Schonenberger, 1999). The number of layers involved at higher current densities (high bias voltages) is not known but it is very likely that only the top conducting layers are involved. Because it is known that on average only one in three layers is conducting, it is expected that only one in three conducting nanotubes have two conducting top layers and one in nine have three conducting top layers and so forth. Hence in a majority of the cases, it is likely that only one layer is involved, even for high currents.

From *in-situ* microscopy experiments, shown in Figure 4.9, we observed that (1) defect-free nanotubes tend to break at the contact point with the liquid metal, rather than at the nanotube-fiber contact, or in the middle of the nanotube, which would be the hottest point if it was a diffusive and dissipative conductor (Collins, 2001). (2) tubes that are coated with particles tend to break near the locations of these particles; (3) kinked nanotubes break at the kink. These experiments are consistent with the conclusion that dissipation occurs at defects and at contaminants.

### 5.5 Conductance versus voltage

Saturation of the conductance occurs only with poor NT-Hg contact (discussed below). With good/large NT-Hg contact, the current saturation effect observed in gold contacted SWNTs (Yao, 2000), which would result in a  $I/V$  decrease in the conductance, is not observed. They found the maximum of 25  $\mu\text{A}$  measured. For SWNTs the saturation effect is attributed to back-scattering from longitudinal phonons however apparently this does not occur in freely suspended MWNTs. We have never observed the monotonic decrease in the conductance reported by Collins *et al.* (Collins, 2001; Collins, 2002), and not even for surfactant coated tubes.

The linear rise in  $G$  with increasing  $V$  is most likely related to the increase in the density of states with increasing  $V$  which also increases linearly with increasing energy as shown in Figure 2.9 (calculated by de Heer (Berger, 2002)). However, for low resistance contacts the increase in conductance is related to the number of accessible channels  $N$ , which is the number of 1D subbands that fall within  $\pm 1/2 V_{bias}$  of the Fermi level (Datta, 1995). The conductance  $G$  is given by the Landauer equation (Eq. (2.6)). Figure 2.9

shows  $G(V)$  assuming the ideal case where  $T = 1$  for all channels. In that model, for a 13.6 nm diameter nanotube, we expect that the conductance increase is  $dG/dV = 12 G_0/V$  in Figure 2.9 (Berger, 2002). However, the observed increase is much less:  $dG/dV \approx 0.3\sim 0.5 G_0/V$ . This implies that  $T \approx 0.02\sim 0.03$  for all of the semiconducting subbands, while, as shown below,  $T \sim 0.5$  for the conducting subbands. The reduced transmission for the semiconducting subbands compared with the conducting subbands are in line with their predicted (White, 1998; Ando, 1998) and observed (McEuen, 1999) properties as discussed above.

The strongly reduced transmission of the semiconducting bands reflects the scattering along the tube combined with the contact impedance (possibly due to Schottky barriers). If the former dominates, then the mean free path for the semiconducting subbands is  $L_0 = 0.02 L$ , where  $L$  is the nanotube length from contact to contact (from TEM studies  $L$  is found to be of the order of  $5\sim 10 \mu\text{m}$ ), so that the mean free path  $L_0 \approx 100\sim 200 \text{ nm}$ . Note that this value is in fact close to the mean free paths found in by Schonberger *et al.* (Schonberger, 1999). In this case, this indicates the participation of the semiconducting bands to the transport as in fact has been found to be the case in other work (Schonberger, 1999; Buitelaar, 2002). Anantram investigated nanotube transport as a function of bias and found reduced transmission coefficients for the semiconducting subbands compared to the metallic subbands (Anantram, 2000), which correspond to the experimental values.

Alternatively, it may be assumed that for high bias tunneling from the contacts to deeper conducting layers occurs so that those layers participate in the transport. This picture is however contradicted by the pattern of destruction at high bias, where a

uniform layer is removed from the entire length of the nanotube, which appears to imply that only the top layer participates. Moreover, the next conducting layer is statistically most probably separated by two or more semiconducting layers (i.e. by about 1 nm), which is rather large (Mintmire, 1995; Saito, 1992; Hamada, 1992). Also, the number of the semiconducting spacer layers varies from one MWNT to the next in contrast to the  $G(V)$  behavior which we found is quite uniform from one tube to the next. For these reasons we believe that the characteristic linear rise in conductance is only due to the participation of the semiconducting subbands of the outer conducting layer, and that these semiconducting subbands have small transmission coefficients (see Eq. (5.5)).

*In-situ* TEM experiments have shown several examples where a nanotube is contacted on both sides, however applied voltages up to 10 V, which is much greater than the band gap, do not produce a measurable current (that means,  $R \gg 1M\Omega$ ). These are clearly semiconducting nanotubes. However, it is curious that such high potentials still do not produce a significant current, for example, tunneling into deeper conducting layers or into the states above the gap should contribute to the transport. Since this does not occur, it implies that the semiconducting tubes are good insulators with high dielectric strengths.

Surfactant coated tubes show very different  $G(V)$  behavior shown in Figure 4.5. In contrast to clean tubes there is no extended linear region and  $G$  saturates at  $V = -1.5$  V. For instance a large offset of 0.3 V in the symmetry axis of  $G(V)$  is observed in Figure 4.5. All these features are in sharp contrast to clean tubes shown in Figure 4.4. The asymmetry may indicate significant doping caused by the surfactant, causing a shift of the Fermi level. From this observation we speculate that the doping (Schonenberger, 1999; Schonenberger, 2002) and the water sensitivity (Buitelaar, 2002) observed in

processed MWNTs are not an intrinsic but are directly related to the surfactants that have been applied to the nanotubes (Bonard, 1997), and also to the difference in work function between the nanotubes and the contact.

It is interesting to point out that statistically, for 1 in 3 conducting tubes, the second layer is also metallic. It would be expected that these tubes would have remarkably different non-linear properties at higher bias voltages as well as greater low bias conductances (i.e.  $2 G_0$  rather than  $1 G_0$ ). This is not seen; all clean conducting tubes with large NT-Hg contact behave much alike with a nearly perfect linear increase of the conductance and  $G \sim 1 G_0$ . It may well be that those tubes for which the top two layers are metallic are in fact very poor (diffusive) conductors due to interlayer scattering. Scattering of this kind has been described by Roche *et al.* (Roche, 2001, Appl. Phys. Lett.; Roche, 2001, Phys. Rev. B.) This implies that those nanotubes that exhibit  $\sim 1 G_0$  conductances, the top layer is always metallic and the next layer is always semi-conducting. This immediately explains the great uniformity in properties of all of the conducting MWNTs and their similarity to SWNTs.

In summary, it appears that only the conducting subbands of the outer layer participate to transport. The higher subbands have short mean free paths (McEuen, 1999) and/or higher contact resistances, which limits their participation to the transport. Among other things, this explains the uniformity in the MWNT transport properties: the number of metallic subbands is the same for all nanotubes. Surfactants cause doping and reduced transmission.

## 5.6 *In-situ* measurements with variable contacts

We found that the intrinsic resistance of MWNTs is very small: in particular, for a nanotube of length  $L$ , the typical intrinsic resistance per unit length,  $R/L < 100 \text{ } \Omega/\mu\text{m}$ . The intrinsic resistance of a typical MWNT of a few micron long is much smaller than  $1/G_0$ , shows that it is a ballistic conductor. The typical mercury to nanotube contact resistance  $R^*_{NT-M}$  is in the range 0.1-1  $\text{k}\Omega\cdot\mu\text{m}$ . Because of the low intrinsic resistance of the clean suspended MWNT, we expect the conductance of tubes making a small contact with liquid metal to be mostly determined by the contact contribution. Therefore, the geometry of the contact and the dipping length on a small scale will be determining.

The  $G(V)$  properties for Hg-nanotube contacts show variations that are due to the contacts and not due to the properties of the nanotubes themselves. This is clear from variations in  $G(V)$  when only the contact geometry is changed (Figure 4.6 and 4.7). First the value of the conductance at low bias voltage increases with increasing contact area, and in accordance with calculation of SWNTs in contact with a metal along its circumference (Anantram, 2000; Mingo, 2000). The same is observed for HOPG (Figure 4.13). There are several cases where  $G(V)$  curves for the same nanotube intercept each other, which can only be explained in terms of the contact properties, which appear to affect not only the  $G(V=0)$  but also to some degree, the slopes  $dG/dV$ . This appears most clearly when  $G(V=0) \ll 1 G_0$ , i.e. when the measured two point conductance is most probably dominated by the contact contribution. Hence, the contacts can not be characterized only by the contact area since then it is difficult to understand how two curves can intercept. In fact we have observed that  $G(V)$  for nanotubes that appear to rest on the surface tend to exhibit a maximum near  $V = 2 \text{ V}$ , while nanotubes that penetrate

the surface, tend not to exhibit a maximum, suggesting that details of the contact to the Hg affect the shape of  $G(V)$ . This property is reminiscent of the differences in the electronic tunneling properties into nanotubes according to whether the tube is end-contacted or side-contacted (Palacios, 2003). A poorer contact is predicted for nanotubes end contacted to Al since the  $\pi$  states preferentially couple to the metal states, as found also for the cylindrical contact geometry (Mingo, 2000), whereas both  $\pi$  and  $\pi^*$  states couple equivalently for side contacts. It is worth noting that the two  $\pi$  and  $\pi^*$  channels in this case don't mix at low bias, which is consistent with ballistic transport (see also Ref. (Anantram, 2000)).

### 5.7 Non-conducting MWNTs

We have observed highly resistive MWNTs ( $\leq 10^{-3} G_0$ ). Note that these resistance values could not be ascribed to diffusive scattering in a conducting tube, for this would require resistance at least of  $2 \text{ M}\Omega/\mu\text{m}$ , that is more than 2 orders of magnitude higher than diffusive MWNTs (Bachtold, 2000). Some of these tubes can hold off bias voltages  $> 2 \text{ V}$  and even up to  $8 \text{ V}$ , which is in any case very much greater than the gap. This suggests that there is a Schottky barrier at the semiconducting nanotube-Hg interface (Nakanishi, 2002) (the work function of Hg is  $4.48 \text{ eV}$  to be compared to an estimated  $4.7 \text{ eV}$  for a SWNT (Cui, 2003)). When a non-conducting nanotube breaks down at high voltages, then the failure occurs at the nanotube-metal contact. It is reasonable to assume that the breakdown of the metal-nanotube Schottky barrier initiates the failure. This is probably initiated by a tunneling current that causes local heating, which in turn produces thermionic electron emission (Javey, 2003). The current is enhanced, ultimately

destroying the nanotube. In any case, non-conducting multiwalled nanotubes are remarkably good insulators, even though  $k_B T$  is of the same order as the energy gap.

### 5.8 *In-situ* observations of nanotube failure

The failure modes of MWNTs shed light on the heat dissipation processes. Undamaged nanotubes tend to fail at the Hg contact, suggesting that most of the heat is dissipated there. Nanotubes with defects tend to fail at the defect. Curiously, we have not observed nanotubes to fail at the contact with the fiber. This contact can be considered to be composed of multiple nanotube-nanotube contacts. In our previous publication (Poncharal, 2002) we argued that the transmission coefficient of this contact was probably about  $1/2$  which explains the “missing” quantum, that is why we observe that well contacted MWNTs have 1 quantum of conductance rather than 2, as expected from the band structure. On the other hand, this explanation could imply that more heat is dissipated at the fiber contact than at the metal contact, since the transmission coefficient of the metal contact would then be 1 and  $1/2$  for the fiber contact. Hence,  $2/3$  of the power  $W = I^2 R$  would be dissipated in the fiber contact and  $1/3$  in the Hg contact. On the other hand, if the reduced transmission at the fiber contact is caused by elastic processes, then this argument does not hold, in fact the heat may be distributed far from the contact point of the nanotube with the fiber. Also, the contact nanotube-fiber can be viewed as a multiple contact so that the power is dissipated over a distance along the tube.

## 5.9 Hg bubble formation

The formation of Hg bubbles is one of the most intriguing effects that we have observed in these experiments. It occurs when the contact of the nanotube is relatively small under high current conditions and only when the nanotube is negatively biased with respect to the Hg. Once the bubble formed, the size of it above the Hg surface can be varied continuously by adjusting the bias voltage. The asymmetry with respect to bias is very important and indicates that the direction of the current matters. However, as seen in Figure 4.12, there is no asymmetry in  $G(V)$  of the tube making contact. Therefore we believe the phenomenon is related to an unusual heating effect. Apparently, when electrons are injected into the Hg, then the temperature near the nanotube increases enough to locally vaporize the Hg. In contrast, when the electrons flow into the nanotube, this does not happen. This scenario is consistent with ballistic transport, where the electrons are accelerated into the Hg due to the potential drop (which is of the order of  $V_{bias}$ ) at the nanotube-Hg interface. These electrons rapidly dissipate their energy in the metal causing local heating. When the bias is reversed, the electrons are accelerated as they enter the nanotube due to the potential drop at the interface. If the mean free path is larger than the nanotube length (as in ballistic transport) then no energy is dissipated in the nanotube, and it will not heat up. Hence, an asymmetry in the heat dissipation (but not in  $G(V)$ ) is expected in ballistic transport.

On the other hand, nanotube failure is observed at the Hg interface for both positive and negative bias. It may be that failure is not only due to heating but also due to electromigration and electrical breakdown effects, due to the large electric fields (of the

order of  $V_{bias}/D$ , where  $D$  is the contact interface thickness and it is of atomic dimensions).

#### 5.10 Experiments with a small Hg droplet touching an HOPG surface

The  $G(V)$  properties of HOPG and conducting MWTNs are remarkably similar. In fact,  $G(V)$  on HOPG has been previously measured by Agrait *et al.* using a tungsten STM tip in contact with HOPG (Agrait, 1992). They also found an increase in the conductance with increasing  $V_{bias}$ . The increase in the conductivity in that case has been ascribed to the linearly increase in the density of states with increasing and decreasing applied voltage. We have also concluded that the increased conductance in MWNTs is due to the increased density of above and below the Fermi level (Poncharal, 2002). Moreover it is likely that for graphite the contact conductance is essentially determined by the top layer, since the c axis resistivity is about five orders of magnitude higher ( $\sim 10 \Omega \cdot \text{cm}$ ) than the basal plane resistivity ( $\sim 100 \mu\Omega \cdot \text{cm}$ ).

#### 5.11 Comparisons with theory and with other experiments

The basic electronic structure of SWNTs was theoretically predicted by Mintmire *et al.* (Mintmire, 1992) and later experimentally confirmed by Wildoer *et al.* (Wildoer, 1998) and Odom *et al.* (Odom, 1998). The theoretical prediction of ballistic conduction in carbon nanotubes over microns distances by White and Todorov (White, 1998) coincided with Frank *et al.*'s paper (Frank, 1998). They pointed out one dimensionality of the electronic structure and the virtual absence of back-scattering for the conducting subbands which, it was speculated, should lead to exceptionally long mean free paths.

This theme was later amplified by others and mainly addressed SWNTs (for a recent review, see (Yao, in Carbon Nanotubes; Dresselhaus, 2001)). MWNTs were treated by Roche (Roche, 2001) and others, who pointed out the importance on interlayer scattering in conductor/conductor double-walled nanotubes and the absence of scattering in conductor/semi-conductor conductor double-walled nanotubes. Recently Urbina *et al.* find that MWNTs have ballistic transport over a micron at room temperature (Urbina, 2003). Javey *et al.* find that SWNTs with Pd contact have conductance reaching four quantum units ( $4G_0$ ) at low temperature (Javey, 2004). Below we discuss a selected set of key experimental papers that directly address the question of ballistic conduction in MWNTs.

Earlier and some later nanotube measurements have a feature that the measured transport properties were diverse and difficult to rationalize: each MWNT appeared to have unique transport properties. For example, four-probe measurements by Ebbesen *et al.* on several lithographically contacted MWNTs showed a wide variety of properties, with both positive and negative temperature coefficients of the conductivity (Ebbesen, 1996). Resistivities varied greatly and even apparently negative resistivities were observed, where the voltage measured on the inner two contacts had a polarity, which was reversed from that of the outer contacts. The conclusion was drawn that currents in MWNTs follow complex serpentine paths that may even reverse direction. It was later accepted that the problem with these measurements was in the sample preparation. It should be pointed out that the measurements showed signs of poor contacts: the reversed voltage is more aptly explained in terms of a directional mesoscopic contact (Datta, 1995). However, the fact remains that these measurements on lithographically contacted

nanotubes yielded unreliable results, which should signal that great caution should be taken in applying similar methods to extract nanotube properties.

Measurements by Langer *et al.* on MWNT bundles showed  $\ln T$  dependence conductance (Langer, 1996), which saturates at low temperatures (the conductance increases by about a factor of 2 from 1 K to 80 K). Magnetoresistance measurements showed evidence for universal quantum fluctuations and weak localization. These measurements strongly supported that isolated MWNTs behave as disorder mesoscopic 2-D systems. Weak localization requires that elastic scattering dominates inelastic scattering, and phase coherence lengths greater than the elastic scattering lengths. Hence, these experiments provide evidence for elastic scattering in the tubes.

Measurements by Schonenberger *et al.* on individual MWNTs found closely related results (Schonenberger, 1999). The nanotubes were purified and ultrasonically dispersed in liquid using surfactants as described in Reference (Bonard, 1997). The conductance increased by a factor of about 2 when the temperature is increased from 1K to 80 K. Magneto-transport measurements also showed universal quantum fluctuations and weak localization. Observations of Aharonov-Bohm oscillations showed that only the outer layer participates in the transport (Bachtold, 1999). Moreover, from tunneling spectroscopy the electronic structure was confirmed to be similar to that of a SWNT however with the expected reduced energy scale (Schonenberger, 1999). They concluded that the transport in MWNTs is one dimensional, diffusive at room temperature and quasi-ballistic at low temperatures. Temperature independent elastic scattering-lengths  $L_e = 90-180$  nm were deduced. Furthermore, Hertel *et al.* are able to study the electron-phonon interaction in the metallic nanotubes only by probing electrons from the vicinity

of the Fermi level using femtosecond time-resolved photoemission (Hertel, 2000). They find that there is no clear signature for electron-phonon scattering up to  $T = 300$  K (Hertel, 2000). It was concluded that the conductivity increase with increasing  $T$  was not due to density of states (DOS) effects. Note that the DOS increases sharply above the gap, which should cause a very large conductivity increase with increasing temperature (which is not observed). The length dependence of the resistance was estimated to be (by comparing different nanotube samples with different lengths) about  $4 \text{ k}\Omega/\mu\text{m}$ .

More recently, Buitelaar *et al.* observed quantum dot properties in MWNTs (Buitelaar, 2002), similar to those observed in SWNTs (Tans, 1997). It was concluded that the outer layer was disordered with substantial hole-doping and that the next layer was metallic to produce the observed properties which were clearly associated with 2 conducting channels from the deeper layer. Coherent transport was assumed (at sub 1 K temperatures) over the entire tube length of  $2.3 \mu\text{m}$ . Substantial hole doping has also been concluded by that group in other work (Kruger, 2001) so that up to 10-20 1D modes of the outer layer participate in the transport, but that charge transport to the contacts is determined by only one mode (Schonenberger, 2002). The doping has been identified to be related to water (Schonenberger, 2002). It is also significant that the two point conductances of their MWNTs do not exhibit the increase with increasing voltage (Nussbaumer, 2002) that we observe, and that these tubes also exhibit the failure behavior found at high voltage by Collins *et al.* (Collins, 2002).

Liu, Avouris *et al.* report on the transport properties of two 1% boron doped lithographically contacted MWNTs, which causes a lowering of the Fermi level  $\Delta E_F \leq -0.1 \text{ eV}$  (Liu, 2001). They estimate that 4 and 6 subbands (for the two samples

respectively) participate to the transport: The two point 300 K conductance is found to be  $G = 2.24 G_0$  and  $G = 2.84 G_0$ . In contrast to others, their samples do not show a decrease but rather a slight linear increase of the relative resistance  $R/R_{300K}$  with increasing the temperature from about 100 to 300 K (both in 2 point and in 4 point measurements). However, the increase is extremely small: about  $1 \cdot 10^{-4} /K$  (a factor of 400 less than for copper). The resistance increase is presented as evidence for metallic conduction. 1D weak localization is concluded from magnetoresistance measurements. The elastic mean free path is found to be  $L_{elastic} = 220-250$  nm which is consistent with scattering only at the contacts. It is estimated that 4-6 channels participate to the transport in these doped nanotubes. The electron-phonon relaxation time at room temperature is estimated to be  $\tau = 0.4$  ps (which, with a Fermi velocity of  $10^8$  cm/sec corresponds to a mean free path of 400 nm). Coherence lengths are found to be temperature dependent and longer than the intercontact distance (250 nm) at low temperatures. One of the conclusions of this paper is that the mean free paths are very long despite the rather heavy boron doping. In many respects this work appears to confirm ballistic conduction (at least on the 400 nm length scale), even in the very unfavorable condition of heavy doping, however the paper actually classifies the nanotubes to be in the diffusive regime. The very weak increase in the resistance is all the more important since it implies that the thermally activated subbands apparently do not significantly contribute to the conductivity with increasing T: it shows that there is no large change in the number of participating layers as the temperature is increased. This appears to be consistent with the relatively small, observed increase of the conductivity at high bias voltages mentioned above.

Collins and Avouris *et al.* find complex conduction behavior for lithographically contacted MWNTs (Collins, 2001; Collins, 2002). The nanotubes were applied to prepatterned Au electrodes, after dispersing them in dichloroethane, centrifugation and a thermal treatment. The transport properties were interpreted in terms of the interplay of the contributions from multiple semiconducting and metallic layers where up to 8 layers contribute to the transport in the high current (non-linear transport) regime (Collins, 2001). In later work, the authors conclude that many shells participate to the transport even at low bias (Collins, 2002). They observe that the conductance monotonically decreases with increasing voltage. The in-air breakdown occurs at relatively low power (320  $\mu$ W), and proceeds in steps of 12  $\mu$ A; the tubes ultimately fail in the middle (Collins, 2001). The two point low bias conductance is 3.7  $G_0$  for a 200 nm long tube.

Urbina *et al.* perform transport measurements using a scanning-tunneling probe on a arc-produced MWNT sample prepared by spin coating the solution (of MWNTs in Aroclor 1254, a mixture of polychlorinated biphenyls) on gold substrate. They find that ballistic transport at room temperature along the carbon nanotube over distance than 1.4  $\mu$ m. And the conductance appears to be quantized, regardless of the diameter and length of the nanotubes involved (Urbina, 2003).

Javey *et al.* pattern CVD growth SWNTs on SiO<sub>2</sub>/Si wafer, followed by electron beam lithography, metal deposition, and lift-off to form Pd contacts. They find the conductance of CVD growth SWNTs with Pd ohmic contact reach 4  $G_0$  at low temperature (Javey, 2004).

We always observe a linear increase in the conductance, never a decrease; we do not observe (low bias) conductances greater than 1  $G_0$  nor do we observe the breakdown

in steps. Furthermore, our nanotubes (with contacts) can sustain powers up to about 5 mW, and their breakdown pattern involves only the outer layer(s); failure occurs at the contact and not in the middle of the tube. We must conclude that our nanotubes and those investigated by Collins *et al.* (Collins, 2001) must be essentially different objects and the most significant difference is in the processing (most likely due to oxidation damage caused in the thermal annealing step), since Collins *et al.* used nanotubes produced by de Heer in some of these studies (Collins, 2001).

In measurements that in principle are most closely related to those presented here, Bachtold *et al.* measured the voltage drop along MWNTs and SWNT bundles using scanning electrostatic force microscopy of lithographically contacted nanotubes (Bachtold, 2000). From their observations, the voltage drop along current carrying nanotubes was determined, from which the resistance per unit length was deduced. They found that the room-temperature resistance of MWNTs is  $\rho = 10 \text{ k}\Omega/\mu\text{m}$ , while  $\rho < 1.5 \text{ k}\Omega/\mu\text{m}$  was found for the SWNT bundle (although inspection of their data appears to show that a significant voltage drop along at least 50% of the 2  $\mu\text{m}$  long bundle). They concluded that SWNTs are ballistic conductors (from the Landauer equation, assuming that the SWNT bundle contained one conducting nanotube with 2 channels, and that the voltage drop occurred at the contacts) and MWNTs are diffusive conductors. The conclusion was based on the ballistic conduction criterion applied to a (hypothetical) 1  $\mu\text{m}$  long nanotube (Eq. (5.6)).

Ballistic conduction has recently been observed in SWNTs (Liang, 2001; Kong, 2001; Javey, 2003) from quantum oscillations in a Fabry-Perrot experiment implying long elastic lengths and phase coherence lengths (at least the intercontact spacing, 200

nm). These experiments show that (phase coherent) ballistic conduction at 10 K does in fact occur. Room-temperature two-probe resistances as low as 7 k $\Omega$  have been measured suggesting low scattering at room temperature as well. It is relevant that the SWNTs in this experiment were produced in situ and not chemically or mechanically treated.

The reasons for these discrepancies between the various nanotube measurements needs be clarified. There is very strong evidence that processing indeed alters the properties (Lu, 1996) in particular of the surface layers (Buitelaar, 2002). Surfactants are universally used to suspend nanotubes in liquids in order to deposit them on substrates. Surfactants chemically bind to the surfaces and may be very hard to remove; in order to remove them may require a high temperature ‘annealing’ treatment (Dujardin, 1998), which can cause further damage them (Eklund, 2001). We have directly demonstrated that surfactants greatly increase the resistivities and affect the doping levels. In fact we find that the resistivities of surfactant treated MWNTs are of the order of magnitude observed by others (Schonenberger, 1999). Clearly water sensitivity (Schonenberger, 2002) may be explained as a result of the hydrophilic surfactant layer on the nanotubes.

Ultrasound has been found to damage nanotubes (Lu, 1996). Ultrasonic dispersion of the nanotubes is also universally applied to MWNTs in order suspend them and to separate them from the nanotube fiber bundles.

Thermal treatments are used to open the nanotubes by oxidizing the ends. However, very similar treatments are used to burn away graphitic particles and amorphous carbonaceous material and also to anneal the tubes. This purification method clearly can be detrimental to the transport properties and may partly explain the properties observed in References (Collins, 2002; Collins, 2001).

## CHAPTER 6

### SUMMARY AND CONCLUSION

The experiment results and analysis of the properties of freely suspended unprocessed nanotubes contacted with a liquid metal contact in this thesis not only confirms that the conductance of MWNTs is quantized, but also demonstrate that MWNTs are indeed ballistic conductors at room temperature over many microns. Ballistic is meant in the sense that the momentum scattering lengths (see chapter 2) are much longer than the nanotube length, hence that the resistance is essentially independent of the length (Datta, 1995; Landauer, 1989; Bachtold, 2000).

The conductance measurements of MWNTs have shown several uniform, robust and reproducible properties:

- (1) Rounded conductance steps followed by plateaus are always seen.
- (2) Initial plateau conductances are distributed primarily in the narrow range from  $G_{pl} = 0.5 \sim 1 G_0$ .
- (3) Initial plateaus significantly greater than  $1 G_0$  are not observed.
- (4) The great majority of the plateaus are remarkably flat, without small substeps or slopes.
- (5) The conductance is independent of voltage up to about 0.1 V followed by a linear increase with increasing voltage.
- (6) Destruction occurs at current of the order of  $\leq 1$  mA and failure occurs at the nanotube-metal contact.
- (7) The properties of conducting nanotubes are very uniform.

The obvious reason for the uniformity in the properties is given by the theoretical prediction that (for  $V_{bias} < E_{gap}$  and  $kT < E_{gap}$ ) only two conducting subbands contribute to the transport for conducting nanotubes. These conditions are amply met for the nanotubes in this study at room temperature and for  $V_{bias} < 100$  mV. The linear increase in conductivity at high bias is also clearly explained in terms of participation from higher subbands with reduced transmission coefficients. In 2/3 of the cases, the layer below the top layer is semiconducting and hence is not expected to participate to the transport, in line with experiments that show that only the top layer participates. Hence, the most straightforward explanation for all these effects is that the two conducting subbands of the outermost conducting layer dominate transport at low bias and at room temperature. As pointed out, our data at low bias strongly disagree with interpretations that attribute the high conductances to the participation of many highly resistive conducting subbands. Moreover, high doping levels are not indicated in particular by the very small range in the measured conductance values: doping concentrations are bound to vary and the resistances are expected to be diameter dependent. There is no indication for these dependences.

The analysis of the conductance trace shapes shows that the nanotube-metal contact resistances dominate the shape. This contact conductance per unit length is rather small:  $G^* \sim 50 G_0/\mu\text{m}$  (a contact 100 nm in length has a resistance of about 2 k $\Omega$ ). The nanotube-metal contact conductances are consistent with other measurements, with recent calculations (Anantram, 2000) and with Sharvin's semi-classical expression for contact conductances of small contacts (Sharvin, 1965).

The nanotube-fiber contact appears to have a transmission coefficient  $T = 0.5$ , which compares well with the expected limits from  $T = 0.3$  (derived from SWNT junctions) to  $T = 0.7$  (the theoretical maximum). Hence, the ‘missing quantum of conductance’ may be caused by reflections at the nanotube-fiber contact. Variations in the plateau conductance have been shown to be caused by variations in that contact. The relatively high frequency of  $T \sim 0.5 G_0$  may be due to a scattering at a pseudo-contact, i.e. a graphitic flake on the tube which essentially reduces the transmission by a factor of 2 (Datta, 1995). Another possibility is related to nanotube-metal contact. Due to two metallic bands coupled very differently to the electrode, one of them is missing for transport, which results in reduced conductance (Palacios, 2003).

The slopes of the conductance plateaus are related to the contact resistance and to the resistance per unit length of the tube. The resistance per unit length is found to be  $\rho < 50 \Omega / \mu\text{m}$ . Combined with the conclusion that two subbands participate in the transport, implies that  $L_m > 200 \mu\text{m}$ , following the identical reasoning presented by McEuen and co-workers (Bachtold, 2000). Hence MWNTs are certainly ballistic conductors at room temperature.

Elastic scattering lengths (from static scattering sites) of the order of hundreds of nm (as estimated for the elastic mean free paths by others (Schonenberger, 1999)), should have produced observable steps in the conductance plateaus which are not seen. Hence either there are no defects on the cleaned tubes or they have a negligible effect on the resistance. Surfactant-coated tubes show the resistances of the order of  $2 \text{ k}\Omega/\mu\text{m}$ . The anomalous  $G(V)$  behavior of surfactant-coated tubes further indicate doping. Hence surfactant-coated tubes are doped with reduced mean free paths compared with clean

tubes. These observations are consistent with other measurements, which show an increased number of conducting channels, short mean free paths and evidence for doping (Schonenberger, 2002; Buitelaar, 2002).

The conductance-versus-voltage measurements of freely suspended nanotubes universally show a rise with increasing voltage, even for surfactant-coated tubes. For clean tubes the slope is tube dependent. The increase is clearly explained in terms of the participation of the semiconducting subbands at high bias however with reduced transmission coefficients. The nanotubes can sustain high currents of order of mA. In-situ TEM experiments verified the conductivity properties of nanotubes. They further show that dissipation occurs at defects and contaminants, and failure occurs at the contacts. At high current densities, the outer layer is destroyed showing that only the outer layer conducts as was concluded earlier (Frank, 1998; Poncharal, 1999; Schonenberger, 1999; Bachtold, 1999).

We have compiled a wide range of observations of metal contacted nanotubes in order to provide an overview for several of the processes that are involved. High contact resistances are observed when the contact area is small, which also affect the  $G(V)$  behavior.

For all conducting nanotubes we find that  $G(V)$  increases with increasing bias voltage:  $dG/dV_{bias} \sim 0.3 G_0/V$  for  $V_{bias} < 2$  V. In some cases (apparently when the nanotube ‘floats’ on the Hg),  $G(V)$  maximizes and then decreases; in other cases (apparently when the nanotube submerges), then  $G(V)$  does not maximize.

An increase in the conductance with increasing  $V_{bias}$ , is observed in both Hg-nanotube contacts and also in Hg-HOPG contacts. This strongly indicates that the density

of states dominates  $G(V)$ . The maximization of  $G(V)$  mentioned above probably is due to kinematic effects related to electron injection at the contact.

Conducting nanotubes fail for  $V_{bias}$  in the range 2.5 ~ 4 V. Failure typically occurs at the Hg contact or at defects, but not at the fiber contact. This property is consistent with ballistic transport through the nanotube, where all the dissipation and the voltage drop occur at the contact.

Highly resistive nanotubes can stand off voltages of more than 2 V, and they eventually fail at the Hg contact. These voltages are much greater than the expected typical band-gap (order of 0.1 eV). From the failure properties it appears that only the outer layer participates in the transport, consistent with previous measurements.

The formation of Hg bubbles for negatively biased nanotubes, indicates that hot electrons are injected into the Hg under those conditions, which cause local heating of the Hg at the interface. The absence of this effect for positively biased nanotubes is remarkable, and demonstrates an asymmetry in the heat dissipation (which is consistent with ballistic transport). On the other hand, we observe that  $G(V) \approx G(-V)$ . It is curious that no asymmetry is observed here as an indirect consequence of the heat dissipation asymmetry.

In contrast, the properties of processed, lithographically contacted are very different and vary from one experiment to the next. Due to this variety, a uniformly applicable summary of properties cannot be given, and the following properties are representative: (1) The nanotubes are diffusive conductors with low temperature mean free paths of the order of fraction of a micron. (2) The tubes are doped and the transport involves multiple (>2) channels (Schonenberger, 1999; Schonenberger, 2002). (3) In

some cases the transport is complex involving many layers (Collins, 2002), in other cases only the top two layers contribute of which the top layer is doped and the deeper layer shows ballistic properties (Buitelaar, 2002). (4) The conductance decreases with increasing voltage and the nanotubes fail due to thermal heating at relatively low currents (Collins, 2001).

This comparison clearly demonstrates that the lithographically contacted processed nanotubes are not the same objects as the unprocessed freely suspended nanotubes that we have investigated. We believe that processing damages, in particular, the outer layers of the nanotubes, which are the most important ones for electrical transport. Our experiments abundantly demonstrate the excellent and unique ballistic transport properties of the multiwalled nanotubes, which still are unrivaled in any other system. More importantly, we have demonstrated that these unique quantum properties persist under ambient conditions.

These measurements by Frank *et al.* (Frank, 1998) were the first one to demonstrate not only ballistic conductance in virgin carbon nanotubes under ambient conditions but also their 1D properties, their high current carrying abilities, and the fact that only the outer layer conducts. These properties were found at a time when there was no indication for any of them either from theory or from other experiments. These properties are in line with those expected theoretically for defect-free nanotubes, and also in line with more recently found properties of SWNTs.

A wide range of applications has been suggested since carbon nanotubes were discovered. A review of advances in their applications can be found in many articles (e.g. de Heer, 2004).

Thanks Joe Gezo, former undergraduate at GIT and currently being a graduate student at UIUC, for operating TEM.

## APPENDIX

### TIGHT-BINDING CALCULATION FOR $\pi$ ELECTRONS OF GRAPHENE

(Schönenberger, 2000)

Starting with the Bloch wavefunction

$$\Psi_{\vec{k}} = \sum_{\vec{R} \in G} e^{i\vec{k} \cdot \vec{R}} \phi(\vec{x} - \vec{R}) \quad (\text{A1})$$

Here,  $G$  is the set of lattice vectors.  $\phi(\vec{x})$  are the atomic wavefunctions, i.e. the  $p_z$  atomic orbitals of graphene. There are two such orbitals per unit-cells called  $\phi_1$  and  $\phi_2$ , where the index refers to the respective carbon atoms. Tight binding calculation assumes that the atomic wave-functions are well localized at the position of the atom. The total function  $\phi$  is linear combination of  $\phi_1$  and  $\phi_2$ :

$$\phi(\vec{x}) = B_1 \phi_1(\vec{x}) + B_2 \phi_2(\vec{x}) = \sum_n B_n \phi_n \quad (\text{A2})$$

The Hamiltonian for a single electron in the atomic potential given by all the carbon atoms:

$$H = \frac{\vec{p}^2}{2m} + \sum_{\vec{R} \in G} (V_{at}(\vec{x} - \vec{x}_1 - \vec{R}) + V_{at}(\vec{x} - \vec{x}_2 - \vec{R})) \quad (\text{A3})$$

Here  $\vec{x}_{1,2}$  denote the position of the two carbon atoms within the unit-cell.

$$H\phi_1 = \varepsilon_1 \phi_1 + \left( \sum_{\vec{R} \neq 0} (V_{at}(\vec{x} - \vec{x}_1 - \vec{R}) + V_{at}(\vec{x} - \vec{x}_2 - \vec{R})) + V_{at}(\vec{x} - \vec{x}_2) \right) \phi_1 \quad (\text{A4})$$

Here  $\varepsilon_1$  is the eigenvalue for the atomic  $p_z$  state. The second part to the right of this equation is abbreviated by  $\Delta U_1 \phi_1$ . This product is small because  $\Delta U_1$  is small in the vicinity of atom 1 and  $\phi_1$  is small everywhere away from location 1. Then we get,

$$H\phi_{1,2} = \varepsilon_{1,2} \phi_{1,2} + \Delta U_{1,2} \phi_{1,2} \quad (\text{A5})$$

Since  $\varepsilon_1 = \varepsilon_2$  and one can choose  $\varepsilon_{1,2} = 0$ , therefore

$$H\phi_1 = \Delta U_1\phi_1 \quad \text{and} \quad H\phi_2 = \Delta U_2\phi_2 \quad (\text{A6})$$

Next to solve the Schrödinger equation:

$$H\Psi_{\vec{k}} = E(\vec{k})\Psi_{\vec{k}} \quad (\text{A7})$$

And

$$E(\vec{k})\langle\phi_j|\Psi\rangle = \langle\phi_j|\Delta U_j|\Psi\rangle \quad (\text{A8})$$

Assume that only nearest-neighbor overlap integrals have to be taken into account. We obtain the two equations:

$$\begin{aligned} \langle\phi_1|\Psi\rangle &= B_1 + B_2\left(\int\phi_1^*\phi_2\right)(1 + e^{-i\vec{k}\cdot\vec{a}_1} + e^{-i\vec{k}\cdot\vec{a}_2}) \\ \langle\phi_2|\Psi\rangle &= B_2 + B_1\left(\int\phi_2^*\phi_1\right)(1 + e^{i\vec{k}\cdot\vec{a}_1} + e^{i\vec{k}\cdot\vec{a}_2}) \end{aligned} \quad (\text{A9})$$

Assume that the overlap integral is real, and only on-site and nearest-neighbor overlap integrals will be considered.:

$$\gamma_0 = \int\phi_1^*\phi_2 \in R \quad (\text{A10})$$

$$\gamma_1 = \int\phi_1^*\Delta U_1\phi_2 = \int\phi_2^*\Delta U_2\phi_1 \in R \quad (\text{A11})$$

The two integrals are equal because interchanging the indices should be not matter due to symmetry. Then we get the following two equations:

$$\begin{aligned} \langle\phi_1|\Delta U_1|\Psi\rangle &= B_2\gamma_1(1 + e^{-i\vec{k}\cdot\vec{a}_1} + e^{-i\vec{k}\cdot\vec{a}_2}) \\ \langle\phi_2|\Delta U_1|\Psi\rangle &= B_1\gamma_1(1 + e^{i\vec{k}\cdot\vec{a}_1} + e^{i\vec{k}\cdot\vec{a}_2}) \end{aligned} \quad (\text{A12})$$

Putting Eq.(A9), (A10), (A11) and (A12) together, and using the abbreviation

$$\alpha(\vec{k}) = (1 + e^{-i\vec{k}\cdot\vec{a}_1} + e^{-i\vec{k}\cdot\vec{a}_2}) \quad (\text{A13})$$

Then the eigenvalue problem is finally formulated as:

$$\begin{pmatrix} E(\vec{k}) & \alpha(\gamma_0 E(\vec{k}) - \gamma_1) \\ \alpha^* (\gamma_0 E(\vec{k}) - \gamma_1) E(\vec{k}) & \end{pmatrix} \begin{pmatrix} B_1 \\ B_2 \end{pmatrix} = \begin{pmatrix} 0 \\ 0 \end{pmatrix} \quad (\text{A14})$$

The dispersion relation  $E(\vec{k})$  is obtained from Eq.(A14) by putting the determinant to zero. Since  $\gamma_0$  is small, we could neglect it. Then one obtains (as an approximation) the simple dispersion relation

$$E(\vec{k}) = \pm \gamma_1 |\alpha(\vec{k})| \quad (\text{A15})$$

Substituting Eq.(13) into Eq.(15), one obtain:

$$E(\vec{k}) = \pm \gamma_1 \sqrt{3 + 2 \cos(\vec{k} \cdot \vec{a}_1) + 2 \cos(\vec{k} \cdot \vec{a}_2) + 2 \cos(\vec{k} \cdot (\vec{a}_2 - \vec{a}_1))} \quad (\text{A16})$$

Or,

$$E_{g_{2D}}(\vec{k}) = \pm \gamma_1 \sqrt{1 + 4 \cos\left(\frac{\sqrt{3}ak_y}{2}\right) \cos\left(\frac{ak_x}{2}\right) + 4 \cos^2\left(\frac{ak_x}{2}\right)} \quad (\text{A17})$$

Here,  $a$  is the lattice constant, i.e.  $a = \sqrt{3}a_0$ . The plot of this function is shown in Figure A2.

## REFERENCES

- Agrait, N.; Rodrigo, J. and Vieira, S. (1992). *Ultramicroscopy* **42**, 177.
- Anantram, M. P.; Datta, S. and Xue, Y. Q. (2000). *Phys. Rev. B* **61**, 14219.
- Anantram, M. P. (2000). *Phys. Rev. B* **62**, 4837.
- Ando, T.; Nakanishi, T. (1998). *J. Phys. Soc. Jpn.* **67**, 2857.
- Bachtold, A.; Fuhrer, M. S.; Plyasunov, S.; Forero, M.; Anderson, E.H.; Zettl, A. and McEuen, P. (2000). *Phys. Rev. Lett.* **84**, 6082.
- Bachtold, A.; Strunk, C.; Salvetat, J. P.; Bonard, J. M.; Forro, L.; Nussbaumer, T. and C., S. (1999). *Nature* **397**, 673.
- Beenakker, C. (1997). *Rev. Mod. Phys.* **69**, 731.
- Berger, C.; Yi, Y.; Wang, Z. L. and de Heer, W. A. (2002). Multiwalled carbon nanotubes are ballistic conductors at room temperature. *Appl. Phys. A* **74**, 363.
- Berger, C.; Yi, Y.; Gezo, J.; Poncharal, P. and de Heer, W.A. Contacts, non-linear transport effects and failure in multiwalled carbon nanotubes. (2003). *New J. of Phys* **5**, 73.1-73.16.
- Berger, C.; Poncharal, P.; Yi, Y. and de Heer, W.A. Ballistic Conduction in Multiwalled Carbon Nanotubes. (2003). *J. of Nanoscience and Nanotechnology*, Vol.3, No. 1-2, pp. 171-177.
- Bethune, D. S.; Kiang, C. H.; de Vries, M. S.; Gorman, G.; Savoy, R.; Vazquez, J. and Beyers, R. (1993). *Nature* **363**, 605.
- Bockrath, M.; Liang, W.; Bozovic, D.; Hafner, J.; Lieber, C.; Tinkham, M. and Park, H. (2001). *Science* **291**, 283.
- Bonard, J.-M.; Stora, T.; Salvetat, J.P.; Maier, F.; Stoeckli, T.; Duschl, C.; Forro, L.; de Heer, W. A. and Chatelain, A. (1997). *Advanced Materials* **9**, 827.
- Buitelaar, M. R.; Belzig, W.; Nussbaumer, T. *et al.* (2003). *Phys. Rev. Lett.* **91**, 057005.
- Buitelaar, M. R.; Bachtold, A.; Nussbaumer, T.; Iqbal, M. and Schonenberger, C. (2002). *Phys. Rev. Lett.* **88**, 156801.
- Charlier, J. C. and Lambin, P. (1998). *Phys. Rev. B* **57**, R15047.

- Chico, L.; Benedict, L. X.; Louie, S. G. and Cohen, M. L. (1996). Phys. Rev. B **54**, 2600.
- Collins, P. and Avouris, P. (2002). Appl.Phys. A **74**, 329.
- Collins, P.; Arnold, M. and Avouris, P. (2001). Science **292**, 706.
- Collins, P. G.; Hersam, M.; Arnold, M.; Martel, R. and Avouris, P. (2001). Phys. Rev. Lett. **86**, 3128.
- Crespi, V. H.; Chopra, N. G.; Cohen, M. L.; Zettl, A. and Louie, S. G. (1996). Phys. Rev. B **54**, 5927.
- Crespi, V. H.; Cohen, M. L. and Rubio, A. (1997). Phys. Rev. Lett. **79**, 2093.
- Cui, X.; Freitag, M.; Martel, R.; Brutus, L. and Avouris, P. (2003). Nanoletters **3**, 783.
- Cumings, J.; Collins, P. G. and Zettl, A. (2000). Nature **406**, 586.
- Dai, H.; Wong, E. W. and Lieber, C. M. (1996). Science **272**, 523.
- Datta, S. (1995). *Electronic transport properties in mesoscopic systems*. Cambridge University Press, Cambridge.
- De Heer, W.A. and Ugarte, D. (1997). in *Nanowires*, edited by P. Serena and N. Garcia (Kluwer, Netherlands,), p. 227.
- De Heer, W. A. and Ugarte, D. (1997). Z. Phys. D **104**, 469.
- De Heer, W. A. (unpublished).
- De Heer, W. A. (2004). MRS Bulletin. Nanotubes and the pursuit of applications.
- Dresselhaus, M. S.; Dresselhaus, G. and Avouris, P. (2001). *Carbon nanotubes: synthesis, structure, properties, and applications*. Springer, Berlin; New York.
- Dresselhaus, M. S.; Dresselhaus, G. and Saito, R. (1995). Physics of Carbon Nanotubes. Carbon **33**, 883.
- Dresselhaus, M. S.; Dresselhaus, G.; Sugihara, K.; Spain, I. L.; Goldberg, H. A. (1988). Graphite Fibers and Filaments. Springer Ser. Mater. Sci., Vol. 5 (Springer, Berlin, Heidelberg).
- Dujardin, E.; Ebbesen, T. W.; Krishnan, A. and Treacy, M. J. (1998). Adv. Mater. **10**, 611.
- Dujardin, E.; Ebbesen, T. W.; Krishnan, A. and Treacy, M. J. (1998). Adv. Mater. **10**, 1472.

- Dujardin, E.; Ebbesen, T. W.; Hiura, T. and Tanigaki, K. (1994). *Science* **265**, 1850.
- Ebbesen, T. W.; Lezec, H. J.; Hiura, H. *et al.* (1996). *Nature* **382**, 54-6.
- Ebbesen, T. W.; Lezec, H. J.; Hiura, H.; Bennett, J. W.; Ghaemi, H. F. and Thio, T. (1996). *Nature* **382**, 54.
- Ebbesen, T. W. and Ajayan, P. M. (1992). Large scale synthesis of carbon nanotubes. *Nature* **358**, 220.
- Eklund, P. (2001). Private communication.
- Elsholz, Frank. (2002). Landauer Büttiker Formalism.
- Endo, M. (1978). PhD thesis, Nagoya University, Japan, (in Japanese)
- Endo, M.; Takeuchi, K.; Kobori, K.; Takahashi, K.; Kroto, H. and Sarka, A. (1995). *Carbon* **33**, 873.
- Endo, M.; Takeuchi, K.; Igarashi, S.; Kobori, K.; Shiraishi, M. and Kroto, H. W. (1993). *J. Phys. Chem. Solids* **54**, 1841-1848.
- Fink, J. H. and Lambin, P. (2001). Dresselhaus, M. S.; Dresselhaus, G. and Avouris, P. (Eds.): *Carbon Nanotubes, Topics Appl. Phys.* **80**, 247-272. Springer-Verlag Berlin Heidelberg.
- Frank, S.; Poncharal, P.; Wang, Z. L. and de Heer, W. A. (1998). Carbon nanotube quantum resistors. *Science* **280**, 1744.
- Forró, L.; Salvetat, J. P.; Bonard, J. M.; Bacsá, R.; Thomson, N. H.; Garaj, S.; Thien-Nga, L.; Gaál, R.; Kulik, A. J.; Ruzicka, B.; Degiorgi, L.; Bachtold, A.; Schönenberger, C.; Pekker, S. and Hernadi, K. (1999). In *Science and Application of Nanotubes*, Tomáek, D.; Enbody, R. J. (Eds.) (Kluwer Academic/Plenum Publishers, New York) p. 297.
- Fuhrer, M.; Nygard, J.; Shih, L.; Forero, M.; Yoon, Y.; Mazzoni, M.; Choi, H.; Ihm, J.; Louie, S. Zettl, A. and McEuen, P. (2000). *Science* **288**, 494.
- Hamada, N.; Sawada, S.; Oshiyama, A. (1992). New one-dimensional conductors: Graphite microtubules. *Phys. Rev. Lett.* **68**, 1579.
- Hertel, T. and Moos, G. (2000). *Phys. Rev. Lett.* **84**, 5002.
- Hiura, H.; Ebbesen, T. W. and Tanigaki, K. (1995). *Adv. Mater.* **7**, 275.

- Hou, P. X.; Bai, S.; Yang, Q. H.; Lui, C. and Cheng, H. M. (2002). *Carbon* **40**, 81.
- Iijima, S. (1991). *Nature* 354, 56-58.
- Iijima, S.; Ichihashi, T. (1993). *Nature* 363, 603-605.
- Javey, A.; Guo, J.; Wang, Q. *et al.* (2003). *Nature* **424**, 654.
- Javey, A.; Guo, J.; Paulsson, M.; Wang, Q.; Mann, D.; Lundstrom, M. and Dai, H. (2004). *Phys. Rev. Lett.* 92, 106804.
- Kane, C. L. and Mele, E. J. (1997). *Phys. Rev. Lett.* 78, 1932.
- Kelly, B. T. (1981). *Physics of graphite*. Applied Science Publishers, London, New Jersey.
- Kong, J.; Yenilmez, D.; Kim, T.; Dai, W.; Laughlin, R.; Liu, L.; Jayanthi, C. and Wu, W. (2001). *Phys. Rev. Lett.* **87**, 106801.
- Kruger, M.; Buitelaar, M.; Nussbaumer, T. and Schonberger, C. (2001). *Appl. Phys. Lett.* **78**, 1291.
- Landauer, R. (1989). *J. Phys.: Condens. Matter* **1**, 8099.
- Langer, L.; Bayot, V.; Grivei, E.; Issi, J.-P.; Heremans, J. P.; Olk, C. H.; Stockman, L.; Haesendonck, C. V. and Bruynseraede, Y. (1996). *Phys. Rev. Lett.* **76**, 479.
- Liang, W.; Bockrath, M.; Bozovic, D.; Hafner, J.; Tinkham, M. and Park, H. (2001). *Nature* **411**, 665.
- Liu, K.; Avouris, P.; Martel, R. and Hsu, W. (2001). *Phys. Rev. B* **63**, 161404.
- Liu, J.; Rinzler, A. G.; Dai, H.; Hafner, J. H.; Bradley, R. K.; Boul, P. J.; Lu, A.; Iverson, T.; Shelimov, K.; Huffman, C. B.; Rodriguex-Macia, F.; Colbert, D. T. and Smalley, R. E. (1998). *Science* 280, 1253-1256.
- Lu, K.; Lago, R. and Chen, Y. (1996). *Carbon* **34**, 814.
- Martel, R.; Schmidt, T.; Shea, H. R.; Hertel, T. and Avouris P. (1998). *App. Phys. Lett.* **73**, 2447.
- McEuen, P.; Bockrath, M.; Cobden, C.; Yoon, Y. and Louie, S. (1999). *Phys. Rev. Lett* **83**, 5098.
- Mingo, N. and Han, J. (2000). *Phys. Rev. B* **64**, 201401.

- Mintmire, J. W. and White, C. T. (1995). Electronic and Structural Properties of Carbon Nanotubes Carbon **33**, 893.
- Mintmire, J. W.; Dunlap, B. I. and White, C. T. (1992). Are Fullerene Tubules Metallic?. Phys. Rev. Lett. **68**, 631.
- Nakanishi, T.; Bachtold, A. and Dekker, C. (2002). Phys. Rev. B **66**, 073307.
- Nussbaumer, T. (2002). Private Communication.
- Odom, T.; Huang, J. L.; Kim, P. and Lieber, C. M. (1998). Nature **391**, 62.
- Ogbazghi, A. Y.; de Heer, W. A.; First, P. N. to be published.
- Palacios, J.J.; Perez-Jimenez, A.J.; Louis, E.; SanFabian, E. and Verges, J.A. (2003). First-principles Phase-coherent Transport in Metallic Nanotubes with realistic contacts. Phys. Rev. Lett. **90**, 106801.
- Poncharal, P.; Wang, Z. L.; Ugarte, D. and De Heer, W. A. (1999). Science **283**, 1513.
- Poncharal, P.; Frank, S.; Wang, Z. L. and de Heer, W. A. (1999). Conductance quantization in multiwalled carbon nanotubes. Eur. Phys. J. D **9**, 77.
- Poncharal, P.; Berger, C.; Yi, Y.; Wang, Z.L. and de Heer, W.A. Room temperature ballistic conductance in carbon nanotubes. (2002). J. of Phys. Chem. B, vol. 106 (47), pp. 12104-12118.
- Roche, S.; Triozon, F. and Rubio, A. (2001). Appl. Phys. Lett. **79**, 3690.
- Roche, S.; Triozon, F.; Rubio, A.; Mayou, D. (2001). Phys. Rev. B **64**, 121401(R).
- Roschier, L.; Penttilä, J.; Martin, M.; Hakonen, P. and Paalanen, M. (1999). Appl. Phys. Lett. **75**, 728-730.
- Saito, R.; Fujita, M.; Dresselhaus, G.; Dresselhaus, M. S. (1992). Phys. Rev. B **46**, 1804.
- Saito, R.; Fujita, M.; Dresselhaus, G.; Dresselhaus, M. S. (1992). Electronic structure of chiral graphene tubules. Phys. Rev. Lett. **1992**, **60**, 2204.
- Saito, R.; Dresselhaus, G. and Dresselhaus, M.S. (1998). Physical properties of carbon nanotubes. Imperial College Press, London.
- Schonenberger, C. (2000). Bandstructure of Graphene and Carbon nanotubes: An Exercise in Condensed Matter Physics.
- Schonenberger, C.; Bachtold, A.; Strunk, C.; Salvétat, J. and Forro, L. (1999). Appl. Phys. A **69**, 283.

Schonenberger, C.; Buitelaar, M.; Kruger, M.; Widner, I.; Nussbaumer, T. and Iqbal, M. (2002). to be published.

Sharvin, Y. V.; Fiz., Zh. Eksp. Teor. (1965). Sov. Phys. JETP 21, 984.

Tans, S. J.; Devoret, M. H.; Dai, H. J.; Thess, A.; Smalley, R. E.; Geerligs, L. J. and Dekker, C. (1997). Nature **386**, 474.

Thess, A.; Lee, R.; Nikdaev, P.; Dai, H.; Petit, P.; Robert, J.; Xu, C.; Lee, Y. H.; Kim, S. G.; Rinzler, A. G.; Colbert, D. T.; Scuseria, G. E.; Tomanek, D.; Fischer, J. E.; Smalley, R. E. (1996). Science 273, 483.

Tsang, S. C.; Chen, Y. K.; Harris, P. J. F. and Green, M. L. H. (1994). Nature 372, 159.

Ugarte, D.; Chatelain, A. and de Heer, W. A. (1996). Science **274**, 1897.

Urbina, A.; Echeverría, I.; Pérez-Garrido, A. *et al.* (2003). Phys. Rev. Lett. **90**, 106603.

Venema, L. C.; Janssen, J. W.; Buitelaar, M. R.; Widoer, J. W. G.; Lemay, S. G.; Kouwenhoven, L. P. and Dekker, C. (2000). Phys. Rev. B **62**, 5238.

White C. T. and Mintmire, J. W. (1998). Nature **394**, 29.

White, C. T. and Todorov, T. N. (1998). Nature **393**, 240.

Wildoer, J. W. G.; Venema, L. C.; Rinzler, A. G.; Smalley, R. E. and Dekker, C. (1998). Nature **391**, 59.

Wychoff, R. W. G. (1964). Crystal Structures, (Interscience) New York, Vol. 1.

Yao, Z.; Kane, C. L. and Dekker, C. (2000). High-field electrical transport in single-wall carbon nanotubes. Phys. Rev. Lett **84**, 2941.

Yao, Z.; Dekker, C. and Avouris, P. (2001). in *Carbon Nanotubes*, edited by M. Dresselhaus, G. Dresselhaus and P. Avouris. Springer-Verlag, Heidelberg, p. 148.

Zettl, A. (unpublished).